國立臺灣大學電機資訊學院光電工程學研究所

碩士論文

Graduate Institute of Photonics and Optoelectronics

College of Electrical Engineering and Computer Science

National Taiwan University

Master Thesis

分析光柵結構的有限差分法與傅立葉模態法

Finite-Difference and Fourier Modal Methods for the Analysis of Gratings Structures

沈祺凱

Chi-Kai Shen

指導教授：邱奕鵬 博士

Advisor: Yih-Peng Chiou, Ph.D.

中華民國 九十九 年 六 月

June, 2010

國立臺灣大學碩士學位論文
口試委員會審定書

分析光柵結構的有限差分法與傅立葉模態法
Finite-Difference and Fourier Modal Methods for the Analysis of Gratings Structures

本論文係沈祺凱君（學號 R97941048）在國立臺灣大學光電工程學研究所完成之碩士學位論文，於民國 99 年 6 月 26 日承下列考試委員審查通過及口試及格，特此證明

口試委員：

邱奕鵬 （指導教授）

林宏洲　　王子建

所長 黃升龍

致謝

首先感謝指導教授邱奕鵬博士這兩年多來的教育，無論是在學術上或是研究態度上，都使我獲益良多，並給予我許多機會接觸學習新的事物，同時也要感謝口試委員林晃巖博士與王子建博士在口試當天針對論文內容給予許多相當有益的建議和指導。

另外，實驗室愉快的氣氛也是我碩士生涯中不可缺少的重要動力。感謝文嵐學姐、承翰學長與俊宏學長在研究上的協助，戰友們凡城、逸民、俊霖和建鴻學長帶給我的許多歡笑，以及早一步畢業的信毅學長、新生代禹秀學妹和牧珉學弟爲實驗室增添的更多熱鬧和趣味。這一切，都將讓我難以忘懷。

感謝家中可愛的姊姊和妹妹，讓我的窩總是如此溫暖，話題也總是無窮無盡，也謝謝同時在生理所打拼的曉君，能與我一路上相互砥礪。最重要的，是要謝謝我最愛的爸媽，除了生活上的照顧與關懷之外，也是我心中無比堅固的支柱和靠山，有他們陪伴是我生命中最大的驕傲。

摘要

本論文提出步階式數學形式之有限差分模態法來對光柵結構進行模擬並將其與傅立葉模態法(亦稱嚴格耦合波分析法)進行比較。我們的數值結果證實，對於橫電極化的所有情況以及橫磁極化在高導電性與無損金屬材料中，有限差分模態法比起嚴格耦合波分析法會有更好的收斂性和準確性。

對於有限差分模態法，我們考慮任意高階之邊界條件並將其與泰勒展開式結合。在不使所取格點數增加的情況下，我們亦將廣義道格拉斯(Douglas)方法套入使用來加速誤差收斂階數。使用前述技巧，可以對結構的每一層架構出稀疏矩陣並計算出存在於該層之模態所對應的場值分佈以及傳播常數。另外，我們也使用穆哈拉姆(Moharam)所提出之改良穿透矩陣方法來穩定多層光柵或甚至單層光柵層間的矩陣運算。

爲了評估此種數值方法的可用性，我們將討論一些光柵的繞射特性，如入射角變化、厚度變化、佔空比變化所造成的影響，以及準確性、收斂性等等。另外，我們也使用結合週期性邊界和吸收邊界的二維有限差分法來與前述方法進行比較。

關鍵詞：

傅立葉模態法、嚴格耦合波分析法、頻域有限差分法、任意階數邊界條件、廣義道格拉斯方法、改良穿透矩陣方法、完美匹配層。

Abstract

In this thesis, the finite-difference modal method (FDMM) with step-index formulation for simulating grating structures is proposed and compared with rigorous coupled-wave analysis (RCWA), also called Fourier modal method (FMM). It is verified that FDMM has better convergence and accuracy than RCWA for TE polarization in almost all cases and TM polarization for high conductive and lossless metallic materials.

In the FDMM, the relation of interface conditions to arbitrary high orders is considered and combines with Taylor series expansion. The generalized Douglas (GD) scheme is also adopted to enhance the convergence order without considering more sampled points. With the techniques mentioned above, the sparse matrix of eigenvalue problem could be constructed to solve the fields and the propagation constants of modes inside each layer. In addition, the enhanced transmittance matrix approach proposed by Moharam *et al.* for RCWA is used to make matrix manipulation stable for multi-layer or even single layer gratings.

The diffraction properties of gratings, such as accuracy, convergence, dependence of diffraction efficiencies on incident angle, thickness, duty cycle, etc, will be discussed for numerical assessment of FDMM. Moreover, two-dimensional finite-difference methods combined with periodic boundary conditions and absorbing boundary conditions will be executed for comparison.

Keywords:

Fourier modal method, rigorous coupled-wave analysis, finite-difference frequency-domain method, arbitrary-order interface conditions, generalized Douglas scheme, enhanced transmittance matrix approach, perfectly matched layer.

Contents

1 Introduction **1**

1.1 Overview 1

1.2 Literature Survey 2

1.3 Motivation 5

1.4 Chapter Outline 6

2 Formulation **8**

2.1 Fourier Modal Method (or RCWA) 9

2.1.1 Planar Diffraction of Rectangular-Groove Gratings . . 10

2.1.2 Multi-layer Approximation for Arbitrary Shape Gratings 15

2.1.3 Stable Approach for Multi-layer Approximation 18

2.2 Finite-Difference Modal Method 21

2.2.1 Eigenvalue Problems inside Each Layer 22

2.2.2 Evaluation of Diffraction Efficiencies 28

2.3 Two-Dimensional Finite-Difference Method 31

2.3.1 Discretizing Maxwell's Equation 31

2.3.2 Mesh Truncation 38
2.3.3 Incident Wave Source Conditions 44
2.3.4 Calculating Diffraction Efficiencies 47

3 Numerical Results and Discussions **49**

3.1 Numerical Verification of FDMM 49
3.1.1 Incident Angle Variation 50
3.1.2 Thickness Variation 54
3.1.3 Duty Cycle Variation: Removing the Instability 57
3.2 Analysis of Accuracy and Convergence 58
3.3 FDMM for TE polarization 60
3.3.1 Rectangular-Groove Gratings 60
3.3.2 Arbitrary Profiles Gratings 67
3.4 FDMM for TM polarization 72
3.4.1 Rectangular-Groove Gratings 72
3.4.2 Arbitrary Profiles Gratings 82
3.5 Numerical Verification of 2DFD 86

4 Conclusion **91**

Bibliography **93**

List of Figures

2.1 Grating with one-dimensional periodicity. 8

2.2 Rectangular-groove grating. 10

2.3 Example of multi-layer approximation. 16

2.4 One-dimensional discretization. 22

2.5 Sketch of a discontinuity between sampled points. 23

2.6 Periodic boundaries. 27

2.7 Configuration of two-dimensional finite difference. 31

2.8 Two-dimensional discretization. 32

2.9 Method of averaging permittivity. 34

2.10 Continuity of fields on interfaces. 35

2.11 A real region surrounded by PML to approximate the infinite region. 39

2.12 Configuration of multi-stretched-coordinate in PML. 43

2.13 Total-field and scattered-field regions connected by a plane wave source. 45

3.1 Fig.8 in the paper of Sheng *et al.* [30]. The zeroth-order reflection with respect to the incident angle. 51
3.2 Incident angle dependence of the zeroth-order reflection for lossy metal with TM polarization (compared with Fig. 3.1). . 51
3.3 Field diagram of Fig. 3.2 at incident angle $\theta = 0°$ (Left: RCWA, Right: FDMM). 52
3.4 Field diagram of Fig. 3.2 at incident angle $\theta = 15°$ (Left: RCWA, Right: FDMM). 52
3.5 Fig.9 in the paper of Pai and Awada [25]. Transmittance with respect to the incident angle. 53
3.6 Incident angle dependence of the zeroth- and first-order transmittance for the dielectric triangular grating under TE incidence (comparing with Fig. 3.5). 53
3.7 Fig.6 of paper of Sheng *et al.* [30]. The first-order reflection of Al and Ag gratings with respect to the thickness. 55
3.8 Thickness dependence of first-order reflection for Al and Ag gratings under TM incidence (compared with Fig. 3.7). 55
3.9 Fig.6 of paper of Sheng *et al.* [30]. The absorption of Al and Ag gratings with respect to the thickness. 56
3.10 Thickness dependence of absorption of Al and Ag gratings under TM incidence (compared with Fig. 3.9). 56

3.11 Fig.1 of paper of Lyndin *et al.* [19]. The minus-first-order reflection with respect to groove width. 57
3.12 Groove width dependence of minus-first-order reflection (comparing with Fig. 3.11). 58
3.13 Accuracy and convergence of β of fundamental mode. A dielectric grating with $\varepsilon_{r,g1} = 3^2$ under TE incidence. 63
3.14 Convergence of the zeroth-order reflection. A dielectric grating with $\varepsilon_{r,g1} = 3^2$ under TE incidence. 63
3.15 Accuracy and convergence of β of fundamental mode. A lossless metallic grating with $\varepsilon_{r,g1} = (-10i)^2$ under TE incidence. . 64
3.16 Convergence of the zeroth-order reflection. A lossless metallic grating with $\varepsilon_{r,g1} = (-10i)^2$ under TE incidence. 64
3.17 Accuracy and convergence of β of fundamental mode. A lossy grating with $\varepsilon_{r,g1} = (3.18 - 4.41i)^2$ under TE incidence. 65
3.18 Convergence of the zeroth-order reflection. A lossy grating with $\varepsilon_{r,g1} = (3.18 - 4.41i)^2$ under TE incidence. 65
3.19 Accuracy and convergence of β of fundamental mode. A high conductive grating metallic with $\varepsilon_{r,g1} = (1 - 40i)^2$ under TE incidence and nonuniform discretization. 66

3.20 Convergence of the zeroth-order reflection. A high conductive metallic grating with $\varepsilon_{r,g1} = (1 - 40i)^2$ under TE incidence and nonuniform discretization. 66
3.21 Configuration of triangular gratings. 67
3.22 Revised discretization for multi-layer approximation. 68
3.23 Convergence of the zeroth-order reflection. A dielectric triangular grating with $\varepsilon_{g1} = 3^2$ under TE incidence. 70
3.24 Convergence of the zeroth-order reflection with proper discretization. A dielectric triangular grating with $\varepsilon_{g1} = 3^2$ under TE incidence. 70
3.25 Convergence of the zeroth-order reflection with proper discretization. A lossless metal triangular grating with $\varepsilon_{g1} = (-10i)^2$ under TE incidence. 71
3.26 Convergence of the zeroth-order reflection with proper discretization. A lossy triangular grating with $\varepsilon_{g1} = (3.18 - 4.41i)^2$ under TE incidence. 71
3.27 Accuracy and convergence of β of fundamental mode. A dielectric grating with $\varepsilon_{r,g1} = 3^2$ under TM incidence. Grids are distributed by ratio of width. 74

3.28 Convergence of the zeroth-order reflection. A dielectric grating with $\varepsilon_{r,g1} = 3^2$ under TM incidence. Grids are distributed by ratio of width. 74

3.29 Accuracy and convergence of β of fundamental mode. A lossless metallic grating with $\varepsilon_{r,g1} = (-10i)^2$ under TM incidence. Grids are distributed by ratio of width. 75

3.30 Convergence of the zeroth-order reflection. A lossless metallic grating with $\varepsilon_{r,g1} = (-10i)^2$ under TM incidence. Grids are distributed by ratio of width. 75

3.31 Accuracy and convergence of β of fundamental mode. A lossy grating with $\varepsilon_{r,g1} = (3.18-4.41i)^2$ under TM incidence. Grids are distributed by ratio of width. 76

3.32 Convergence of the zeroth-order reflection. A lossy grating with $\varepsilon_{r,g1} = (3.18 - 4.41i)^2$ under TM incidence. Grids are distributed by ratio of width. 76

3.33 Accuracy and convergence of β of fundamental mode. A lossy grating with $\varepsilon_{g1} = (0.22 - 6.71i)^2$ under TM incidence. Grids are distributed by ratio of width. 77

3.34 Convergence of the zeroth-order reflection. A lossy grating with $\varepsilon_{g1} = (0.22 - 6.71i)^2$ under TM incidence. Grids are distributed by ratio of width. 77

3.35 Accuracy and convergence of β of fundamental mode. A highly conductive grating with $\varepsilon_{g1} = (1 - 40i)^2$ under TM incidence. Grids are distributed by ratio of width. 78

3.36 Convergence of the zeroth-order reflection. A highly conductive grating with $\varepsilon_{g1} = (1 - 40i)^2$ under TM incidence. Grids are distributed by ratio of width. 78

3.37 Continuity of E_x fields for TM polarization. 79

3.38 Convergence of the zeroth-order transmittance. A dielectric triangular grating with $\varepsilon_{g1} = 3^2$ under TM incidence. 84

3.39 Convergence of the zeroth-order transmittance with proper discretization. A dielectric triangular grating with $\varepsilon_{g1} = 3^2$ under TM incidence. 84

3.40 Convergence of the zeroth-order reflection with proper discretization. A lossless metal triangular grating with $\varepsilon_{g1} = (-10i)^2$ under TM incidence. 85

3.41 Convergence of the zeroth-order reflection with proper discretization. A lossy triangular grating with $\varepsilon_{g1} = (3.18 - 4.41i)^2$ under TM incidence. 85

3.42 Duty cycle variation of the minus-first-order reflection. A dielectric grating with $\varepsilon_{g1} = 3^2$ under TM incidence. 2DFD with averaging permittivity is used. 86

3.43 Duty cycle variation of the minus-first-order reflection. A lossless metallic grating with $\varepsilon_{g1} = (-10i)^2$ under TM incidence. 2DFD with averaging permittivity is used. 87

3.44 Duty cycle variation of the minus-first-order reflection. A lossless metallic grating with $\varepsilon_{g1} = (-10i)^2$ under TM incidence. 2DFD with considering boundary condition is used. 88

3.45 Field diagram of Fig. 3.12 at groove width= $302nm$ (Left: RCWA, Right: FDMM) 89

3.46 Field diagram of Fig. 3.12 at groove width= $302nm$ (Left: Graded-index 2DFD, Right: Step-index 2DFD) 89

3.47 Field diagram of Fig. 3.12 at groove width= $250nm$ (Left: RCWA, Right: FDMM) 90

3.48 Field diagram of Fig. 3.12 at groove width= $250nm$ (Left: Graded-index 2DFD, Right: Step-index 2DFD) 90

Chapter 1

Introduction

1.1 Overview

Diffraction of optical electromagnetic radiation by periodic structures is important for many engineering applications. Grating diffraction is central in the fields of integrated optics, holography, optical data processing, spectral analysis, etc. There are numerous numerical methods with variety of possible assumptions to analyze diffraction properties of gratings, and most of them are not only tools for solving mathematical equations but also imply some physical insights of the problems. Thanks to advancement of computer technology, numerical methods and computer-aided design (CAD) become more important and convenient for finding optimized parameters for high cost or complicated experiments.

1.2 Literature Survey

The Fourier modal method (FMM) which is a kind of differential methods [1] and often referred to as rigorous coupled-wave analysis (RCWA) was first formulated for planar gratings by Moharam and Gaylord [2] [3] [4], and then extended to surface-relief gratings [7] [6] and crossed-grating structures. It provides the exact solutions whose accuracy depends solely on the numbers of terms retained in the space-harmonic expansions of the fields.

Before this method was proposed, the most common differential methods were the coupled-wave approach [8] and the modal approach [9]. The coupled-wave approach, which expanding the solution into plane-wave components, had been known to offer a relatively simple formulation and superior physical insight into wave-diffraction phenomena. In this approach, several assumptions were made in order to obtain solutions such as neglecting the second order derivatives of the field amplitudes and retaining only one diffracted wave. The modal approach, which through eigenmode expansion, was a rigorous exact analysis but complicated mathematically. However, Magnusson and Gaylord [10] had shown that these two approaches are equivalent and the coupled-wave approach could become rigorous by including all diffracted waves in the formulation together with retaining the second derivatives of the electromagnetic fields. Therefore, RCWA was created by considering the coupled-wave approach without the assumptions as mentioned above.

As matching the boundary conditions between every layers and finding diffraction efficiencies, some instabilities would be introduced because taking the inverse of some ill-condition matrices. Several methods such as R-matrix, S-matrix, and other approaches which were compared systematically by Li [11] have been proposed to produce stable implementation for this problem, and the method proposed by Moharam *et al.* [12] in 1995 will be mentioned in section 2.1.3.

Another problem of RCWA discovered by Li and Haggans [13] is poor convergence as dealing with metallic gratings under TM incidence. The convergence was dramatically improved by the reformulation by Lalanne and Morris [14] and Granet and Guizal [15], and this improvement was explained by Li [16] mathematically. He proved the origin of poor convergence comes from the mistakes of using Fourier factorization and proposed the inverse rule of factorization to uniformly satisfy the boundary conditions in the grating region.

However, even using the modified factorization mentioned above, Popov *et al.* [17] discovered a numerical instability problem in this differential theory as applied to metallic gratings with very high conductivity under TM incidence. They attributed these instabilities to the imperfect condition of matrices generated by Fourier coefficients of permittivity distribution to be inverted. This statement was later questioned by Watanabe [18]. Some heuristical solutions

proposed by them were introducing artificial metal losses in order to damp the instabilities or applying two-step truncation [17]. Such strategy obviously treats a neighboring but different electromagnetic problem. Lyndin *et al.* [19] established the link between the instabilities and the spurious modes corresponding to instable high order eigenvalues. They proposed a procedure of identification and filtration of these spurious modes, but such tracking of those artifactual modes are complicated. Furthermore, Guizal *et al.* [20] applied the reformulation of FMM with adaptive spatial resolution proposed by Granet [21] to approach the problem of highly conductive gratings under TM incidence and get even more stable solution.

Finite difference (FD) methods for solving partial difference are also used in electromagnetism for solving Maxwell's equations. This method is not widely used in grating theory but often used to study the diffraction by aperiodic objects of finite dimension because of their suitability for incorporating absorbing boundary conditions to limit the computational domain. Generally, standard FD methods require a two-dimensional (2D) mesh for the discretization of a one-dimensional (1D) grating. After adding periodic boundary conditions, absorbing boundaries and sources, the fields of scattering problems could be solved and used to find diffraction efficiencies.

However, Lalanne and Hugonin [22] proposed a very simple method for the analysis of 1D lamellar gratings. This method is solving eigenmodes in-

side the gratings region such as FMM (RCWA) but using finite-difference approach. And it is similar to numerical techniques that are based on finite-difference modal approaches and used in waveguide theories. They used a first-order method with averaging permittivity and found that their method is much inferior to the RCWA for dielectric gratings. In contrast, their method compared favorably with the RCWA for metallic gratings operating in the infrared regions of the spectrum, especially for TM polarization. They also proposed three crucial methods to accelerate the convergence: (1) proper interpolation for averaging permittivity, (2) mesh points on discontinuities and (3) non-uniform sampling near the discontinuities. Their numerical results indicated that FD approach offers rather good performance for highly conducting gratings and TM polarization.

1.3 Motivation

In the paper of Lalanne and Hugonin [22], they presented the finite-difference modal method and declared good performance for metallic gratings and TM polarization but worse convergence than RCWA for TE polarization. Inside the grating layer, what they used is an interpolation scheme that locally averages the permittivity, and they said the method of interpolation has a drastic impact on the convergence performance. In addition, they only considered first-order finite-difference and expected that faster convergence

rates can be achieved by using higher order method but the computational efficiency will be reduced because of increasing non-zero value in the eigen matrices.

Therefore, the finite-difference modal method (FDMM) with even higher order formulation and considering boundary conditions instead of interpolation is introduced and tested in this thesis. With the generalized Douglas scheme [23] [24], the convergence order can be increased without adding the mesh points, so the computational time and the computer memory does not be increased. For comparison, the two-dimensional finite-difference both for graded-index approximation and step-index approximation will be investigated.

1.4 Chapter Outline

There are three chapters following this introduction.

In chapter 2, the Fourier modal method (FMM), or rigorous coupled wave analysis (RCWA) is demonstrated first both for rectangular-groove gratings and surface-relief gratings. Surface-relief gratings, which also called arbitrary profile gratings, can use many layers of rectangular-groove gratings with different duty cycles to approximate. A stable approach will then be mentioned to solve the unstable problems as using above approximation. Next, the finite-difference modal method (FDMM) will be proposed by us-

ing step-index formulation with or without generalized Douglas scheme inside each grating layer and stable approach used in RCWA. Last, the two-dimensional finite-difference (2DFD) with averaging permittivity and considering boundary condition will be applied to the same configuration which solved by RCWA and FDMM above. In addition, two different methods of perfectly matched layers and total fields/scattered fields (TF/SF) for adding sources will be mentioned.

In chapter 3, numerical results are given to assess the formulations mention in chapter 2. First, some papers' results will be used to verify the correctness of FDMM and RCWA, and the problems of RCWA will be seen for lossless metallic or high conductive gratings under TM incidence. Second, accuracy and convergence of propagation constants and diffraction efficiencies of these two numerical methods will be defined and discussed for every kinds of materials, both of TE and TM polarization and both of rectangular-groove gratings and arbitrary profile gratings. Finally, 2DFD will be used to solve the same problem which suffers from serious instabilities with lossless metallic gratings under TM incidence.

Chapter 4 concludes this thesis.

Chapter 2

Formulation

The geometry of the problem we deal with is one dimensional periodic grating depicted in Fig. 2.1, which is separated into reflection region, grating region and transmission region. The normal to the interface between any adjacent two regions is along z direction, and the grating is periodic along x direction and infinite along y direction.

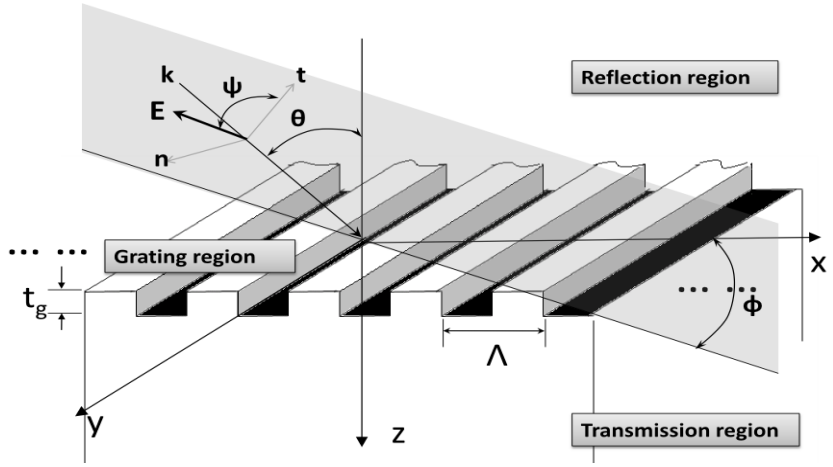

Figure 2.1: Grating with one-dimensional periodicity.

2.1 Fourier Modal Method (or RCWA)

The main idea of RCWA is to express both permittivity and electromagnetic fields by Fourier bases. In the grating region, the periodic relative permittivity $\epsilon(x)$ is expandable in a Fourier series of the form

$$\epsilon(x) = \sum_h \epsilon_h e^{j\frac{2\pi}{\Lambda}hx}, \tag{2.1}$$

where Λ is grating period and ϵ_h is the hth Fourier coefficient of the relative permittivity which can be found by

$$\epsilon_h = \frac{1}{\Lambda}\int_{x_i}^{x_i+\Lambda} \epsilon(x) e^{-j\frac{2\pi}{\Lambda}hx} dx, \tag{2.2}$$

where x_i is any initial position in the integration. Regarding the electromagnetic fields, it assumes that these could be expanded by Fourier bases along the periodic direction x and form a set of modes along the propagation direction z and are expressed as

$$\psi_m(x,z) \sim \left(\sum_i C_{mi} e^{-jk_{xi}x}\right) \times e^{\pm j\beta_m z}, \tag{2.3}$$

where m is the index of mode, β_m is the propagation constant of mode m, $k_{xi} = k_0 \sin(\theta_{incidence}) + i\frac{2\pi}{\Lambda}$ and C_{mi} is the contribution of mode m to the ith Fourier order.

After using above approximation to rewrite Maxwell's equations, an eigenvalue problem is constructed and used to find every eigenmodes inside the

grating layer. Then we match boundary condition of tangential field components at each interface between two adjacent layers and calculate the diffraction efficiencies finally. More details of RCWA will be shown in the following subsections.

2.1.1 Planar Diffraction of Rectangular-Groove Gratings

For simplicity, only TM polarization (H_y,E_x,E_z), which means the magnetic field is perpendicular to the plane of incidence (which means x-z plane here), is going to be demonstrated, and the mathematical derivation of TE polarization is similar to that of TM. The structure of a rectangular-groove grating is depicted in Fig. 2.2. Assume the incidence wave is a plane wave given by

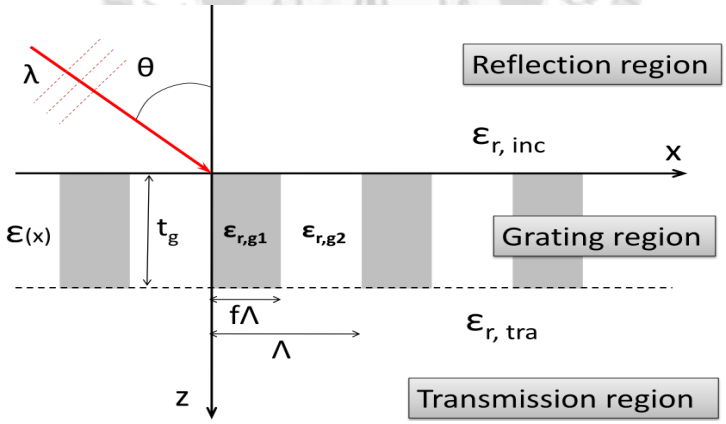

Figure 2.2: Rectangular-groove grating.

$$H_y^{inc} = e^{-jk_0\sqrt{\epsilon_{r,inc}}(\sin\theta x+\cos\theta z)}, \tag{2.4}$$

where k_0 is the wave vector in free space, and θ is the incident angle. However, it also could be any other kinds of waves. And the solutions form of reflection and transmission are given by

$$H_y^R = \sum_i R_i e^{-j(k_{xi}x - k_{zi}^R z)} \tag{2.5}$$

and

$$H_y^T = \sum_i T_i e^{-j[k_{xi}x + k_{zi}^T (z-t)]}, \tag{2.6}$$

where $k_{zi}^R = \sqrt{k_0^2 \epsilon_{r,inc} - k_{xi}^2}$, $k_{zi}^T = \sqrt{k_0^2 \epsilon_{r,tra} - k_{xi}^2}$ and t is the thickness of grating. The electric fields in these regions can be obtained from Maxwell's equation $\mathbf{E} = \frac{1}{j\omega\epsilon_0\epsilon_r} \nabla \times \mathbf{H}$.

In the grating region, we would like to solve modes propagated along direction z. Being analogous to (2.3), the fields may be expressed as

$$H_y^G = \sum_i U_{yi}(z) e^{-jk_{xi}x}, \tag{2.7}$$

where $U_{yi}(z)$ means the contribution of every modes to the ith space harmonic fields. After substituting it into Maxwell's equations, we will get

$$E_x^G = \alpha \sum_i S_{yi}(z) e^{-jk_{xi}x}, \tag{2.8}$$

where α is normalization constant which will be decided later. For TM polarization, Maxwell's equations $\mathbf{E} = \frac{1}{j\omega\epsilon_0\epsilon_r} \nabla \times \mathbf{H}$ and $\mathbf{H} = \frac{-1}{j\omega\mu_0} \nabla \times \mathbf{E}$ will be simplified to be

$$E_z^G = \frac{1}{j\omega\epsilon_0\epsilon_r(x)} \frac{\partial H_y^G}{\partial x} \tag{2.9}$$

$$E_x^G = \frac{1}{j\omega\epsilon_0\epsilon_r(x)}\left(-\frac{\partial H_y^G}{\partial z}\right) \tag{2.10}$$

$$-j\omega\mu_0 H_y^G = \frac{\partial E_x^G}{\partial z} - \frac{\partial E_z^G}{\partial x}. \tag{2.11}$$

First considering (2.10). If we define

$$\frac{1}{\epsilon_r(x)} = \sum_h a_h e^{j\frac{2\pi}{\Lambda}hx} \tag{2.12}$$

and substitute (2.12), (2.7) and (2.8) into (2.10). we will obtain

$$\alpha \cdot S_{xi} = \frac{-1}{j\omega\epsilon_0}\sum_p a_{ip}\frac{\partial U_{yi}}{\partial z}, \tag{2.13}$$

where $a_{ip} \equiv a_{p-i}$ is Fourier coefficient of $\epsilon_r^{-1}(x)$. Next, combining (2.11) with (2.9) and substituting (2.12), (2.7) and (2.8) into this combination, then we obtain

$$\alpha \cdot \frac{\partial S_{xi}}{\partial z} = \frac{-jk_{xi}}{j\omega\epsilon_0}\sum_p a_{ip}(-jk_{xi})U_{yp} - i\omega\mu_0\sum_i U_{yi}. \tag{2.14}$$

Now we can see that if $\alpha \equiv \frac{1}{j\omega\epsilon_0}$, the (2.13) and (2.14) will become simpler. Finally, combining the (2.13) with (2.14) and eliminating S_{xi}, we obtain

$$\sum_p a_{ip}\frac{\partial^2 U_{yp}}{\partial z^2} = k_{xi}\sum_p a_{ip}k_{xp}U_{yp} - k_0^2 U_i, \tag{2.15}$$

or, in matrix form,

$$\mathbf{AU''} = \mathbf{K_x A K_x U} - k_0^2\mathbf{U}, \tag{2.16}$$

where $\mathbf{A} \equiv [a_{ip}]$ and $\mathbf{K_x} \equiv diag[k_{xi}]$. Therefore, now we know the eigenvalue problem used to be solved is

$$\mathbf{U''} = \mathbf{A^{-1}}(\mathbf{K_x A K_x U} - k_0^2\mathbf{I})\mathbf{U}. \tag{2.17}$$

However, from the empirical advice of Lalanne and Morris [14] (by quasi-static limit description), G. Granet and B. Guizal [15] in 1996 and the mathematical foundation given by Li [16] that the matrix $\mathbf{A}$ in the parenthesis of (2.17) is better to be replaced by $\mathbf{E^{-1}}$, where $\mathbf{E} \equiv [\epsilon_{ip}]$, for improving convergence. This replacement will improve the convergence. Namely, we solve

$$\mathbf{U}'' = \mathbf{A^{-1}}(\mathbf{K_x E^{-1} K_x U} - k_0^2 \mathbf{I})\mathbf{U} \equiv -\mathbf{MU} \tag{2.18}$$

finally instead of (2.17). If the field assumption is like (2.3), i.e., $U_{yi}(z) \sim \sum_m C_{mi} e^{\pm j\beta_m z}$, we could know that

$$\mathbf{U}'' = \left[\sum_i \frac{\partial^2 U_{yi}(z)}{\partial z^2} \right] = -\boldsymbol{\beta}^{\mathbf{2}} \mathbf{U}, \tag{2.19}$$

and be sure that the eigenvalue problem is $\mathbf{MU} = \boldsymbol{\beta}^{\mathbf{2}}\mathbf{U}$, where $\boldsymbol{\beta}^{\mathbf{2}}$ is a diagonal matrix containing eigenvalues.

After solving the eigenvalue problem above, the space harmonics of tangential electric and magnetic fields are given by

$$\begin{aligned} U_{yi} &= \sum_m w_{im} \{ g_m^+ e^{-j\beta_m z} + g_m^- e^{+j\beta_m (z - t_g)} \} \\ S_{yi} &= -\sum_p \sum_m a_{ip} w_{pm} (-j\beta_m) \{ g_m^+ e^{-j\beta_m z} - g_m^- e^{+j\beta_m (z - t_g)} \}, \end{aligned} \tag{2.20}$$

where w_{im} and β_m are the elements of the eigenvector matrix $\mathbf{W}$ and the square root of the eigenvalues of the matrix $\mathbf{M}$. The quantities g_m^+ and g_m^- are unknown constants to be determined by matching boundary conditions. Physically, g_m^+ and g_m^- mean the contribution of each mode. The columns of

$[w_{im}]$ means which mode, and the ith row of column m represents the ratio of tth space harmonic in this mode.

To solve reflection coefficient R_i, transmission coefficient T_i, g_m^+ and g_m^-, the boundary conditions of tangential fields are used. For TM polarization, the component E_x, which means $\frac{1}{\epsilon_r}\frac{\partial H_y}{\partial z}$, and H_y are continuous at discontinuities. At the input boundary ($z = 0$)

$$\delta_{i0} + R_i = \sum_m w_{im}\{g_m^+ + e^{-j\beta_m t_g} g_m^-\} \tag{2.21}$$

and

$$\frac{-jk_0\sqrt{\epsilon_{r,inc}}\cos\theta\delta_{i0}}{\epsilon_{r,inc}} + \frac{jk_{zi}^R}{\epsilon_{r,inc}} R_i = \sum_p \sum_m a_{ip} w_{pm}(-j\beta_m)\{g_m^+ - e^{-j\beta_m t_g} g_m^-\}, \tag{2.22}$$

or in matrix form,

$$\begin{bmatrix} \delta_{i0} \\ \frac{-jk_0\cos\theta}{\sqrt{\epsilon_{r,inc}}}\delta_{i0} \end{bmatrix} + \begin{bmatrix} \mathbf{I} \\ -\mathbf{Z_R} \end{bmatrix} \mathbf{R} = \begin{bmatrix} \mathbf{W} & \mathbf{WX} \\ \mathbf{AWZ} & -\mathbf{AWZX} \end{bmatrix} \begin{bmatrix} g_m^+ \\ g_m^- \end{bmatrix}, \tag{2.23}$$

where $\mathbf{Z_R} \equiv diag[-jk_{zi}^R/\epsilon_{r,inc}]$, $\mathbf{Z} \equiv diag[-j\beta_m]$ and $\mathbf{X} \equiv diag[\exp(-j\beta_m t_g)]$.

At $z = t_g$,

$$\sum_m w_{im}\{e^{-j\beta_m t_g} g_m^+ + g_m^-\} = T_i \tag{2.24}$$

and

$$\sum_p \sum_m a_{ip} w_{pm}(-j\beta_m)\{e^{-j\beta_m t_g} g_m^+ - g_m^-\} = \frac{-jk_{zi}^T}{\epsilon_{r,tra}} T_i, \tag{2.25}$$

or in matrix form,

$$\begin{bmatrix} \mathbf{WX} & \mathbf{W} \\ \mathbf{AWZX} & -\mathbf{AWZ} \end{bmatrix} \begin{bmatrix} g_m^+ \\ g_m^- \end{bmatrix} = \begin{bmatrix} \mathbf{I} \\ \mathbf{Z_T} \end{bmatrix} \mathbf{T}, \tag{2.26}$$

where $\mathbf{Z_T} \equiv diag[-jk_{zi}^T/\epsilon_{r,tra}]$.

The coefficients R_i and T_i could be found by using (2.23) and (2.26). The diffraction efficiencies could be calculated by the definition of the ratio of Poynting's vectors along propagation direction z. For TM polarization here, the Poynting's vector in the propagation direction z is

$$P_z = \frac{1}{2} Re\left[E_x H_y^*\right] = \frac{1}{2} Re\left[\frac{j}{\omega\epsilon_0\epsilon_r}(\frac{\partial H_y}{\partial z})H_y^*\right], \tag{2.27}$$

and the diffraction efficiencies are defined as

$$\begin{aligned} DEr_i &= \frac{P_z^R}{P_z^{inc}} = |R_i|^2 Re\left[\frac{k_{zi}^R}{k_{z0}}\right] \\ DEt_i &= \frac{P_z^T}{P_z^{inc}} = |T_i|^2 Re\left[\frac{\epsilon_{r,inc}}{\epsilon_{r,tra}}\frac{k_{zi}^T}{k_{z0}}\right]. \end{aligned} \tag{2.28}$$

For lossless gratings, the sum of the reflected and transmitted diffraction efficiencies given by (2.28) must be unity, which means conservation of energy. In addition, if it needs to plot the field diagrams, solve coefficients g_m^+ and g_m^- after finding R_i and T_i. In the next subsection, we will generalize the structure to arbitrary shape.

2.1.2 Multi-layer Approximation for Arbitrary Shape Gratings

For gratings with arbitrary profiles, we divide the grating into a large number of sufficiently thin layers and approximate each layer by a rectangular-groove grating, which was use first proposed by Peng *et al.* and applied to RCWA by Moharam and Gaylord [6], as in Fig. 2.3.

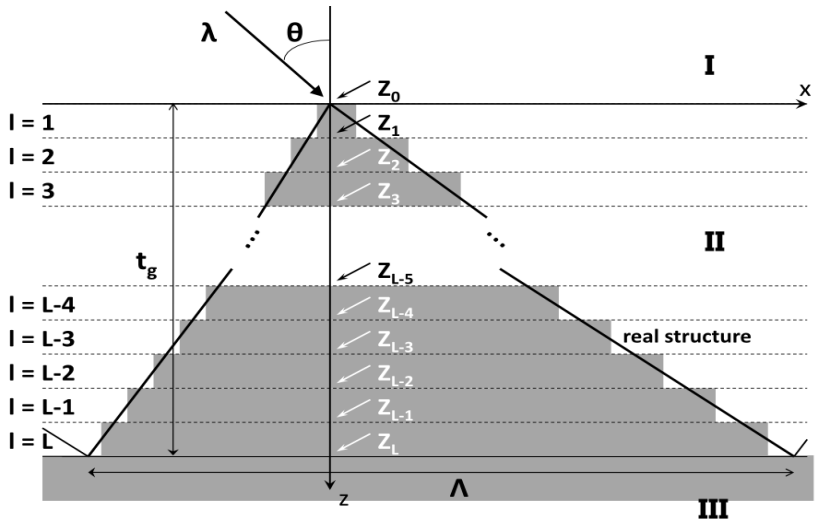

Figure 2.3: Example of multi-layer approximation.

The electromagnetic fields in each grating layer are determined by RCWA for rectangular-groove gratings (or by other approaches, such as the modal approach and the finite difference approach). Then boundary conditions of the tangential fields are applied in sequence at every interfaces to get reflected and transmitted diffracted field amplitudes and diffraction efficiencies. Here we still use TM polarization to illustrate the formulation.

After solving the eigenvalue problems in each grating layer, the space harmonics of tangential fields of every layers are given by

$$U_{l,yi} = \sum_m w^l_{im}\{g^+_{l,m}e^{-j\beta^l_m(z-z_{l-1})} + g^-_{l,m}e^{+j\beta^l_m(z-z_l)}\}$$
$$S_{l,yi} = -\sum_p\sum_m a^l_{ip}w^l_{pm}(-j\beta^l_m)\{g^+_{l,m}e^{-j\beta^l_m(z-z_{l-1})} - g^-_{l,m}e^{+j\beta^l_m(z-z_l)}\}, \quad (2.29)$$

where the index l means which grating layer. Then we match boundary con-

dition at every interfaces and express these in matrix form. At the interface between the input region and the first grating layer, i.e. at $z = 0$ in Fig. 2.3,

$$\begin{bmatrix} \delta_{i0} \\ \frac{-jk_0\cos\theta}{\sqrt{\epsilon_{r,inc}}}\delta_{i0} \end{bmatrix} + \begin{bmatrix} \mathbf{I} \\ -\mathbf{Z_R} \end{bmatrix} \mathbf{R} = \begin{bmatrix} \mathbf{W}_1 & \mathbf{W}_1\mathbf{X}_1 \\ \mathbf{A}_1\mathbf{W}_1\mathbf{Z}_1 & -\mathbf{A}_1\mathbf{W}_1\mathbf{Z}_1\mathbf{X}_1 \end{bmatrix} \begin{bmatrix} g^+_{1,m} \\ g^-_{1,m} \end{bmatrix}, \tag{2.30}$$

where the suffixes of $\mathbf{W}$, $\mathbf{A}$, $\mathbf{Z}$ and $\mathbf{X}$ mean which grating layer and the definitions of these matrices are same as in preceding subsection, at the interface between $(l-1)$th and lth layer ($z = z_{l-1}$)

$$\begin{bmatrix} \mathbf{W}_{l\text{-}1}\mathbf{X}_{l\text{-}1} & \mathbf{W}_{l\text{-}1} \\ \mathbf{A}_{l\text{-}1}\mathbf{W}_{l\text{-}1}\mathbf{Z}_{l\text{-}1}\mathbf{X}_{l\text{-}1} & -\mathbf{A}_{l\text{-}1}\mathbf{W}_{l\text{-}1}\mathbf{Z}_{l\text{-}1} \end{bmatrix} \begin{bmatrix} g^+_{l-1,m} \\ g^-_{l-1,m} \end{bmatrix} = \begin{bmatrix} \mathbf{W}_l & \mathbf{W}_l\mathbf{X}_l \\ \mathbf{A}_l\mathbf{W}_l\mathbf{Z}_l & -\mathbf{A}_l\mathbf{W}_l\mathbf{Z}_l\mathbf{X}_l \end{bmatrix} \begin{bmatrix} g^+_{l,m} \\ g^-_{l,m} \end{bmatrix}, \tag{2.31}$$

and at the interface between the last grating layer and the output region

$$\begin{bmatrix} \mathbf{W}_L\mathbf{X}_L & \mathbf{W}_L \\ \mathbf{A}_L\mathbf{W}_L\mathbf{Z}_L\mathbf{X}_L & -\mathbf{A}_L\mathbf{W}_L\mathbf{Z}_L \end{bmatrix} \begin{bmatrix} g^+_{L,m} \\ g^-_{L,m} \end{bmatrix} = \begin{bmatrix} \mathbf{I} \\ \mathbf{Z_T} \end{bmatrix} \mathbf{T}. \tag{2.32}$$

Finally, (2.30)-(2.32) are rewritten as

$$\begin{bmatrix} \delta_{i0} \\ \frac{-jk_0\cos\theta}{\sqrt{\epsilon_{r,inc}}}\delta_{i0} \end{bmatrix} + \begin{bmatrix} \mathbf{I} \\ -\mathbf{Z_R} \end{bmatrix} \mathbf{R} = \prod_{l=1}^{L} \begin{bmatrix} \mathbf{W}_l & \mathbf{W}_l\mathbf{X}_l \\ \mathbf{A}_l\mathbf{W}_l\mathbf{Z}_l & -\mathbf{A}_l\mathbf{W}_l\mathbf{Z}_l\mathbf{X}_l \end{bmatrix} \times \begin{bmatrix} \mathbf{W}_l\mathbf{X}_l & \mathbf{W}_l \\ \mathbf{A}_l\mathbf{W}_l\mathbf{Z}_l\mathbf{X}_l & -\mathbf{A}_l\mathbf{W}_l\mathbf{Z}_l \end{bmatrix}^{-1} \begin{bmatrix} \mathbf{I} \\ \mathbf{Z_T} \end{bmatrix} \mathbf{T}. \tag{2.33}$$

However, this approximation used in successive field matching may introduce numerical instability which is due to the presence of evanescent fields. And these evanescent waves, which possess large imaginary part of β, will

make the matrix $\mathbf{X}$ to be ill-conditioned as doing matrix inverse. In the next subsection we will introduce stable approaches to eliminate the numerical instability.

2.1.3 Stable Approach for Multi-layer Approximation

There are several approaches which have been proposed to produce stable implementation. For example, Moharam and Gaylord [6] obtained numerically stable RCWA calculation for TE polarization and dielectric gratings to a grating depth of as many as four wavelengths, by sequential Gaussian elimination scheme. Pai and Awada [25] use layer transmission matrices and interface reflection and transmission matrices to derive the solution for RCWA in terms of a multiple-reflection series which is stable for TE polarization and dielectric gratings to a grating depth of as many as four wavelengths. Li [26] used the R-matrix propagation algorithm to propagate the field through the layers in the modal approach to obtain stable results for deep dielectric and metallic one-dimensional gratings in the conical mount.

Here we use the method which is proposed by Moharam, Pommet, and Grann [12] in 1995 and called enhanced transmittance matrix approach. See (2.33) again and notice the inverse matrix at left. There are some $\mathbf{X}$ terms in this big inverse matrix. Because the elements of $\mathbf{X}$ are $e^{\pm j\beta_m z}$, as some β_m values have large imaginary part, these exponential terms will produce very large or very small elements in this big inverse matrix. And the inver-

sion of this almost singular matrix will produce erroneous results because of truncation errors. Therefore, we would like to remove $\mathbf{X}$ terms from the big inverse matrix.

Consider the last factor ($l = L$) in (2.33), which is

$$\begin{bmatrix} \mathbf{W}_L & \mathbf{W}_L\mathbf{X}_L \\ \mathbf{A}_L\mathbf{W}_L\mathbf{Z}_L & -\mathbf{A}_l\mathbf{W}_l\mathbf{Z}_l\mathbf{X}_l \end{bmatrix} \begin{bmatrix} \mathbf{W}_L\mathbf{X}_L & \mathbf{W}_L \\ \mathbf{A}_L\mathbf{W}_L\mathbf{Z}_L\mathbf{X}_L & -\mathbf{A}_l\mathbf{W}_L\mathbf{Z}_L \end{bmatrix}^{-1} \begin{bmatrix} \mathbf{f_T} \\ \mathbf{g_T} \end{bmatrix} \mathbf{T}$$

$$= \begin{bmatrix} \mathbf{W}_L & \mathbf{W}_L\mathbf{X}_L \\ \mathbf{A}_L\mathbf{W}_L\mathbf{Z}_L & -\mathbf{A}_l\mathbf{W}_l\mathbf{Z}_l\mathbf{X}_l \end{bmatrix} \times \begin{bmatrix} \mathbf{X}_L & 0 \\ 0 & \mathbf{I} \end{bmatrix}^{-1} \begin{bmatrix} \mathbf{W}_L & \mathbf{W}_L \\ \mathbf{A}_L\mathbf{W}_L\mathbf{Z}_L & -\mathbf{A}_l\mathbf{W}_L\mathbf{Z}_L \end{bmatrix}^{-1} \begin{bmatrix} \mathbf{f_T} \\ \mathbf{g_T} \end{bmatrix} \mathbf{T}, \quad (2.34)$$

where $\mathbf{f_T} = \mathbf{I}$ and $\mathbf{g_T} = \mathbf{Z_T}$. The matrix to be inverted has been rewritten as the product of two matrices. The matrix on the right side in the product is well conditioned, however, the left side matrix is ill-conditioned. By defining

$$\begin{bmatrix} \mathbf{W}_L & \mathbf{W}_L \\ \mathbf{A}_L\mathbf{W}_L\mathbf{Z}_L & -\mathbf{A}_l\mathbf{W}_L\mathbf{Z}_L \end{bmatrix}^{-1} \begin{bmatrix} \mathbf{f_L} \\ \mathbf{g_L} \end{bmatrix} \equiv \begin{bmatrix} \mathbf{u}_L \\ \mathbf{v}_L \end{bmatrix}, \quad (2.35)$$

(2.34) could be reduced to

$$\begin{bmatrix} \mathbf{W}_L & \mathbf{W}_L\mathbf{X}_L \\ \mathbf{A}_L\mathbf{W}_L\mathbf{Z}_L & -\mathbf{A}_l\mathbf{W}_l\mathbf{Z}_l\mathbf{X}_l \end{bmatrix} \begin{bmatrix} \mathbf{X}_L^{-1} & 0 \\ 0 & \mathbf{I} \end{bmatrix} \begin{bmatrix} \mathbf{u_L} \\ \mathbf{v_L} \end{bmatrix} \mathbf{T}$$

$$= \begin{bmatrix} \mathbf{W}_L & \mathbf{W}_L\mathbf{X}_L \\ \mathbf{A}_L\mathbf{W}_L\mathbf{Z}_L & -\mathbf{A}_l\mathbf{W}_l\mathbf{Z}_l\mathbf{X}_l \end{bmatrix} \begin{bmatrix} \mathbf{X}_L^{-1}\mathbf{u}_L \\ \mathbf{v}_L \end{bmatrix} \mathbf{T}, \quad (2.36)$$

and by changing variable $\mathbf{T} = \mathbf{u}_L^{-1}\mathbf{X}_L\mathbf{T}_L$, the (2.36) will become

$$\begin{bmatrix} \mathbf{W}_L & \mathbf{W}_L\mathbf{X}_L \\ \mathbf{A}_L\mathbf{W}_L\mathbf{Z}_L & -\mathbf{A}_l\mathbf{W}_l\mathbf{Z}_l\mathbf{X}_l \end{bmatrix} \begin{bmatrix} \mathbf{I} \\ \mathbf{v}_L\mathbf{u}_L^{-1}\mathbf{X}_L \end{bmatrix} \mathbf{T}_L \equiv \begin{bmatrix} \mathbf{f}_L \\ \mathbf{g}_L \end{bmatrix} \mathbf{T}_L. \quad (2.37)$$

Repeat this process for all layers, we obtain

$$\begin{bmatrix} \delta_{i0} \\ \frac{-jk_0\cos\theta}{\sqrt{\epsilon_{r,inc}}}\delta_{i0} \end{bmatrix} + \begin{bmatrix} \mathbf{I} \\ -\mathbf{Z_R} \end{bmatrix} \mathbf{R} = \begin{bmatrix} \mathbf{f}_1 \\ \mathbf{g}_1 \end{bmatrix} \mathbf{T}_1, \tag{2.38}$$

where $\mathbf{T} = \mathbf{u}_L^{-1}\mathbf{X}_L\mathbf{u}_{L-1}^{-1}\mathbf{X}_{L-1}\ldots\mathbf{u}_2^{-1}\mathbf{X}_2\mathbf{u}_1^{-1}\mathbf{X}_1\mathbf{T}_1$. In this formulation, the instability could be avoided successfully because it never inverts the matrices $\mathbf{X}$. The singular-value decomposition technique could be considered in inverting the matrix $\mathbf{u}$ to avoid numerical difficulties because of round-off errors when a large number of layers and a large number of harmonics are used.

In addition, if it needs to plot the field diagram, we have to find coefficients $g_{l,m}^+$ and $g_{l,m}^-$ in every layers by finding $\mathbf{R}$, $\mathbf{T}$ and $\mathbf{T_l}$ of each layer first and then substituting back. After using the skill above, the coefficients in each layer will be

$$\begin{bmatrix} g_{L,m}^+ \\ g_{L,m}^- \end{bmatrix} = \begin{bmatrix} \mathbf{I} \\ \mathbf{v}_L\mathbf{u}_L^{-1}\mathbf{X}_L \end{bmatrix} \mathbf{T}_L, \begin{bmatrix} g_{L-1,m}^+ \\ g_{L-1,m}^- \end{bmatrix} = \begin{bmatrix} \mathbf{I} \\ \mathbf{v}_{L-1}\mathbf{u}_{L-1}^{-1}\mathbf{X}_{L-1} \end{bmatrix} \mathbf{T}_{L-1}, \cdots \tag{2.39}$$

, where $\mathbf{T}_L = \mathbf{u}_{L-1}^{-1}\mathbf{X}_{L-1}\cdots\mathbf{u}_1^{-1}\mathbf{X}_1\mathbf{T}_1$, $\mathbf{T}_{L-1} = \mathbf{u}_{L-2}^{-1}\mathbf{X}_{L-2}\cdots\mathbf{u}_1^{-1}\mathbf{X}_1\mathbf{T}_1$ and so on.

2.2 Finite-Difference Modal Method

In the finite difference modal method, we transfer the continuous functions and their differentiations into discrete points values. The assumption of fields is to express the distribution of spatial fields in grating period direction x and, just like RCWA method, form a set of modes in the propagation direction z which is

$$\psi_m(x,z) \sim \psi_m(x) \times e^{\pm j\beta_m z}, \tag{2.40}$$

where m is the index of mode, β_m is the propagation constant of mode m.

The equation to be solved is Helmholtz equation, $\nabla^2\psi + k_0^2\epsilon_r\psi = 0$ (assuming non-magnetic material). If the structure is infinite and uniform in y-axis and periodic in x-axis, and the direction of fields is in y-axis (i.e. TE or TM polarization), the equation becomes

$$\frac{\partial^2\psi_y(x,z)}{\partial x^2} + \frac{\partial^2\psi_y(x,z)}{\partial z^2} + k_0^2\epsilon_r(x)\psi_y(x,z) = 0. \tag{2.41}$$

Next, substituting (2.40) into (2.41), we obtain

$$\frac{\partial^2\psi_y(x)}{\partial x^2} + k_0^2\epsilon_r(x)\psi_y(x) = \beta^2\psi_y(x). \tag{2.42}$$

After discretizing (2.42), constructing sparse matrix, and solving eigenvalue problem inside each layer, eigenmodes with x distribution inside each layer are found. Then boundary conditions are matched to solve the diffraction efficiencies and plot the field diagrams. In the next subsection, more details about the finite difference inside each layer are offered.

2.2.1 Eigenvalue Problems inside Each Layer

The basic idea of finite difference is to express the differentiation of a field point by itself and it's adjacent points, as in Fig. 2.4. Being different from

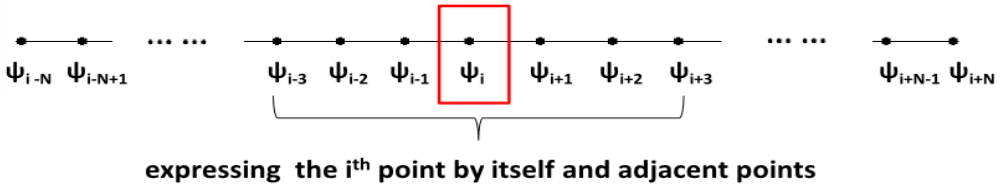

Figure 2.4: One-dimensional discretization.

RCWA, the convergence of FD method could be improved by considering more adjacent points, i.e. extending to higher orders of Taylor series expansion. If we use $(2N+1)$ points to approximate the differentiation of one field point, ψ_i, we have to know the relation between the field at those points and ψ_i and its derivatives up to $(2N)$th order as

$$\begin{bmatrix} \psi_{i-N} \\ \vdots \\ \psi_i \\ \vdots \\ \psi_{i+N} \end{bmatrix} = \begin{bmatrix} u_{-N,0} & u_{-N,1} & \dots & u_{-N,2N} \\ \vdots & \vdots & \ddots & \vdots \\ u_{N,0} & u_{N,1} & \dots & u_{N,2N} \end{bmatrix} \begin{bmatrix} \psi_i \\ \vdots \\ \psi_i^{(j)} \\ \vdots \\ \psi_i^{2N} \end{bmatrix} + O(h^{2N+1}). \quad (2.43)$$

And then inverting the matrix to find ψ_i'' with truncation error $O(h^{2N+1}/h^2) = O(h^{2N-1})$. As the grids are uniformly positioned, the truncation error will become $O(h^{2N})$. Here we use central difference scheme, but it is not necessary. We can use forward-difference or backward-difference as well.

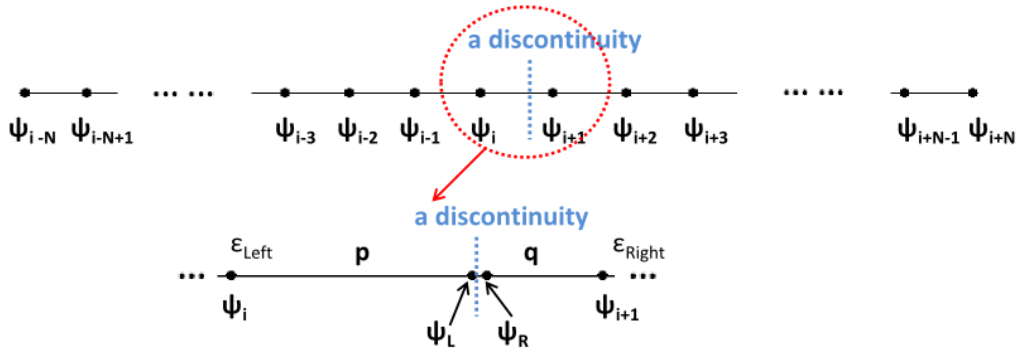

Figure 2.5: Sketch of a discontinuity between sampled points.

However, there are some discontinuities in each grating layer. Unlike RCWA, which use Fourier expansion to illustrate the change of permittivity, here we match boundary conditions at these discontinuities to arbitrary higher order. As in Fig. 2.5, if we want to express the $(i+1)$th points in terms of each order of the ith point, we expand each order of $(i+1)$th field ψ_{i+1} by each order of ψ_R, i.e.

$$\mathbf{\Psi}_{i+1} \equiv \begin{bmatrix} \psi_{i+1} \\ \psi'_{i+1} \\ \psi''_{i+1} \\ \psi^{(3)}_{i+1} \\ \vdots \\ \psi^{(2N)}_{i+1} \end{bmatrix} = \begin{bmatrix} 1 & q & \frac{q^2}{2!} & \frac{q^3}{3!} & \cdots & \frac{q^{2N}}{(2N)!} \\ 0 & 1 & q & \frac{q^2}{2!} & \cdots & \frac{q^{2N-1}}{(2N-1)!} \\ 0 & 0 & 1 & q & \cdots & \frac{q^{2N-2}}{(2N-2)!} \\ 0 & 0 & 0 & 1 & \cdots & \frac{q^{2N-3}}{(2N-3)!} \\ \vdots & \vdots & \vdots & \vdots & \ddots & \vdots \\ 0 & 0 & 0 & 0 & \cdots & 1 \end{bmatrix} \begin{bmatrix} \psi_R \\ \psi'_R \\ \psi''_R \\ \psi^{(3)}_R \\ \vdots \\ \psi^{(2N)}_R \end{bmatrix} \equiv \mathbf{M}_{i+1:R}\mathbf{\Psi}_R, \tag{2.44}$$

and each order of ψ_L by each order of (i)th field ψ_i,

$$\mathbf{\Psi}_L \equiv \begin{bmatrix} \psi_L \\ \psi'_L \\ \psi''_L \\ \psi_L^{(3)} \\ \vdots \\ \psi_L^{(2N)} \end{bmatrix} = \begin{bmatrix} 1 & p & \frac{p^2}{2!} & \frac{p^3}{3!} & \cdots & \frac{p^{2N}}{(2N)!} \\ 0 & 1 & p & \frac{p^2}{2!} & \cdots & \frac{p^{2N-1}}{(2N-1)!} \\ 0 & 0 & 1 & p & \cdots & \frac{p^{2N-2}}{(2N-2)!} \\ 0 & 0 & 0 & 1 & \cdots & \frac{p^{2N-3}}{(2N-3)!} \\ \vdots & \vdots & \vdots & \vdots & \ddots & \vdots \\ 0 & 0 & 0 & 0 & \cdots & 1 \end{bmatrix} \begin{bmatrix} \psi_i \\ \psi'_i \\ \psi''_i \\ \psi_i^{(3)} \\ \vdots \\ \psi_i^{(2N)} \end{bmatrix} \equiv \mathbf{M}_{L:i}\mathbf{\Psi}_i. \tag{2.45}$$

And the main problem is how to connect $\mathbf{\Psi}_L$ and $\mathbf{\Psi}_R$, i.e., because

$$\mathbf{\Psi}_{i+1} = \mathbf{M}_{i+1:R}\mathbf{M}_{R:L}\mathbf{M}_{L:i}\mathbf{\Psi}_i, \tag{2.46}$$

we need to find the matrix $\mathbf{M}_{R:L}$. Next, we will derive the arbitrary higher order boundary condition for (2.42).

A. Arbitrary Higher Order Boundary Condition [23] [24]

Generally, considering the discontinuous parameters of materials are not only permittivity ϵ but also permeability μ. The zeroth-order boundary condition is continuing of tangential fields

$$\psi_R = \psi_L, \tag{2.47}$$

where $\psi = E_y$ for TE and H_y for TM, and subscript R and L mean points infinitesimally close to the interface on the left and right, respectively. Next, for the first-order boundary condition, we use Maxwell's equations $\mathbf{H} = \frac{-1}{j\omega\mu_0\mu_r}\nabla \times \mathbf{E}$ and $H_{z,R} = H_{z,L}$ for TE; $\mathbf{E} = \frac{1}{j\omega\epsilon_0\epsilon_r}\nabla \times \mathbf{H}$ and $E_{z,R} = E_{z,L}$ for

TM to derive

$$\psi'_R = a\psi'_L, \tag{2.48}$$

where $a = \frac{\mu_R}{\mu_L}$ for TE and $a = \frac{\epsilon_R}{\epsilon_L}$ for TM. The second-order boundary condition is derived from Helmholtz equation, i.e. $\psi''_R + \omega^2\mu_R\epsilon_R\psi_R = \beta^2\psi_R$ and $\psi''_L + \omega^2\mu_L\epsilon_L\psi_L = \beta^2\psi_L$. By using (2.47), we could obtain

$$\psi''_R = \psi''_L + b\psi_L, \tag{2.49}$$

where $b = \omega^2(\mu_L\epsilon_L - \mu_R\epsilon_R)$. For the third-order boundary condition, the Helmoholtz equation is differentiated on each side to get $\psi^3_R + \omega^2\mu_R\epsilon_R\psi'_R = \beta^2\psi'_R$ and $\psi^3_L + \omega^2\mu_L\epsilon_L\psi'_L = \beta^2\psi'_L$. After substituting (2.48) into above two equations, we obtain

$$\psi^{(3)}_R = a(\psi^{(3)}_L + b\psi'_L). \tag{2.50}$$

We proceed to find the 4th order boundary relation. In the derivation here, we could regard the term $(\partial^2_x + \omega^2\mu\epsilon)$ as an operator, which is equivalent to the term β^2, i.e.,

$$(\partial^2_x + \omega^2\mu_R\epsilon_R)(\partial^2_x + \omega^2\mu_R\epsilon_R)\psi_R = \beta^2\beta^2\psi_R \text{ and}$$

$$(\partial^2_x + \omega^2\mu_L\epsilon_L)(\partial^2_x + \omega^2\mu_L\epsilon_L)\psi_L = \beta^2\beta^2\psi_L.$$

Combining the above equations with (2.47) and (2.49), we get the relation

$$\psi^{(4)}_R = \psi^{(4)}_L + 2b\psi''_L + b^2\psi_L. \tag{2.51}$$

After repeating the above processes, we will generalize the continuity relation which could be expressed in matrix form as

$$\mathbf{M}_{R:L} = \begin{bmatrix} 1 & 0 & 0 & 0 & \cdots & 0 \\ 0 & a & 0 & 0 & \cdots & 0 \\ b & 0 & 1 & 0 & \cdots & 0 \\ 0 & ab & 0 & a & \cdots & 0 \\ \vdots & \vdots & \vdots & \vdots & \ddots & \vdots \\ 0 & C_0^{N-1}ab^{N-1} & 0 & C_1^{N-1}ab^{N-2} & \cdots & 0 \\ C_0^N b^N & 0 & C_1^N b^{N-1} & 0 & \cdots & C_N^N \end{bmatrix}, \quad (2.52)$$

and make $\mathbf{\Psi}_R = \mathbf{M}_{R:L}\mathbf{\Psi}_L$. Finally, substitute it into (2.46) and then know how to express ψ_{i+1} by each order of ψ_i. Put this expression back into (2.43) and, after finding all the elements of (2.43), invert it to obtain the expression of ψ_i''.

B. Periodic Boundary Condition

It had been proved by Bloch in 1928 that, for a periodic potential system, the eigenstate can be expressed as the product of a plane wave envelope function and a periodic function which has the same periodicity, i.e.

$$\psi_{\mathbf{k}}(\mathbf{r}) = e^{-j\mathbf{k}\cdot\mathbf{r}} \times u_{\mathbf{k}}(\mathbf{r}), \quad (2.53)$$

where $\mathbf{k}$ is reciprocal periodic vector and $u_{\mathbf{k}}(\mathbf{r})$ satisfies $u_{\mathbf{k}}(\mathbf{r}) = u_k(\mathbf{r} + \mathbf{\Lambda})$ where $\mathbf{\Lambda}$ is the grating vector. When the structure is periodic, we should not ignore the points just outside the calculating region. Instead, we add the phase term on them, and put them in the sparse matrix.

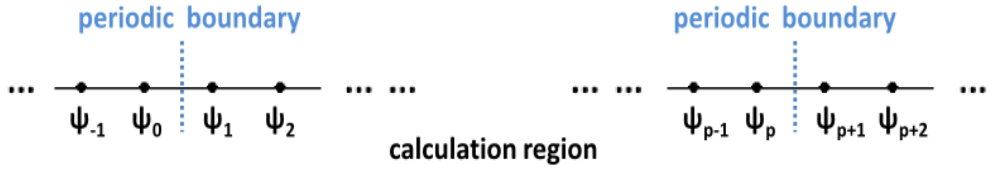

Figure 2.6: Periodic boundaries.

As the Fig. 2.6, after doing finite difference, we obtain the expression of ψ_1'', which is

$$\psi_1'' = \cdots + c_0\psi_0 + c_1\psi_1 + c_2\psi_2 + \cdots . \tag{2.54}$$

Although ψ_0 is out of the calculating, it is a replicated point of ψ_p with a displacement of Λ, where p is the number of total calculated points. Therefore, we could express $\psi_0 = e^{-jk(-\Lambda)} \times \psi_p$, $\psi_{-1} = e^{-jk(-\Lambda)} \times \psi_{p-1}$ and so on. Finally, the expression of ψ_1'' is

$$\psi_1'' = \cdots + c_0 e^{-jk(-\Lambda)} \times \psi_p + c_1\psi_1 + c_2\psi_2 + \cdots \tag{2.55}$$

instead of

$$\psi_1'' = \cdots + 0 + c_1\psi_1 + c_2\psi_2 + \cdots . \tag{2.56}$$

And these terms will appear on the corner of sparse matrix for 1D finite difference.

C. Generalized Douglas Finite-Difference Scheme

There is a clever way to enhance the convergence of truncation error by two order. The main idea of this method is considering two additional

derivatives. More specifically, for $(2N+1)$ points approximation, we expand each points to $(2N+2)$th order instead of $(2N)$th order. Then using first $(2N)$th order terms to find 2nd order differential expression (i.e. operator D_x^2) and define this expression as $\psi''_{i,pseudo}$. Next, operate this expression on the ψ_i to get actual ψ''_i, which includes even higher order terms. Finally, approximate $\psi''_{i,pseudo}$ to be ψ''_i. The formulation can be expressed as

$$\begin{aligned} D_x^2\psi_i &= \psi''_{i,pseudo} + g_1\psi_i^{2N+1} + g_2\psi_i^{2N+2} + O(h^{2N+3}) \\ &\approx \psi''_i + g_1\psi_i^{2N+1} + g_2\psi_i^{2N+2} + O(h^{2N+3}) \\ &= (1 + g_1 D_x^{2N-1} + g_2 D_x^{2N})\psi''_i + O(h^{2N+3}) \\ \Rightarrow \quad \psi''_i &= \frac{D_x^2}{1 + g_1 D_x^{2N-1} + g_2 D_x^{2N}}\psi_i, \end{aligned} \tag{2.57}$$

with $O(h^{2N+3})/h^2 = O(h^{2N+1})$ and $O(h^{2N+2})$ for central difference and uniform grid cutting. After substituting this refined operator back into (2.42), we obtain

$$\begin{aligned} \frac{\partial^2\psi_y(x)}{\partial x^2} + k_0^2\epsilon_r(x)\left(1 + g_1\frac{\partial^{2N-1}}{\partial x^{2N-1}} + g_2\frac{\partial^{2N}}{\partial x^{2N}}\right)\psi_y(x) \\ = \beta^2\left(1 + g_1\frac{\partial^{2N-1}}{\partial x^{2N-1}} + g_2\frac{\partial^{2N}}{\partial x^{2N}}\right)\psi_y(x). \end{aligned} \tag{2.58}$$

2.2.2 Evaluation of Diffraction Efficiencies

Being the same as RCWA, we solve the eigenvalues problem after constructing the sparse matrices in every layers and get the eigenvalues and eigenvector matrices $\mathbf{W}$. The difference between eigenvector matrices $\mathbf{W}$ of these

two method is, for RCWA, columns of $[w_{im}]$ means which modes and rows of $[w_{im}]$ means which orders; for finite difference, columns of $[w_{pm}]$ means which modes and rows of $[w_{pm}]$ means which positions.

After solving the eigenvalues problem of each layer, we obtain the mode field expression in reflection region

$$\psi_y^R = \sum_m w_{pm}^R (a_m^+ e^{-j\beta_m^R z} + R_m^- e^{j\beta_m^R z}), \tag{2.59}$$

where $a_m^+ = \langle w_{pm}^R | \psi_{inc} \rangle$ (projection of incident field on each mode), in lth grating layer

$$\psi_{l,y}^G = \sum_m w_{pm}^l (g_{l,m}^+ e^{-j\beta_m^l (z - z_{l-1})} + g_m^- e^{j\beta_m^l (z - z_l)}), \tag{2.60}$$

and in transmission region

$$\psi_y^T = \sum_m w_{pm}^T (T_m^+ e^{-j\beta_m^T (z - t_g)}), \tag{2.61}$$

where t_g for multi-layer approximation means the total height of grating. Again, $\psi_y = E_y$ for TE and $\psi_y = H_y$ for TM.

Next, using Maxwell's equations to find field H_x for TE or field E_x for TM, then matching boundary condition for each interface between two adjacent layers, we obtain the final matrix

$$\begin{bmatrix} \mathbf{W_R} \\ \mathbf{A_R W_R Z_R} \end{bmatrix} \mathbf{a}^+ + \begin{bmatrix} \mathbf{W_R} \\ -\mathbf{A_R W_R Z_R} \end{bmatrix} \mathbf{R} = \prod_{l=1}^{L} \begin{bmatrix} \mathbf{W}_l & \mathbf{W}_l \mathbf{X}_l \\ \mathbf{A}_l \mathbf{W}_l \mathbf{Z}_l & -\mathbf{A}_l \mathbf{W}_l \mathbf{Z}_l \mathbf{X}_l \end{bmatrix} \times \begin{bmatrix} \mathbf{W}_l \mathbf{X}_l & \mathbf{W}_l \\ \mathbf{A}_l \mathbf{W}_l \mathbf{Z}_l \mathbf{X}_l & -\mathbf{A}_l \mathbf{W}_l \mathbf{Z}_l \end{bmatrix}^{-1} \begin{bmatrix} \mathbf{W_T} \\ \mathbf{A_T W_T Z_T} \end{bmatrix} \mathbf{T}, \tag{2.62}$$

where $\mathbf{W_l} = [w^l_{pm}]$, $\mathbf{A_l} = diag[1/\epsilon_{r,l}]$ for TM; $\mathbf{I}$ for TE,$\mathbf{Z_l} = diag[-j\beta^l_m]$ and $\mathbf{X_l} = diag[e^{-j\beta^l_m(z_l - z_{l-1})}]$.

The enhanced transmittance matrix approach mentioned in subsection 2.1.4 to make the numerical calculation stable could be used as finding $\mathbf{R}$ and $\mathbf{T}$. Finally, we could use definition (2.27) to find diffraction efficiencies and plot field diagrams.

2.3 Two-Dimensional Finite-Difference Method

For TM polarization, using the method of 1D FD with multi-layer may suffer some instabilities without proper discretization. Both for comparing and revising, we try another method, which calculates arbitrary gratings by two-dimensional finite difference (2DFD), to simulate the same diffraction problems.

The calculating geometry is shown as Fig. 2.7. We use periodic boundary condition on edges of periodic direction, and perfect matched layer besides the edges of propagation direction.

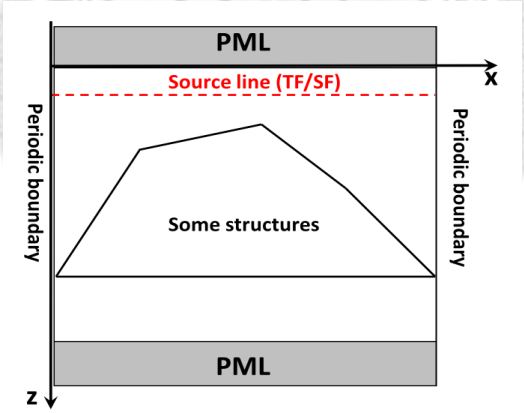

Figure 2.7: Configuration of two-dimensional finite difference.

2.3.1 Discretizing Maxwell's Equation

Consider TM polarization again. Maxwell's equations will become

$$j\omega\epsilon_0\epsilon_r(x)E_z = \frac{\partial H_y}{\partial x}, \tag{2.63}$$

$$j\omega\epsilon_0\epsilon_r(x)E_x = -\frac{\partial H_y}{\partial z}, \tag{2.64}$$

and

$$j\omega\mu_0 H_y = \frac{\partial E_z}{\partial x} - \frac{\partial E_x}{\partial z}. \tag{2.65}$$

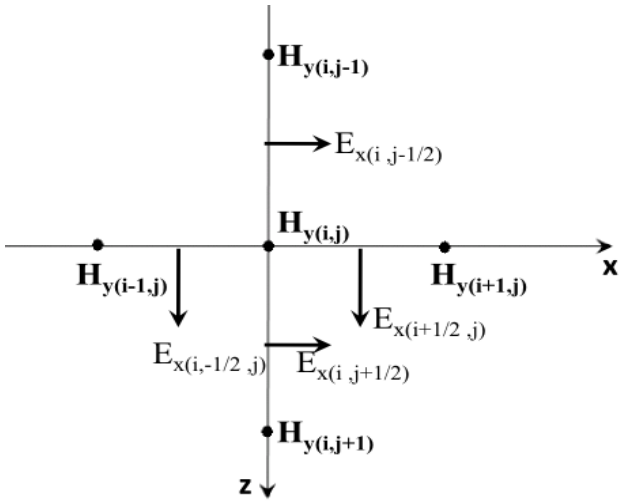

Figure 2.8: Two-dimensional discretization.

A. Averaging permittivity

According to Fig. 2.8, above equations can be discretized into

$$j\omega\epsilon_0\epsilon_{r(i+\frac{1}{2},j)}E_{z(i+\frac{1}{2},j)} = \frac{H_{y(i+1,j)} - H_{y(i,j)}}{\Delta x}, \tag{2.66}$$

$$j\omega\epsilon_0\epsilon_{r(i-\frac{1}{2},j)}E_{z(i-\frac{1}{2},j)} = \frac{H_{y(i,j)} - H_{y(i-1,j)}}{\Delta x}, \tag{2.67}$$

$$j\omega\epsilon_0\epsilon_{r(i,j+\frac{1}{2})}E_{x(i,j+\frac{1}{2})} = -\frac{H_{y(i,j+1)} - H_{y(i,j)}}{\Delta z}, \tag{2.68}$$

$$j\omega\epsilon_0\epsilon_{r(i,j-\frac{1}{2})}E_{x(i,j-\frac{1}{2})} = -\frac{H_{y(i,j)} - H_{y(i,j-1)}}{\Delta z}, \tag{2.69}$$

and

$$j\omega\mu_0 H_{y(i,j)} = \frac{E_{z(i+\frac{1}{2},j)} - E_{z(i-\frac{1}{2},j)}}{\Delta x} - \frac{E_{x(i,j+\frac{1}{2})} - E_{x(i,j-\frac{1}{2})}}{\Delta z}. \tag{2.70}$$

After substituting (2.66), (2.67), (2.68) and (2.69) into (2.71), we obtain

$$\begin{aligned}\frac{1}{\Delta x^2}\left[\frac{H_{y(i+1,j)}}{\epsilon_{r(i+\frac{1}{2},j)}} - \left(\frac{1}{\epsilon_{r(i+\frac{1}{2},j)}} + \frac{1}{\epsilon_{r(i-\frac{1}{2},j)}}\right) H_{y(i,j)} + \frac{H_{y(i-1,j)}}{\epsilon_{r(i-\frac{1}{2},j)}}\right] \\ + \frac{1}{\Delta z^2}\left[\frac{H_{y(i,j+1)}}{\epsilon_{r(i,j+\frac{1}{2})}} - \left(\frac{1}{\epsilon_{r(i,j+\frac{1}{2})}} + \frac{1}{\epsilon_{r(i,j-\frac{1}{2})}}\right) H_{y(i,j)} + \frac{H_{y(i,j-1)}}{\epsilon_{r(i,j-\frac{1}{2})}}\right] \\ + \omega^2\mu_0\epsilon_0 H_{y(i,j)} = 0.\end{aligned} \tag{2.71}$$

where $\epsilon_{r(i,j)}$ are calculated by averaging the permittivities in the region of $x_{i-\frac{1}{2}} \le x \le x_{i+\frac{1}{2}}$ and $z_{i-\frac{1}{2}} \le z \le z_{i+\frac{1}{2}}$. For simplicity and generality, I put many points in this region, classify the regions they belong to, and calculate the arithmetic mean of them. As in Fig. 2.9, the value of permittivity ϵ at position (i, j) will become

$$\epsilon_{(i,j)} = \frac{\epsilon_1 N_1 + \epsilon_2 N_2}{N_1 + N_2}, \tag{2.72}$$

or sometimes

$$\epsilon_{(i,j)} = \left(\frac{N_1/\epsilon_1 + N_2/\epsilon_2}{N_1 + N_2}\right)^{-1}, \tag{2.73}$$

where ϵ_k $(k = 1, 2)$ means the permittivity at one side of the discontinuity and N_k is the amount of points with this permittivity value.

B. Considering boundary condition [27]

Although permittivity approximated by averaging is applicable to structures with small permittivity difference, it has difficulty in accurately model-

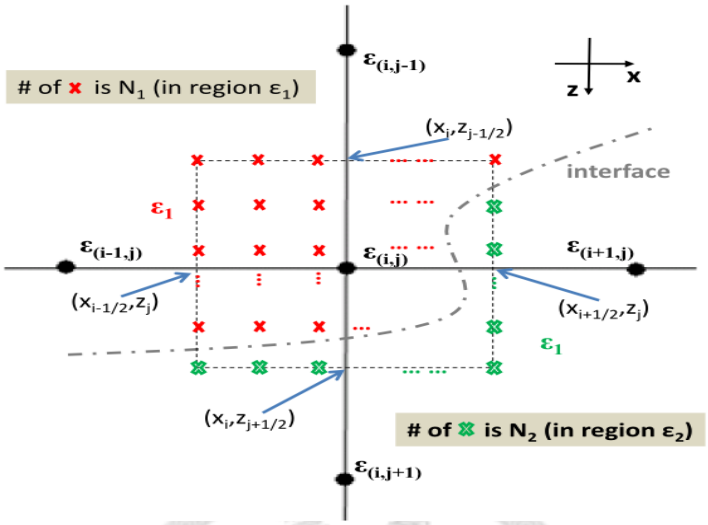

Figure 2.9: Method of averaging permittivity.

ing field behaviors near abrupt interfaces. Moreover, recent advancement of nanoprocess make step-index structures practical for next-generation optical design, indicating that a modified modeling formulation dedicated to step-permittivity problem is required. This modification will be demonstrated by taking account of the boundary condition, i.e. the continuity of tangential fields **E** and **H** and normal fields **D** and **B** (in no source region).

Consider the region without sources depicted as Fig. 2.7. If there is no discontinuity inside the mesh of point (i, j), from (2.71), we obtain

$$\frac{H_{y(i+1,j)} - 2H_{y(i,j)} + H_{y(i-1,j)}}{\Delta x^2} + \frac{H_{y(i,j+1)} - 2H_{y(i,j)} + H_{y(i,j-1)}}{\Delta y^2} + \omega^2 \mu_0 \epsilon_0 \epsilon_{(i,j)} H_{y(i,j)} = 0. \quad (2.74)$$

However, if discontinuities exist, we put the mesh points on the interfaces or

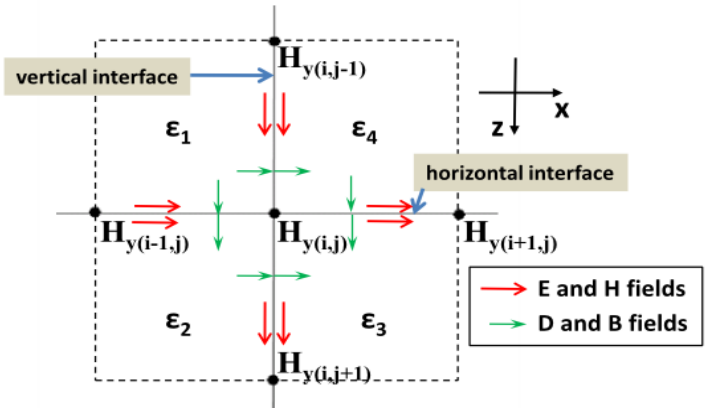

Figure 2.10: Continuity of fields on interfaces.

corners and match boundary condition, as Fig. 2.10. Here the most complicated configuration for rectangular structures, which includes four different kinds of medium, will be used to discuss.

Consider the interface between ϵ_1 and ϵ_2. In the homogeneous parts of these two medium, the Helmholtz equation are

$$\frac{\partial^2 H_y}{\partial x^2} + \frac{\partial^2 H_y}{\partial z^2} + \omega^2 \mu_0 \epsilon_0 \epsilon_1 H_y = 0 \quad \text{and} \quad \frac{\partial^2 H_y}{\partial x^2} + \frac{\partial^2 H_y}{\partial z^2} + \omega^2 \mu_0 \epsilon_0 \epsilon_2 H_y = 0, \tag{2.75}$$

which can be discretized into

$$\frac{\left.\frac{\partial H_y}{\partial x}\right|_1 - \frac{H_{y(i,j)} - H_{y(i-1,j)}}{\Delta x}}{\Delta x/2} + \frac{\left.\frac{\partial H_y}{\partial z}\right|_1 - \frac{H_{y(i,j)} - H_{y(i,j-1)}}{\Delta z}}{\Delta z/2} + \omega^2 \mu_0 \epsilon_0 \epsilon_1 H_{y(i,j)} = 0 \tag{2.76}$$

and

$$\frac{\left.\frac{\partial H_y}{\partial x}\right|_2 - \frac{H_{y(i,j)} - H_{y(i-1,j)}}{\Delta x}}{\Delta x/2} + \frac{\frac{H_{y(i,j+1)} - H_{y(i,j)}}{\Delta z} - \left.\frac{\partial H_y}{\partial z}\right|_2}{\Delta z/2} + \omega^2 \mu_0 \epsilon_0 \epsilon_2 H_{y(i,j)} = 0. \quad (2.77)$$

Next, because the continuity of tangential **E** fields (means E_x here) and normal **D** (means D_z here), we know that

$$\frac{1}{\epsilon_1}\left.\frac{\partial H_y}{\partial z}\right|_1 = \frac{1}{\epsilon_2}\left.\frac{\partial H_y}{\partial z}\right|_2 \quad \text{and} \quad \left.\frac{\partial H_y}{\partial x}\right|_1 = \left.\frac{\partial H_y}{\partial x}\right|_2. \quad (2.78)$$

Substitute (2.78) into (2.76) and (2.77) and we could obtain

$$\frac{2}{\Delta x}\left.\frac{\partial H_y}{\partial x}\right|_1 - \frac{2H_{y(i,j)} - 2H_{y(i-1,j)}}{\Delta x^2} + \omega^2 \mu_0 \epsilon_0 \frac{2\epsilon_1 \epsilon_2}{\epsilon_1 + \epsilon_2} H_{y(i,j)} + \frac{\frac{2\epsilon_1}{\epsilon_1 + \epsilon_2} H_{y(i,j+1)} - 2H_{y(i,j)} + \frac{2\epsilon_2}{\epsilon_1 + \epsilon_2} H_{y(i,j-1)}}{\Delta z^2} = 0. \quad (2.79)$$

After doing the similar processes for the last three interfaces between ϵ_2 and ϵ_3, ϵ_3 and ϵ_4, and ϵ_4 and ϵ_1, we get

$$-\frac{2}{\Delta z}\left.\frac{\partial H_y}{\partial z}\right|_2 + \frac{2H_{y(i,j+1)} - 2H_{y(i,j)}}{\Delta z^2} + \omega^2 \mu_0 \epsilon_0 \frac{2\epsilon_2 \epsilon_3}{\epsilon_2 + \epsilon_3} H_{y(i,j)} + \frac{\frac{2\epsilon_2}{\epsilon_2 + \epsilon_3} H_{y(i+1,j)} - 2H_{y(i,j)} + \frac{2\epsilon_3}{\epsilon_2 + \epsilon_3} H_{y(i-1,j)}}{\Delta x^2} = 0, \quad (2.80)$$

$$-\frac{2}{\Delta x}\left.\frac{\partial H_y}{\partial x}\right|_3 + \frac{2H_{y(i+1,j)} - 2H_{y(i,j)}}{\Delta x^2} + \omega^2 \mu_0 \epsilon_0 \frac{2\epsilon_3 \epsilon_4}{\epsilon_3 + \epsilon_4} H_{y(i,j)} + \frac{\frac{2\epsilon_4}{\epsilon_3 + \epsilon_4} H_{y(i,j+1)} - 2H_{y(i,j)} + \frac{2\epsilon_3}{\epsilon_3 + \epsilon_4} H_{y(i,j-1)}}{\Delta z^2} = 0, \quad (2.81)$$

and

$$\frac{2}{\Delta z}\left.\frac{\partial H_y}{\partial z}\right|_4 - \frac{2H_{y(i,j)} - 2H_{y(i,j-1)}}{\Delta z^2} + \omega^2\mu_0\epsilon_0\frac{2\epsilon_4\epsilon_1}{\epsilon_4+\epsilon_1}H_{y(i,j)} + \frac{\frac{2\epsilon_1}{\epsilon_4+\epsilon_1}H_{y(i+1,j)} - 2H_{y(i,j)} + \frac{2\epsilon_4}{\epsilon_4+\epsilon_1}H_{y(i-1,j)}}{\Delta x^2} = 0. \quad (2.82)$$

Equations (2.79)-(2.82) are the results derived from $\nabla \times \mathbf{H} = j\omega\mathbf{D}$.

Finally, Faraday's law, i.e. $\nabla \times \mathbf{E} = -j\omega\mathbf{B}$, will be considered and taken surface integration on both side, which means

$$\int_S \nabla \times \mathbf{E} \cdot d\mathbf{s} = -j\omega \int_S \mathbf{B} \cdot d\mathbf{s}. \quad (2.83)$$

By taking Stoke's theorem into account, we obtain

$$\oint_L \mathbf{E} \cdot d\mathbf{l} = -j\omega \int_S \mathbf{B} \cdot d\mathbf{s}. \quad (2.84)$$

While the area of integration approaches zero, $\oint \mathbf{E} \cdot d\mathbf{l} \to 0$ and we would get

$$\left(\frac{1}{\epsilon_1}+\frac{1}{\epsilon_2}\right)\left.\frac{\partial H_y}{\partial x}\right|_1 + \left(\frac{1}{\epsilon_2}+\frac{1}{\epsilon_3}\right)\left.\frac{\partial H_y}{\partial z}\right|_2 - \left(\frac{1}{\epsilon_3}+\frac{1}{\epsilon_4}\right)\left.\frac{\partial H_y}{\partial x}\right|_3 - \left(\frac{1}{\epsilon_4}+\frac{1}{\epsilon_1}\right)\left.\frac{\partial H_y}{\partial z}\right|_4 = 0. \quad (2.85)$$

After substituting (2.79)-(2.82) into (2.85), the Helmholtz equation will become

$$\frac{\frac{\epsilon_3+\epsilon_4}{2\epsilon_3\epsilon_4}H_{y(i+1,j)} - \left(\frac{\epsilon_3+\epsilon_4}{2\epsilon_3\epsilon_4}+\frac{\epsilon_1+\epsilon_2}{2\epsilon_1\epsilon_2}\right)H_{y(i,j)} + \frac{\epsilon_1+\epsilon_2}{2\epsilon_1\epsilon_2}H_{y(i-1,j)}}{\Delta x^2} + \frac{\frac{\epsilon_2+\epsilon_3}{2\epsilon_2\epsilon_3}H_{y(i,j+1)} - \left(\frac{\epsilon_2+\epsilon_3}{2\epsilon_2\epsilon_3}+\frac{\epsilon_1+\epsilon_4}{2\epsilon_1\epsilon_4}\right)H_{y(i,j)} + \frac{\epsilon_1+\epsilon_4}{2\epsilon_1\epsilon_4}H_{y(i,j-1)}}{\Delta z^2} + \omega^2\mu_0\epsilon_0 H_{y(i,j)} = 0. \quad (2.86)$$

2.3.2 Mesh Truncation

Sometimes it needs to solve infinite structures such as free space, periodic structure, etc, in the electromagnetic problems. In principle, as discretizing the infinite structure, it needs to use infinite mesh points, but it is impossible in reality because of finite capacity of memory. Therefore, some methods have been proposed to use finite mesh points but not deviate from the original configuration of the problem. These techniques are called methods of mesh truncation.

A. Periodic Boundary Condition

To calculate problems of periodic structure, it only needs to consider one period of the structure and use periodic boundary condition. The concept of this part has been mentioned in subsection 2.2.1.

B. Perfectly Matched Layer (PML): Graded Edition [27]

For finite-difference time-domain method (FDTD), while calculating an infinite or semi-infinite space, basically we could use a very large region with PEC or PMC to approach it although it will consume a lot of memory. For finite-difference frequency-domain method (FDFD), what we find are the steady state solutions, the electromagnetic waves are inevitable to reach the PEC or PMC and reflect. Therefore, it will fail totally in FDFD calculation.

There are two main kinds of methods applied to simulate infinite spaces. One is differential-based absorbing boundary (DABC), like Mur ABC, Hig-

don ABC, Liao ABC etc. However, the reduction of reflected waves is not optimal as these methods are used. The other one is material based absorbing boundary condition (MABC), which adding some loss terms in the material parameter such as permittivity and permeability. Some examples of this method are PML, UPML (Uniaxial PML), etc. Here, PML is used in our simulation. PML, which is proposed by Bérenger [28] in 1994 and applied on finite-difference time-domain method, is one of the most popular method to absorb the outgoing electromagnetic waves.

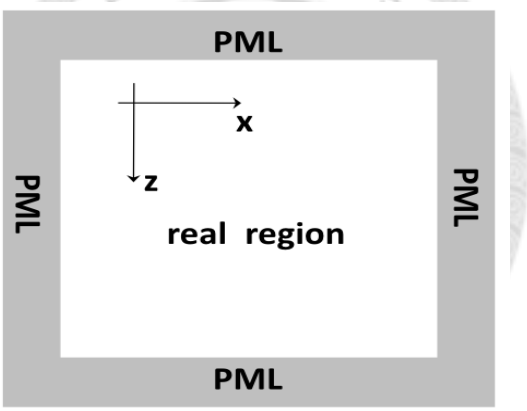

Figure 2.11: A real region surrounded by PML to approximate the infinite region.

Consider the most general case which the PML surround the real region, as in Fig. 2.11. For TM polarization (H_y,E_x,E_z), time harmonic oscillation $e^{j\omega t}$ and loss terms σ^* for permeability and σ for permittivity, the Maxwell's

equations will become

$$j\omega\mu_0 H_{yx} + \sigma_x^* H_{yx} = \frac{\partial E_z}{\partial x}, \tag{2.87}$$

$$j\omega\mu_0 H_{yz} + \sigma_z^* H_{yz} = -\frac{\partial E_x}{\partial z}, \tag{2.88}$$

$$j\omega\epsilon_0\epsilon_r E_x + \sigma_z E_x = -\frac{\partial H_y}{\partial z}, \tag{2.89}$$

and

$$j\omega\epsilon_0\epsilon_r E_z + \sigma_x E_z = \frac{\partial H_y}{\partial x}, \tag{2.90}$$

where $H_y = H_{yx} + H_{yz}$. Equations (2.87) and (2.90) mean the electromagnetic waves which propagate along x-direction; (2.88) and (2.89) mean the electromagnetic waves which propagate along z-direction. Equations (2.87) and (2.88) could be combined to be

$$H_y = \frac{1}{j\omega\mu_0 + \sigma_x^*}\frac{\partial E_z}{\partial x} - \frac{1}{j\omega\mu_0 + \sigma_z^*}\frac{\partial E_x}{\partial z}. \tag{2.91}$$

Then discretizing (2.91), (2.89) and (2.90) to obtain

$$H_{y(i,j)} = \frac{1}{j\omega\mu_0 + \sigma^*_{x(i,j)}}\frac{E_{z(i+\frac{1}{2},j)} - E_{z(i-\frac{1}{2},j)}}{\Delta x} - \frac{1}{j\omega\mu_0 + \sigma^*_{z(i,j)}}\frac{E_{x(i,j+\frac{1}{2})} - E_{x(i,j-\frac{1}{2})}}{\Delta z}, \tag{2.92}$$

$$(j\omega\epsilon_0\epsilon_{r(i+\frac{1}{2},j)} + \sigma_{x(i+\frac{1}{2},j)})E_{z(i+\frac{1}{2},j)} = \frac{H_{y(i+1,j)} - H_{y(i,j)}}{\Delta x}, \tag{2.93}$$

$$(j\omega\epsilon_0\epsilon_{r(i-\frac{1}{2},j)} + \sigma_{x(i-\frac{1}{2},j)})E_{z(i-\frac{1}{2},j)} = \frac{H_{y(i,j)} - H_{y(i-1,j)}}{\Delta x}, \tag{2.94}$$

$$(j\omega\epsilon_0\epsilon_{r(i,j+\frac{1}{2})} + \sigma_{z(i,j+\frac{1}{2})})E_{x(i,j+\frac{1}{2})} = -\frac{H_{y(i,j+1)} - H_{y(i,j)}}{\Delta z}, \tag{2.95}$$

and

$$(j\omega\epsilon_0\epsilon_{r(i,j-\frac{1}{2})} + \sigma_{z(i,j-\frac{1}{2})})E_{x(i,j-\frac{1}{2})} = -\frac{H_{y(i,j)} - H_{y(i,j-1)}}{\Delta z}. \tag{2.96}$$

Let $\mu_{\alpha c} = 1 + \frac{\sigma^*_\alpha}{j\omega\mu_0}$ and $\epsilon_{\alpha c} = \epsilon_r + \frac{\sigma_\alpha}{j\omega\epsilon_0}$, where $\alpha = x$ or z. Next, Substitute (2.93)-(2.96) into (2.92) and get

$$\frac{1}{\Delta x^2 \mu_{xc(i,j)}}\left[\frac{H_{y(i+1,j)}}{\epsilon_{xc(i+1/2,j)}} - \left(\frac{1}{\epsilon_{xc(i+1/2,j)}} + \frac{1}{\epsilon_{xc(i-1/2,j)}}\right) H_{y(i,j)} + \frac{H_{y(i-1,j)}}{\epsilon_{xc(i-1/2,j)}}\right]$$
$$+\frac{1}{\Delta z^2 \mu_{xc(i,j)}}\left[\frac{H_{y(i,j+1)}}{\epsilon_{zc(i,j+1/2)}} - \left(\frac{1}{\epsilon_{zc(i,j+1/2)}} + \frac{1}{\epsilon_{zc(i,j-1/2)}}\right) H_{y(i,j)} + \frac{H_{y(i,j-1)}}{\epsilon_{zc(i,j-1/2)}}\right]$$
$$+\omega^2 \mu_0 \epsilon_0 H_{y(i,j)} = 0. \quad (2.97)$$

To avoid the reflection at the interface between actual region and PML, we have to match impedances on both sides, i.e.

$$Z_{actual} = \sqrt{\frac{\mu_0}{\epsilon_0 \epsilon_r}} = \sqrt{\frac{\mu_0(1 + \sigma^*/j\omega\mu_0)}{\epsilon_0(\epsilon_r + \sigma/j\omega\epsilon_0)}} = Z_{PML}, \quad (2.98)$$

which means

$$\frac{\sigma^*}{\mu_0} = \frac{\sigma}{\epsilon_0 \epsilon_r}. \quad (2.99)$$

Consider the configuration as in Fig. 2.7. In this case, PMLs are only added at upper and lower boundaries, i.e. they are only used to absorb the outgoing waves propagating in z-direction. Therefore, σ_x terms do not exist ($\mu_{xc} = 1$ and $\epsilon_{xc} = 1$), and (2.97) will be simpler.

To determine the coefficient σ_z, PMLs are cut into L layers, and σ_z grows larger as being farther from the actual region. Assume the form of σ_z is

$$\sigma_z(z) \equiv \sigma_{max}\left(\frac{z}{L \cdot \Delta z}\right)^M, \quad (2.100)$$

where z is the distance from a point in PML to the interface between actual region and PML, and M is the power of the function σ_z. To find σ_{max}, use

$\mu_c = 1 + \frac{\sigma^*}{j\omega\mu_0}$, $\epsilon_c = \epsilon_r + \frac{\sigma}{j\omega\epsilon_0}$ and impedance matching relation, i.e. (2.99), to consider

$$e^{-jk_z z} = e^{-j\omega\sqrt{\mu_0\mu_c\epsilon_0\epsilon_c}\cos\theta z} = e^{-j\omega\sqrt{\mu_0\epsilon_0\epsilon_r}\cos\theta\left(1+\frac{\sigma(z)}{j\omega\epsilon_0\epsilon_r}\right)z}$$
$$= e^{-j\omega\sqrt{\mu_0\epsilon_0\epsilon_r}\cos\theta z} \times e^{-\sqrt{\frac{\mu_0}{\epsilon_0\epsilon_r}}\cos\theta\sigma(z)z}, \qquad (2.101)$$

where θ is the angle between the incident wave and the normal of the interface, and the term at left of the last part is the loss term. Therefore, the reflection R we give at the interface after propagating a round trip of PML will be

$$R = e^{-2\cos\theta\sqrt{\frac{\mu_0}{\epsilon_0\epsilon_r}}\int_0^{L\cdot\Delta z}\sigma(z)dz}. \qquad (2.102)$$

After substituting (2.100) into (2.102) and integrating it, we obtain

$$\sigma_{max} = -\frac{(M+1)\ln R}{2L\Delta z\cos\theta}\sqrt{\frac{\epsilon_0\epsilon_r}{\mu_0}}, \qquad (2.103)$$

which combines with (2.100) and is applied to (2.97) for defining ϵ_c and μ_c.

C. Perfectly Matched Layer : Multi-Stretched-Coordinate

Here we introduce another point of view about PML. We let the loss term be a constant in each layer and match boundary at each interface, as Fig. 2.12. To derive the boundary condition for arbitrary higher order, assume that the PML only acts on the wave propagating along z direction. Consider a wave propagating toward PML but whose direction is not necessarily normal to PML, i.e.

$$\psi_y(x,z) = C(x)e^{-jk_z z}, \qquad (2.104)$$

where $C(x)$ is the part depending on x.

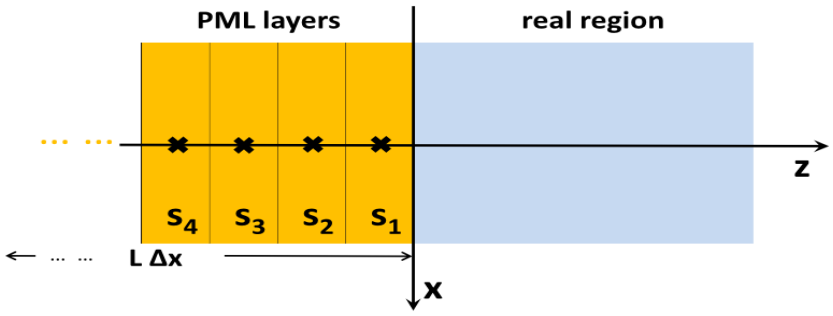

Figure 2.12: Configuration of multi-stretched-coordinate in PML.

In PML, loss terms will be put into permeability μ and permittivity ϵ as (2.87)-(2.90). By taking the impendence matching into account (like what we did in (2.101)), i.e.

$$\psi_y = C(x)e^{-jk_z z} = C(x)e^{-jk_z\left(1+\frac{\sigma(z)}{j\omega\epsilon_0\epsilon_r}\right)z} = C(x)e^{-jk_z sz}, \tag{2.105}$$

where $s \equiv 1 + \frac{\sigma(z)}{j\omega\epsilon_0\epsilon_r} = 1 + \frac{\sigma(z)^*}{j\omega\mu_0}$. From the continuity of the tangential fields, we have

$$\psi_{yR} = \psi_{yL} \tag{2.106}$$

for $0th$ order. After differentiating (2.106) by z, we obtain

$$\frac{\partial\psi_{yR}}{\partial z} = -jk_z s_R\psi_{yR} \quad \text{and} \quad \frac{\partial\psi_{yL}}{\partial z} = -jk_z s_L\psi_{yL}, \tag{2.107}$$

and combine (2.107) with (2.106) to get

$$\frac{1}{s_R}\frac{\partial\psi_{yR}}{\partial z} = \frac{1}{s_L}\frac{\partial\psi_{yL}}{\partial z}. \tag{2.108}$$

After repetition of differentiation, we will know the continuity of arbitrary high order is

$$\frac{1}{s_R^n}\frac{\partial^n \psi_{yR}}{\partial z^n} = \frac{1}{s_L^n}\frac{\partial^n \psi_{yL}}{\partial z^n}. \tag{2.109}$$

Therefore, we could use higher-order finite-difference formulation along z direction in PML to obtain better absorption.

2.3.3 Incident Wave Source Conditions

After discretizing the fields inside the calculated region and considering periodic boundary conditions and perfect matched layer, it needs to generate the sources to interact with the structure of interest. In finite-difference time-domain (FDTD) method, there are many methods to be used. For examples, hard-source **E** and **H** fields, which are set up simply by assigning a desired time function to specific components of **E** or **H** in the space lattice. Another method is J and M current sources, which can deposit charge and generate charge-associated fields.

Here the total-field/scattered-field (TF/SF) formulation [29] will be used to realize a plane-wave source. It assumes that the physical total electric and magnetic fields $\mathbf{E_{total}}$ and $\mathbf{H_{total}}$ can be decomposed as

$$\mathbf{E_{total}} = \mathbf{E_{inc}} + \mathbf{E_{scat}} \qquad \mathbf{H_{total}} = \mathbf{H_{inc}} + \mathbf{H_{scat}}, \tag{2.110}$$

where $\mathbf{E_{inc}}$ and $\mathbf{H_{inc}}$ are the incident fields, assumed to be known at all points of the space lattice. $\mathbf{E_{scat}}$ and $\mathbf{H_{scat}}$ are the scattered fields, which

are initially unknown.

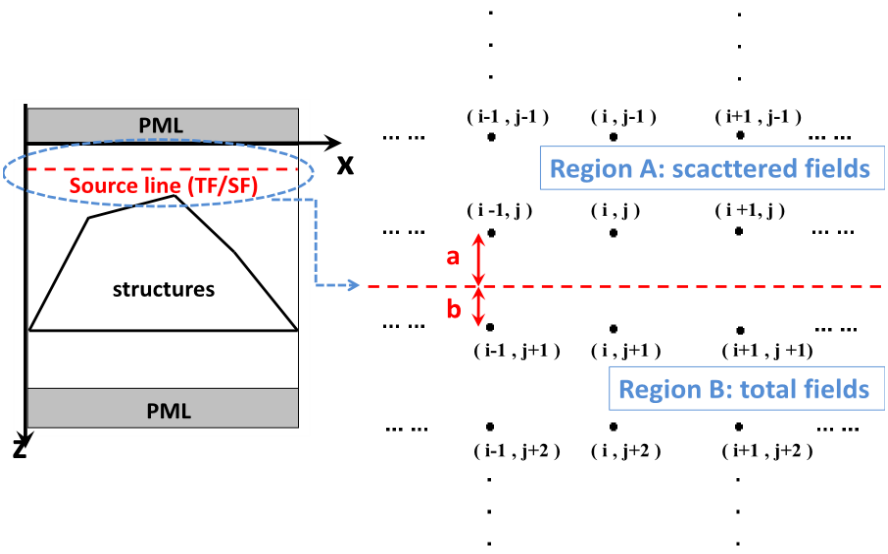

Figure 2.13: Total-field and scattered-field regions connected by a plane wave source.

Assume the electromagnetic wave propagates along $+z$ direction. The calculated region is separated into two parts, one is region A, which only includes scattered-field components; the other one is region B, which contain both scattered-field and incident-field, i.e. total fields, as shown in Fig. 2.13. After discretization, we could obtain the approximated wave equation like the form of (2.71). For simplicity, as dealing with field $\psi_{y(i,j)}$ at mesh point $x = x_i$ and $z = z_j$, express this form by

$$C_1\psi_{y(i,j-1)} + C_2\psi_{y(i-1,j)} + C_3\psi_{y(i,j)} + C_4\psi_{y(i+1,j)} + C_5\psi_{y(i,j+1)} = 0, \quad (2.111)$$

where C_1 to C_5 mean the coefficient of each mesh points after discretizing. If

all of these points are in region A, it only needs to consider scattered fields, (2.111) can be written as

$$C_1\psi^{scat}_{y(i,j-1)} + C_2\psi^{scat}_{y(i-1,j)} + C_3\psi^{scat}_{y(i,j)} + C_4\psi^{scat}_{y(i+1,j)} + C_5\psi^{scat}_{y(i,j+1)} = 0. \quad (2.112)$$

Similarly, if all of these points are in region B, only total fields are considered, (2.111) can be written as

$$C_1\psi^{total}_{y(i,j-1)} + C_2\psi^{total}_{y(i-1,j)} + C_3\psi^{total}_{y(i,j)} + C_4\psi^{total}_{y(i+1,j)} + C_5\psi^{total}_{y(i,j+1)} = 0. \quad (2.113)$$

Now, consider the configuration of Fig. 2.13, analyze the field $\psi_{y(i,j)}$, and obtain

$$C_1\psi^{scat}_{y(i,j-1)} + C_2\psi^{scat}_{y(i-1,j)} + C_3\psi^{scat}_{y(i,j)} + C_4\psi^{scat}_{y(i+1,j)} + C_5\psi^{total}_{y(i,j+1)} = 0. \quad (2.114)$$

Note that (2.114) is not consistent and correct, since it adds the unlike term $\psi^{total}_{y(i,j+1)}$ on the last part. For consistency, we must change this term by subtracting the assumed-known incident wave $\psi^{inc}_{y(i,j+1)}$, which means

$$C_1\psi^{scat}_{y(i,j-1)} + C_2\psi^{scat}_{y(i-1,j)} + C_3\psi^{scat}_{y(i,j)} + C_4\psi^{scat}_{y(i+1,j)} + C_5(\psi^{total}_{y(i,j+1)} - \psi^{inc}_{y(i,j+1)}) = 0, \quad (2.115)$$

where $\psi^{inc}_{y(i,j+1)} = exp(-jk_x x_i)exp(-jk_z(b))$ for the assumption of plane wave incidence. Then we move the term $\psi^{inc}_{y(i,j+1)}$ to right side and obtain

$$C_1\psi^{scat}_{y(i,j-1)} + C_2\psi^{scat}_{y(i-1,j)} + C_3\psi^{scat}_{y(i,j)} + C_4\psi^{scat}_{y(i+1,j)} + C_5\psi^{total}_{y(i,j+1)} = C_5\psi^{inc}_{y(i,j+1)}. \quad (2.116)$$

The similar way could be used for every points adjacent to the source line. And we could construct the sparse matrix $\mathbf{M}$ for every field points with a vector describing source terms $\mathbf{S}$, which means $\mathbf{M\Psi} = \mathbf{S}$. Finally, the field distribution could be found.

2.3.4 Calculating Diffraction Efficiencies

After finding the distribution of the field, i.e. the value of field at each points, we could use the definition (2.27) and (2.28) to find diffraction efficiency, and all we have to calculate first is R_i and T_i.

To find these terms, first we need to know a row of field distribution (in reflection region) without grating structure, and define this distribution as incidence. Next, put the grating structure into calculation, take the same row of field distribution and subtract the field distribution found in first step. Then we will obtain reflection field $\psi_R(x)$ distributing in x direction and at a position of z. Also, we take a row of field in transmittance region to be transmittance field $\psi_T(x)$. Finally, use Fourier expansion

$$\psi_R(x) = \sum_i R_i e^{-jk_{xi}x} e^{jk_{zi}^R z_R} \equiv \sum_i R_i^* e^{-jk_{xi}x}, \tag{2.117}$$

where z_R is the fixed z coordinate we take and $R_i^* = R_i e^{jk_{zi}^R z_R}$, to find Fourier coefficients

$$R_i^* = \frac{1}{\Lambda}\int_0^\Lambda \psi_R(x) e^{-jk_{xi}x} dx \approx \frac{1}{\Lambda}\sum_p e^{-jk_{xi}x_p}\psi_R(x_p)\Delta x, \tag{2.118}$$

and obtain $R_i = R_i^* e^{-jk_{zi}^R z_R}$. Using definition (2.27) to find the incident, reflective and transmitted power along direction z, then the diffraction efficiency of each order will be found.

Chapter 3

Numerical Results and Discussions

3.1 Numerical Verification of FDMM

Here the method of finite difference modal method (FDMM) with interface conditions and multi-layer approximation will be tested and verified by comparing the results with some papers. It will be applied to simulate variation of diffraction efficiencies with changes of incident angle and thickness of grating layer and verify that the usability of FDMM. For completeness, the lines with colors of light blue, pink, dark blue and green lines or shapes of circle, cross, diamond and triangle are calculated from three-, five-, seven-, and nine-point formulation of FDMM and their generalized Douglas (GD) scheme. Also, results of RCWA will be considered.

3.1.1 Incident Angle Variation

First, we compare our results with the Fig.8 in the paper of Sheng *et al.* [30]. Consider the geometry depicted in Fig. 2.2 with the following parameters: $f = 0.34$, $\Lambda = 1000nm$, $\lambda = 647.1nm$, $t_g = 60nm$, $\varepsilon_{r,inc} = \varepsilon_{r,g2} = 1$, $\varepsilon_{r,tra} = \varepsilon_{r,g1} = -17.42 - 0.58i$.

In Fig. 3.1 which is the result of the paper, the calculated method they used could be categorized into modal method. And Fig. 3.2 presents the results of RCWA and FDMM. It could be seen that these methods are agreed with each other and experimental results. The dips of zeroth-order reflectivity in Fig. 3.1 and Fig. 3.1 correspond to the excitation of surface plasmon at the matching condition

$$k_0 c = \omega(k_0 \sin\theta \pm n\frac{2\pi}{\Lambda}), \tag{3.1}$$

where c is the light speed, θ is the incident angle and $\omega(k)$ is the surface-plasmon dispersion relation. The reflectivity minima at $\theta = 14°, 25°$ and $60°$ correspond to $n = -1, 1$ and 2 respectively. At these dips, surface plasma are induced and cause very large fields at interface. And these fields will increase the loss in the lossy metal. This phenomenon could be seen by the fields diagram of Fig. 3.3 and Fig. 3.4. In Fig. 3.3, the surface plasma are not excited. However, in Fig. 3.4, the surface plasma appear as function of sine and cosine and cause larger field intensity around grating layer than Fig. 3.3. In each figure, the results on the left side mean using RCWA to solve,

and on the left side mean using RCWA.

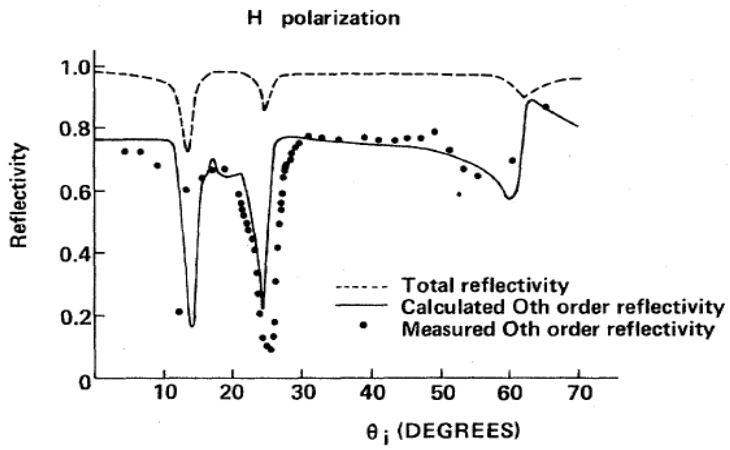

Figure 3.1: Fig.8 in the paper of Sheng *et al.* [30]. The zeroth-order reflection with respect to the incident angle.

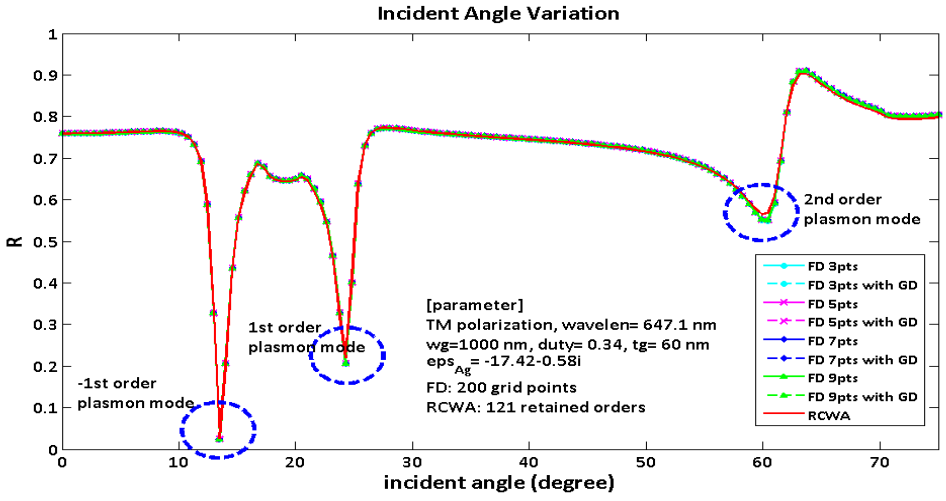

Figure 3.2: Incident angle dependence of the zeroth-order reflection for lossy metal with TM polarization (compared with Fig. 3.1).

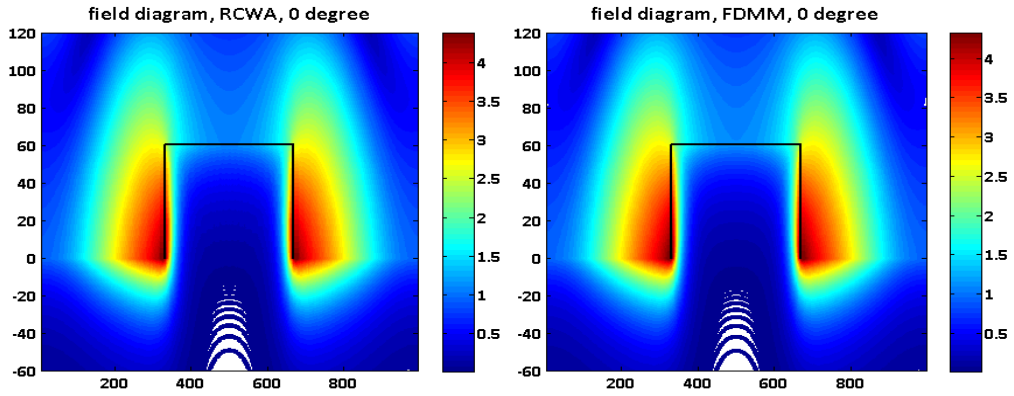

Figure 3.3: Field diagram of Fig. 3.2 at incident angle $\theta = 0°$ (Left: RCWA, Right: FDMM).

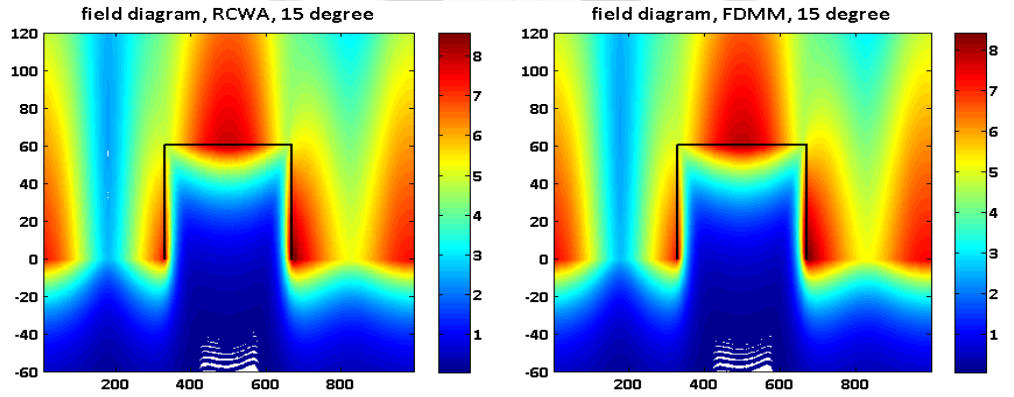

Figure 3.4: Field diagram of Fig. 3.2 at incident angle $\theta = 15°$ (Left: RCWA, Right: FDMM).

Next, consider triangular profile dielectric grating with TE incidence. Here we compare our results with Pai and Awada [25], who introduced matrices for layer transmission and interface reflection and transmission to derive solution for RCWA in terms of a multiple-reflection series, as Fig. 3.5.

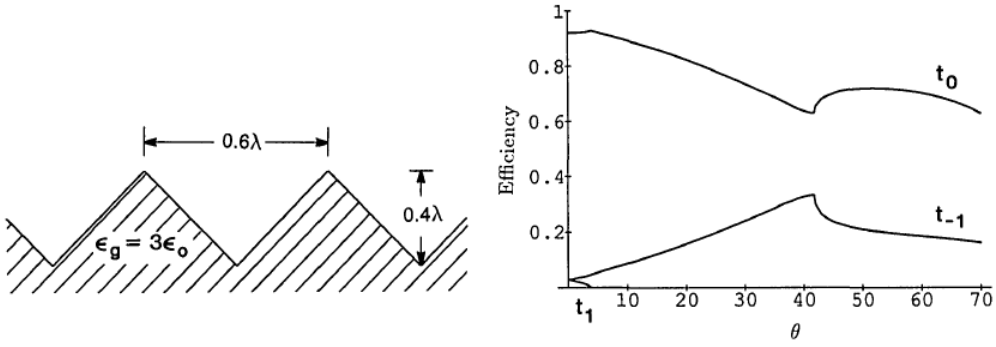

Figure 3.5: Fig.9 in the paper of Pai and Awada [25]. Transmittance with respect to the incident angle.

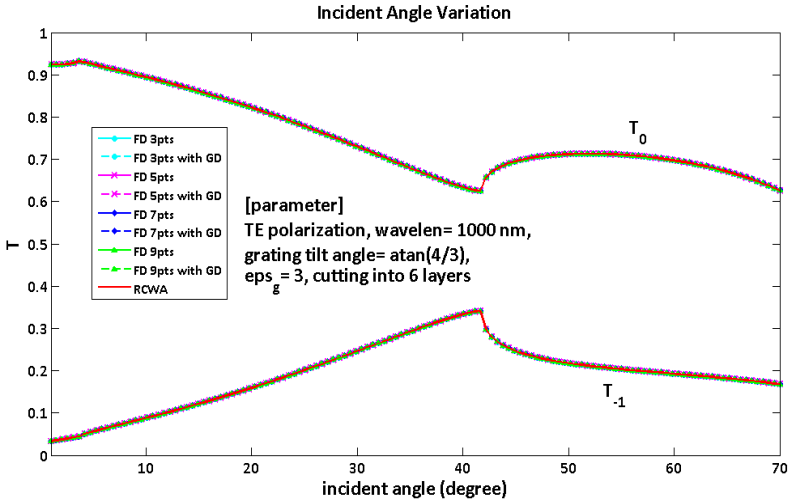

Figure 3.6: Incident angle dependence of the zeroth- and first-order transmittance for the dielectric triangular grating under TE incidence (comparing with Fig. 3.5).

And we use enhanced transmittance matrix approach proposed by Moharam *et al.* in both RCWA and FDMM, as Fig. 3.6. The parameter used

are $\lambda = 1000nm$, $\varepsilon_{r,g1} = \varepsilon_{r,tra} = 3$ and cutting into 6 layers, and the structure is like the left figure in Fig. 3.5. The results are agreeable to each other.

3.1.2 Thickness Variation

Comparing results of our methods with Fig.6 of paper of Sheng *et al.* [30]. In Fig. 3.7 and 3.8, the normally incident light is assumed to be $\lambda = 700nm$, and the gratings have the parameters $\Lambda = 1050$, $f = 0.5$, $\varepsilon_{r,Ag} = -23.4 - 0.387i$ and $\varepsilon_{r,Al} = -42.6 - 17.02i$.

It could be seen that Ag gratings acts as a nearly perfect conducting gratings with quite little absorption and Al gratings show significant absorption with increase depth. This statement could be understood more clearly by plotting absorption as a function of depth, as Fig. 3.9 and Fig. 3.10. In addition, there are some instabilities which could be found in Fig. 3.10 as using RCWA to simulate the grating with Ag material, and such problem of RCWA for highly conductive materials has been discovered by Popov *et al.* and discussed during these years. This phenomenon will be seen more obviously in the case of next subsection.

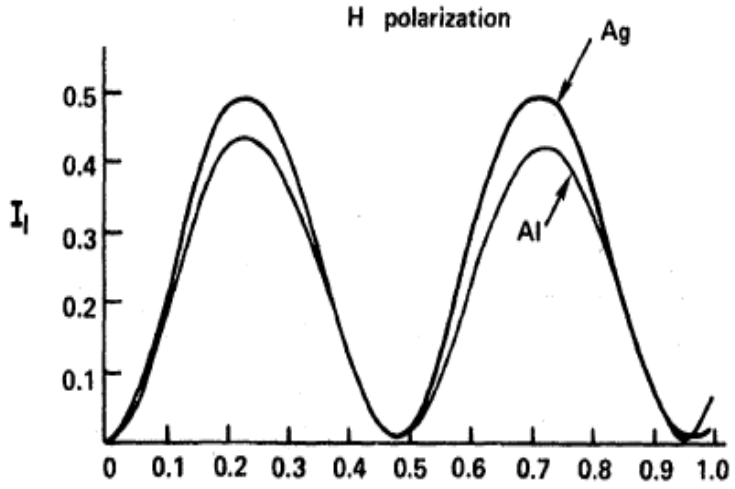

Figure 3.7: Fig.6 of paper of Sheng *et al.* [30]. The first-order reflection of Al and Ag gratings with respect to the thickness.

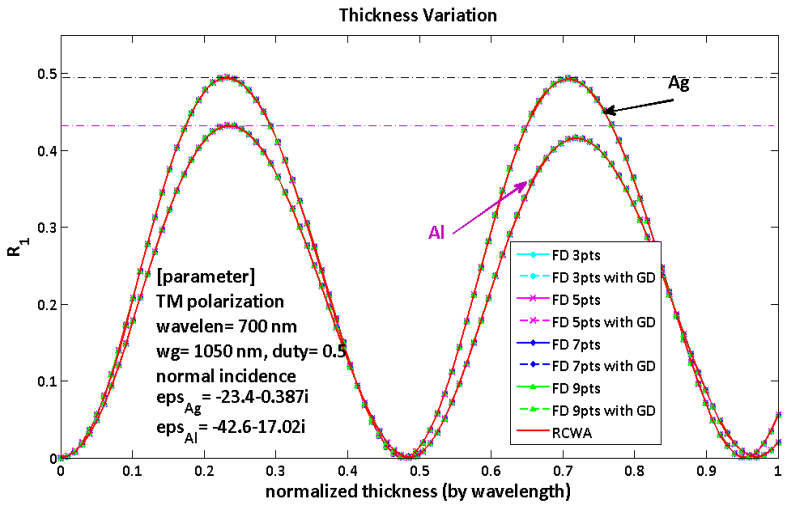

Figure 3.8: Thickness dependence of first-order reflection for Al and Ag gratings under TM incidence (compared with Fig. 3.7).

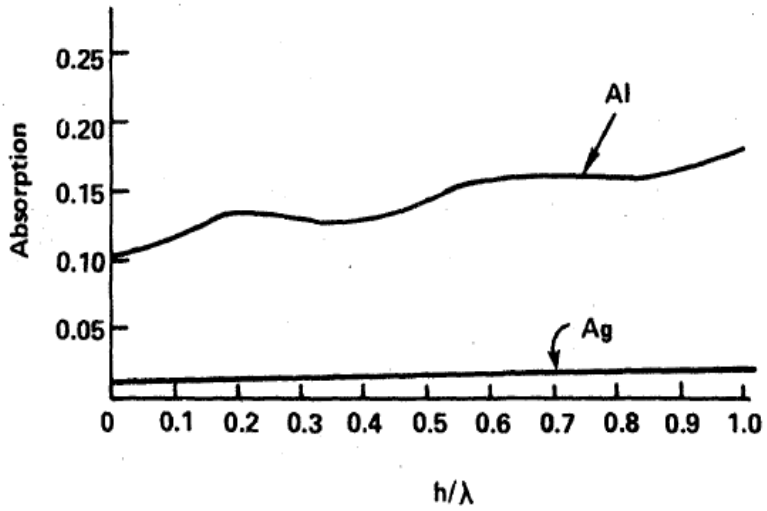

Figure 3.9: Fig.6 of paper of Sheng *et al.* [30]. The absorption of Al and Ag gratings with respect to the thickness.

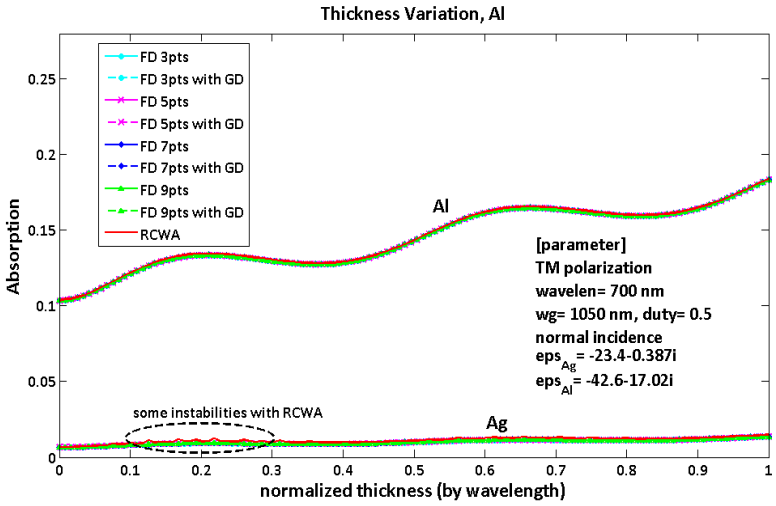

Figure 3.10: Thickness dependence of absorption of Al and Ag gratings under TM incidence (compared with Fig. 3.9).

3.1.3 Duty Cycle Variation: Removing the Instability

The RCWA is known to suffer from numerical instabilities when applied to low-loss metallic gratings under TM incidence. There were many methods proposed to deal with it, as the mention in chapter 1. Here we compare FDMM with RCWA without using mode-filtering mentioned in the paper of Lyndin *et al.* [19]. The values of the parameters are the same as Fig. 1 of [19]. The binary grating period Λ and depth t_g are $500nm$, the wavelength λ is $632.8nm$, and the incident angle θ is $30°$. The result of Lyndin's paper is shown in Fig. 3.11 , and the results of FDMM are shown in Fig. 3.12. We could see that by using appropriate method of cutting grip points, FDMM would be more stable then RCWA under certain condition.

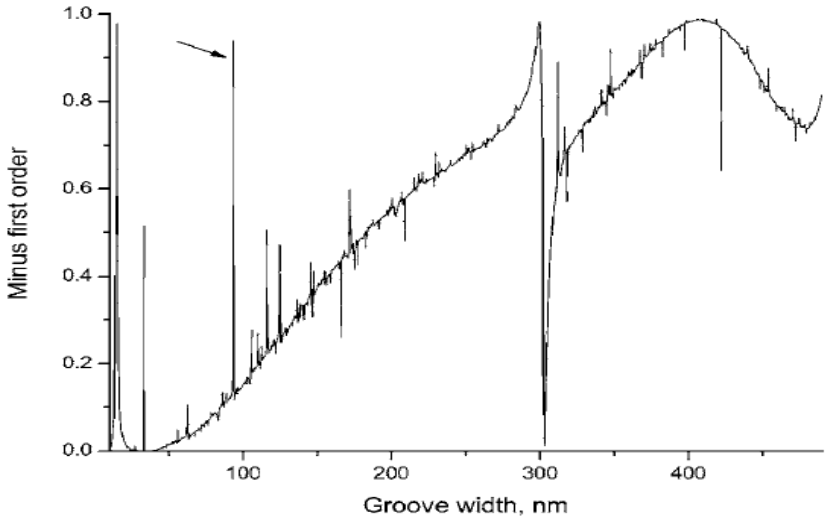

Figure 3.11: Fig.1 of paper of Lyndin *et al.* [19]. The minus-first-order reflection with respect to groove width.

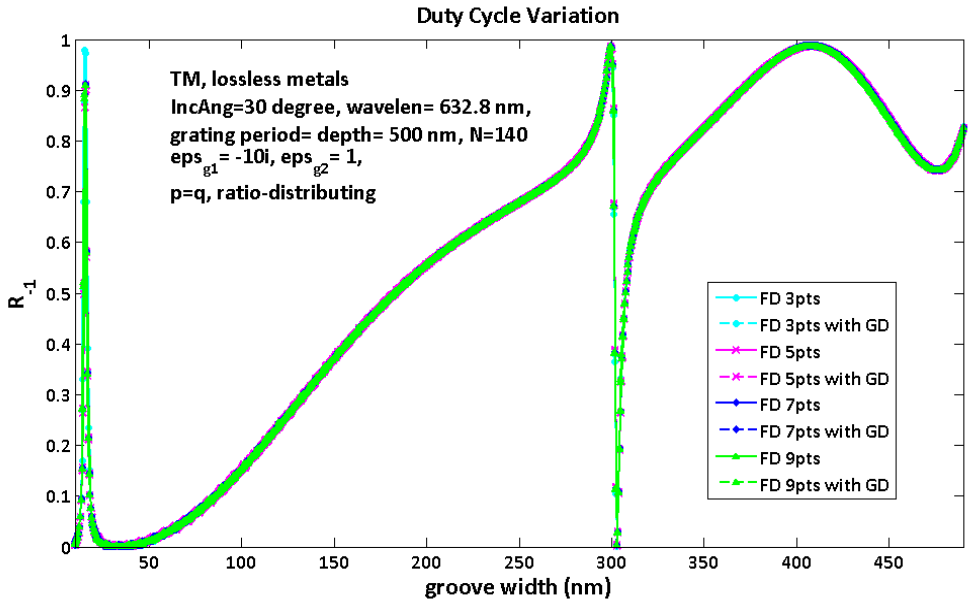

Figure 3.12: Groove width dependence of minus-first-order reflection (comparing with Fig. 3.11).

3.2 Analysis of Accuracy and Convergence

After comparing FDMM and RCWA with some paper's results and verifying the usability of FDMM proposed in this thesis, the accuracy and convergence properties of the eigenvalues and diffraction efficiencies of FDMM are going to be tested more detailedly for every kinds of materials and polarizations of planar waves in the following two sections. The reason of separating discussions into accuracy and convergence is that analytical solutions, which could be solved by modal methods, do not be used as the standard values.

The β values, which means the square of eigenvalues, are the propagation

constants of eigenmodes. The convergence of β is described by using the relative error defined as

$$\text{Relative error of } \beta \equiv \beta_{error} = \left| \frac{\beta_N - \beta_{final}}{k_0} \right|, \tag{3.2}$$

where β_N is calculated from the eigenproblem with N grids for FDMM or N retained orders for RCWA, and β_{final} is the value with the maximum N in that calculation. Besides, the error of diffraction efficiencies (DE) is described by

$$\text{Relative error of DE} = \left| DE_N - DE_{final} \right|, \tag{3.3}$$

where the suffixes of DE have the same meaning as mentioned above.

In the figures of following two sections, β_{error} of fundamental mode and DE_{error} with respect to number N will be used to compare convergence by using double-log diagrams and semi-log diagrams, and β_{error} of fundamental mode and DE_{error} with respect to number N will be used to compare accuracy. As in section 3.1, the three-, five-, seven-, and nine-point formulation of FDMM and their GD scheme are all taken into account. The light blue, pink, dark blue and green lines represent three-, five-, seven-, and nine-point formulation, respectively.

3.3 FDMM for TE polarization

3.3.1 Rectangular-Groove Gratings

A. Dielectric

A dielectric rectangular-groove grating is considered here, and its parameters are: $\varepsilon_{r,inc} = \varepsilon_{r,g2} = 1$, $\varepsilon_{r,g1} = \varepsilon_{r,tra} = 3^2$, $f = 0.45$, $\Lambda = 1000nm$, $\lambda = 1000nm$, $t_g = 1000nm$ and $\theta_{inc} = 15°$. The grid's number is taken from 20 to 380 by uniform discretization. The accuracy and convergence properties of β and the zeroth-order reflection are shown in Fig. 3.13 and Fig. 3.14.

β value of five-point FDMM without GD and even higher order FDMM are more accurate than RCWA after 30 sampled points and converge faster than RCWA. In addition, the limitation of accuracy of nine-point FDMM appears around 70 grid's number, and it is explained by round-off error which is due to finite digits of the floating points numbers in computers. The diffraction efficiency of three-point FDMM with GD becomes closer to the final solution than RCWA after 70 sampled points. The five-point with GD and more higher order FDMM could get even better convergence, but these methods will be on the same degree of accuracy after 50 sampled points.

B. Lossless metal

A lossless metallic grating is tested by using the same parameters as the case in Fig. 3.13 and Fig. 3.14 except that changing ε_{g1} and ε_{tra} into $(-10i)^2$.

The accuracy and convergence properties of β and the zeroth-order reflection are shown in Fig. 3.15 and Fig. 3.16. In these two figures, it could be found that β value of three-point FDMM with GD and even higher order FDMM are more accurate than RCWA after 40 sampled points, and the diffraction efficiency of three-point FDMM with GD becomes closer to the final solution than RCWA after 40 sampled points. Being different from the case of Fig. 3.13 and Fig. 3.14, convergence lines of DE_{error} for even higher order would separate more obviously, and nine-point FDMM without GD and even higher order one could get the best convergence.

C. Lossy metal

The lossy metallic grating is simulated by changing the parameter ε_{g1} and ε_{tra} above to $(3.18 - 4.41i)^2$. Results of this case are shown in Fig. 3.17 and Fig. 3.18. Although accuracy of β of five-point FDMM without GD and three-point FDMM with GD is worse than RCWA in this range of grid's number, accuracy of DE_{error} of them is still better than RCWA. There is no obvious relation between convergence of β_{error} and that of DE_{error}.

Generally speaking, for TE polarization and uniform discretization, three-point FDMM and even higher order FDMM could be more correct than RCWA under an equal N. By the way, being different from RCWA, whose matrices of eigenproblems is full matrices, the sparse matrices are solved in the eigenproblems for FDMM, and this might reduce the computation time.

D. Lossy metal with high conductivity

Here we consider lossy metals with very high conductivity. Lalanne and Hugonin [22] set the specific parameters to study the robustness of numerical methods. Under such condition, the convergence of RCWA is getting quite worse for both TE and TM polarization. Here the same parameters are taken into account for TE polarization by FDMM, and proper nonuniform discretization with increasing resolution around discontinuities will be adopted. The parameters used are: $\varepsilon_{inc} = \varepsilon_{g2} = 1$, $\varepsilon_{g1} = \varepsilon_{tra} = (1 - 40i)^2$, $f = 0.57$, $\Lambda = 1236.1nm$, $\lambda = 1000nm$, $t_g = 0.4\Lambda$ and $\theta_{inc} = \arcsin(\lambda/2/\Lambda)$. The grid's number is taken from 20 to 550. The results are shown in Fig. 3.19 and Fig. 3.20. In this case, even three-point FDMM without GD is better than RCWA.

Now it could be manifested that FDMM with considering boundary condition and arbitrary high order approximation would be better than RCWA in convergence and accuracy under the TE incidence with planar gratings. In the next subsection, arbitrary structure of gratings with multi-layer approximation will be tested.

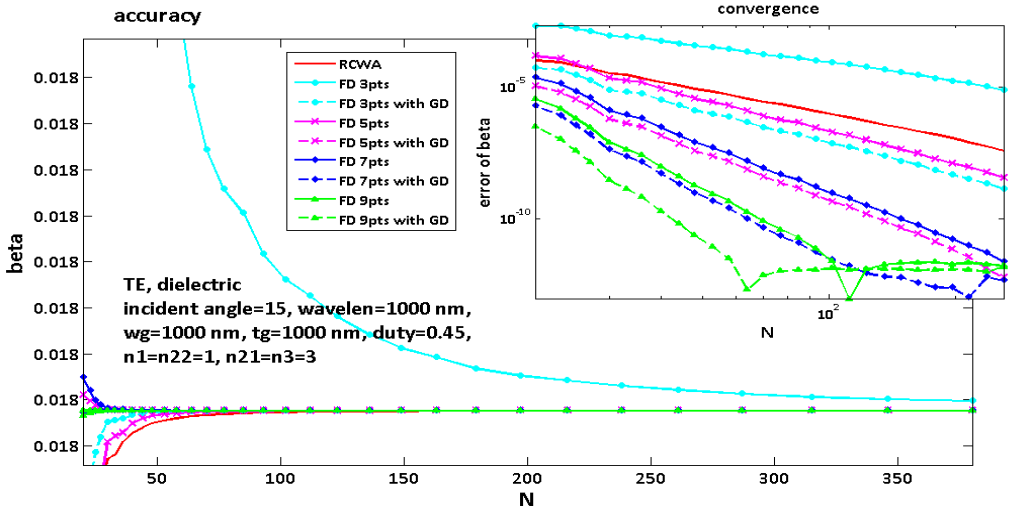

Figure 3.13: Accuracy and convergence of β of fundamental mode. A dielectric grating with $\varepsilon_{r,g1} = 3^2$ under TE incidence.

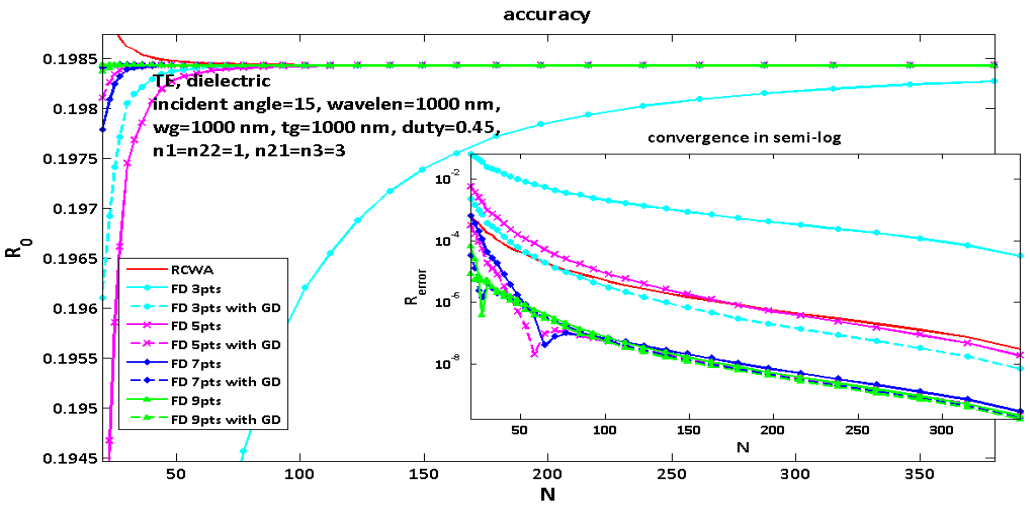

Figure 3.14: Convergence of the zeroth-order reflection. A dielectric grating with $\varepsilon_{r,g1} = 3^2$ under TE incidence.

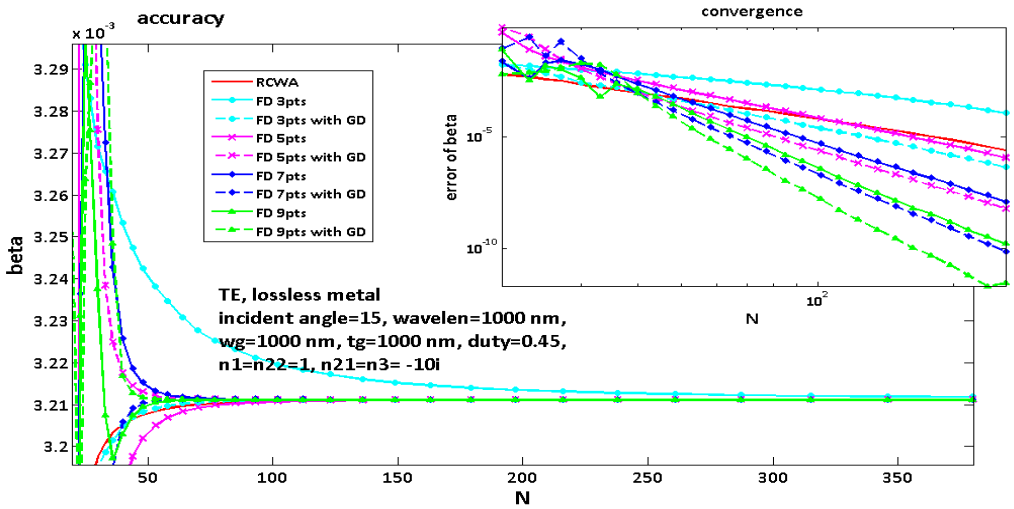

Figure 3.15: Accuracy and convergence of β of fundamental mode. A lossless metallic grating with $\varepsilon_{r,g1} = (-10i)^2$ under TE incidence.

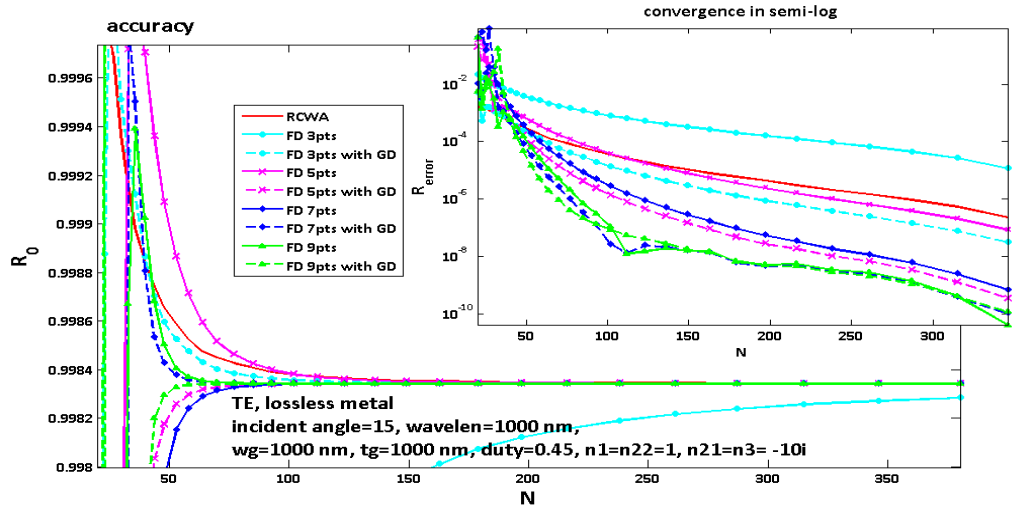

Figure 3.16: Convergence of the zeroth-order reflection. A lossless metallic grating with $\varepsilon_{r,g1} = (-10i)^2$ under TE incidence.

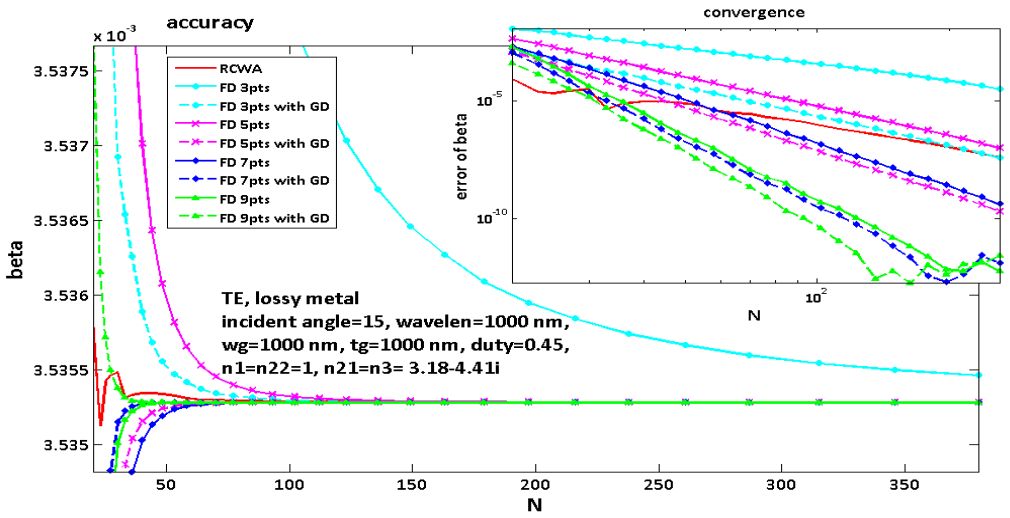

Figure 3.17: Accuracy and convergence of β of fundamental mode. A lossy grating with $\varepsilon_{r,g1} = (3.18 - 4.41i)^2$ under TE incidence.

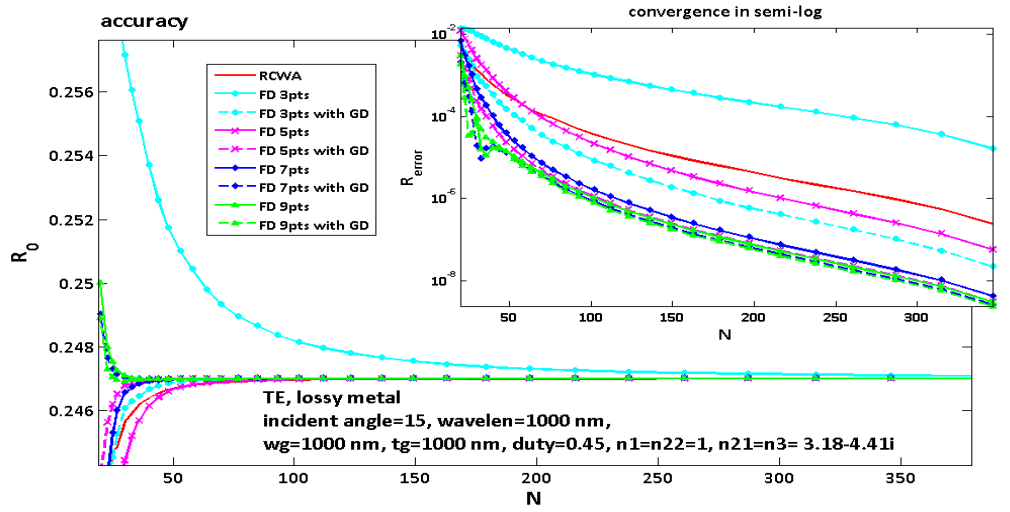

Figure 3.18: Convergence of the zeroth-order reflection. A lossy grating with $\varepsilon_{r,g1} = (3.18 - 4.41i)^2$ under TE incidence.

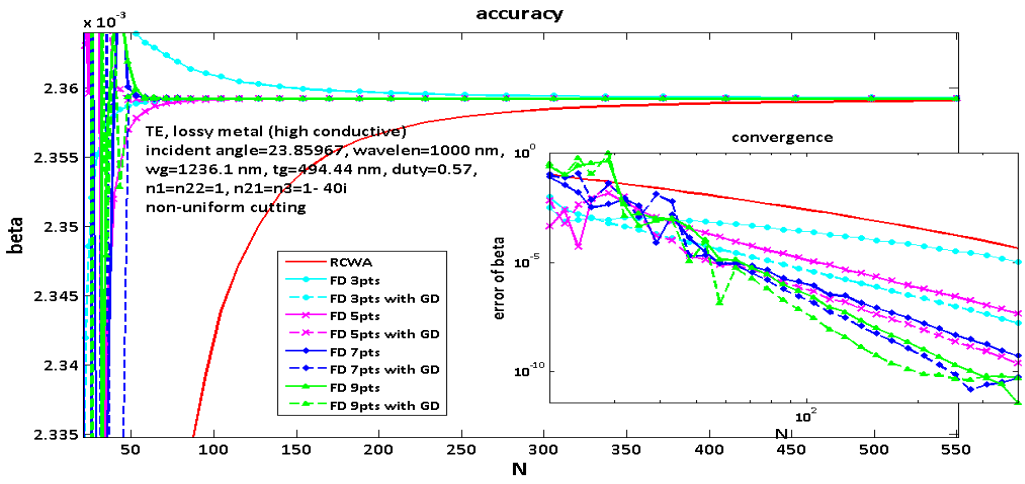

Figure 3.19: Accuracy and convergence of β of fundamental mode. A high conductive grating metallic with $\varepsilon_{r,g1} = (1 - 40i)^2$ under TE incidence and nonuniform discretization.

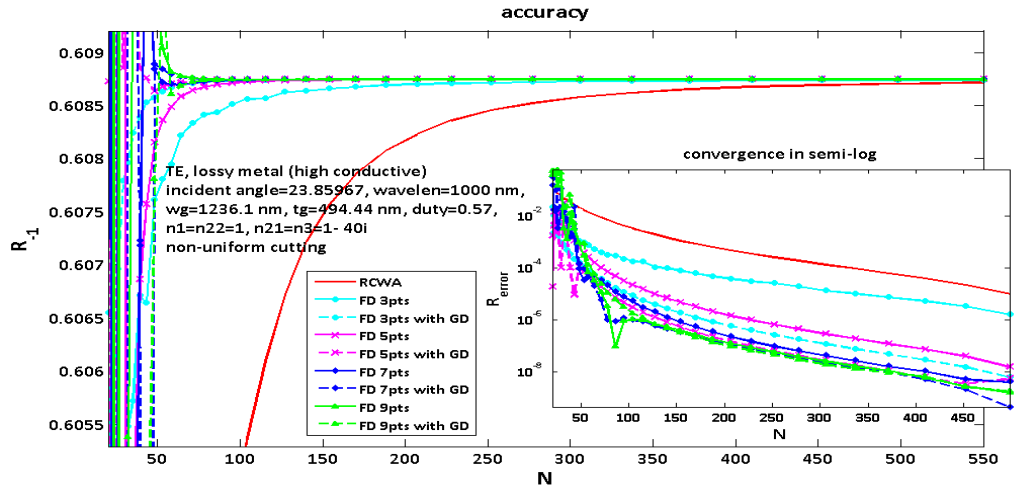

Figure 3.20: Convergence of the zeroth-order reflection. A high conductive metallic grating with $\varepsilon_{r,g1} = (1 - 40i)^2$ under TE incidence and nonuniform discretization.

3.3.2 Arbitrary Profiles Gratings

Here the gratings with triangular profile is used to comparing accuracy and convergence of FDMM with RCWA. The parameters and profile are illustrated in Fig. 3.21. In the following figures, the parameters of grating's profile are: $t_g = 1000nm$, $\Lambda = 1000nm$, $\theta_{tilt} = \arctan(2t_g/\Lambda)$, number of layers=15 and $\varepsilon_{r,inc} = \varepsilon_{r,g2} = 1$. And the results of dielectric, lossy metallic and lossless metallic gratings under both TE and TM polarization are going to be shown.

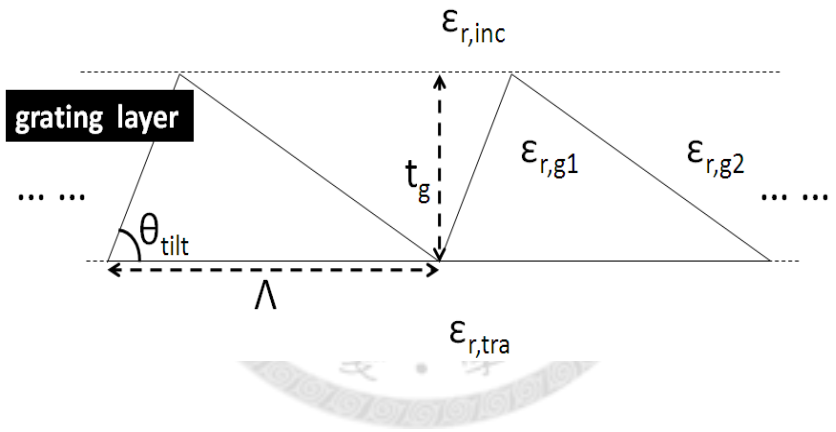

Figure 3.21: Configuration of triangular gratings.

A. Dielectric

For a dielectric grating with $\varepsilon_{r,g1} = \varepsilon_{r,tra} = 3^2$ under TE polarization, results of accuracy and convergence are shown in Fig. 3.23. It is found that three-point formulation with GD and even higher order methods converge as fast as RCWA at first, and will be closer to the final value than RCWA at

large grid's number, but the advantages of FDMM here are not obvious in this case. However, if the revised discretization method making the distances between discontinuities and their adjacent grid points on both sides of them equal is used as in Fig. 3.22, the results would become more stable, and the

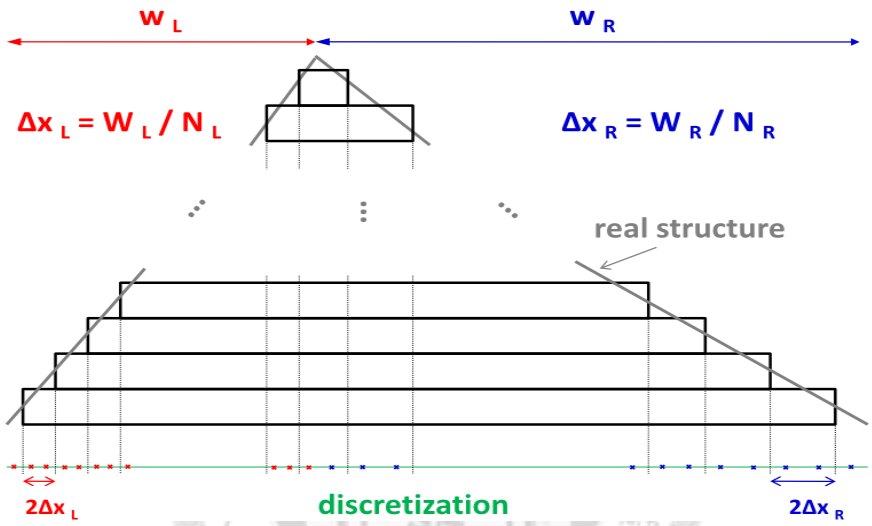

Figure 3.22: Revised discretization for multi-layer approximation.

effect of higher order methods becomes obvious, as in Fig. 3.24. This proper discretization is more important for TM polarization.

B. Lossless metal

A lossless metal grating with $\varepsilon_{r,g1} = \varepsilon_{r,tra} = (-10i)^2$ and proper discretization as in Fig. 3.22 is considered, and its results are shown in Fig. 3.25. It is found that five-point FDMM is on the same degree of accuracy of RCWA, and the convergence of three-points and even higher order formula-

tions are better than RCWA.

C. Lossy metal

A lossy metallic grating with $\varepsilon_{r,g1} = \varepsilon_{r,tra} = (3.18 - 4.41i)^2$ and proper discretization is tested, and its results are shown in Fig. 3.26. The three-point FDMM with GD and even higher order methods are superior to RCWA obviously.

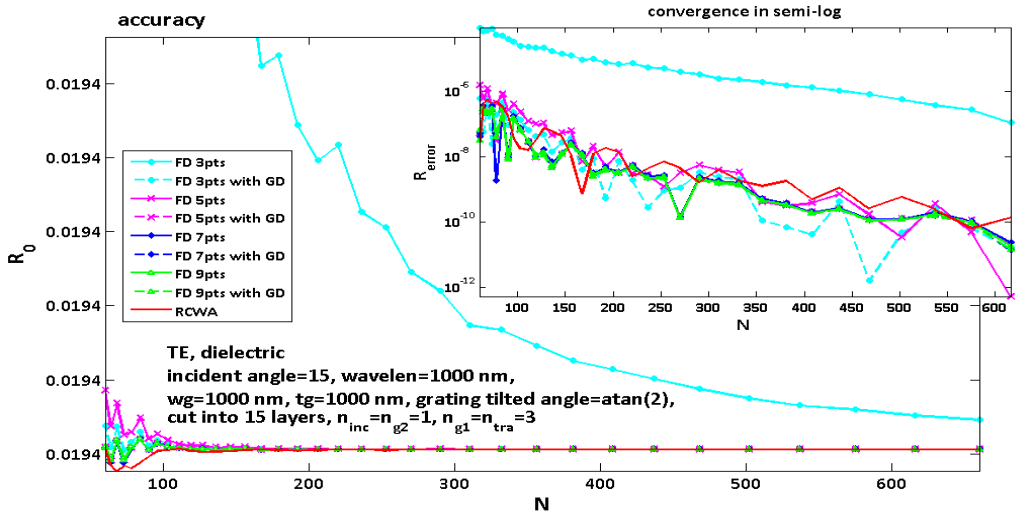

Figure 3.23: Convergence of the zeroth-order reflection. A dielectric triangular grating with $\varepsilon_{g1} = 3^2$ under TE incidence.

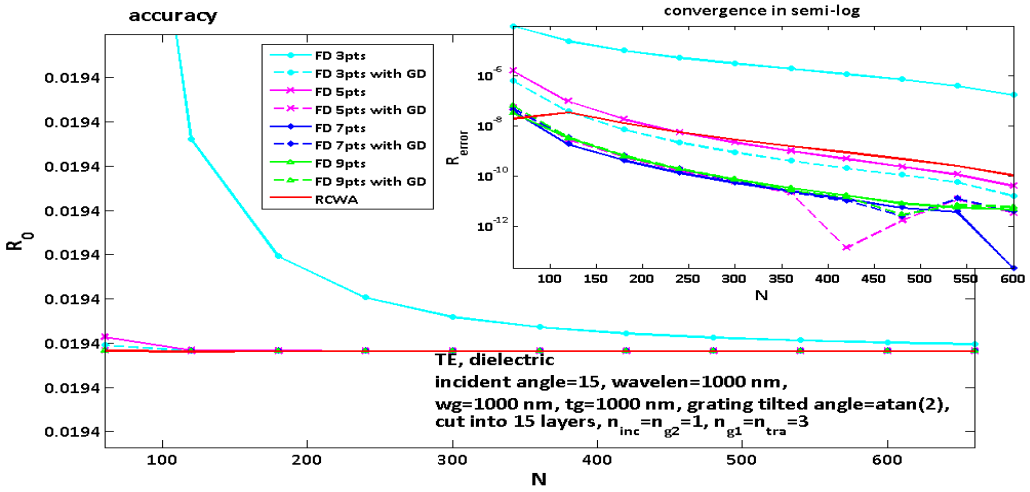

Figure 3.24: Convergence of the zeroth-order reflection with proper discretization. A dielectric triangular grating with $\varepsilon_{g1} = 3^2$ under TE incidence.

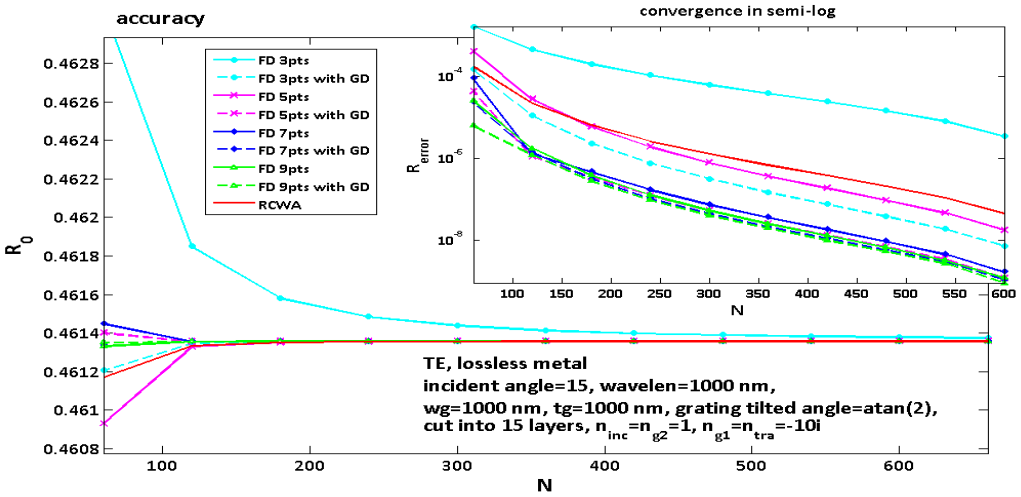

Figure 3.25: Convergence of the zeroth-order reflection with proper discretization. A lossless metal triangular grating with $\varepsilon_{g1} = (-10i)^2$ under TE incidence.

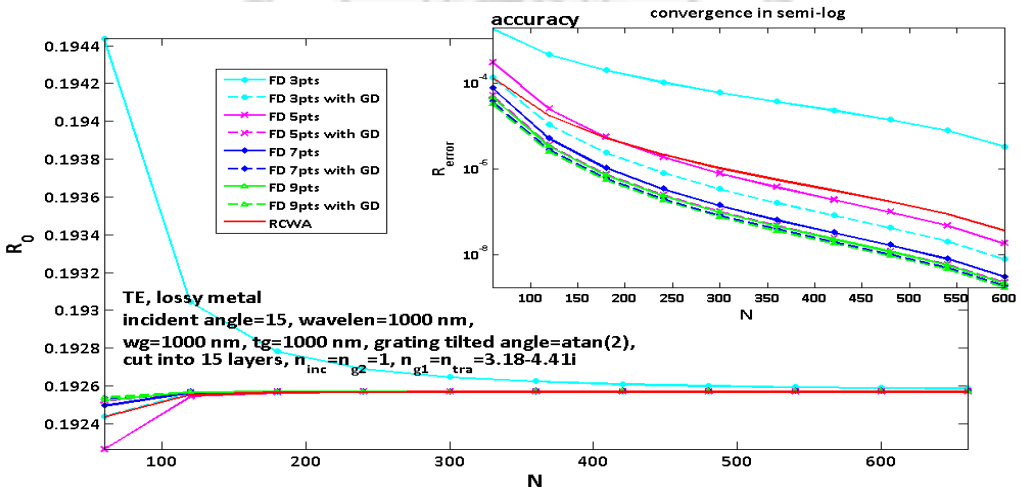

Figure 3.26: Convergence of the zeroth-order reflection with proper discretization. A lossy triangular grating with $\varepsilon_{g1} = (3.18 - 4.41i)^2$ under TE incidence.

3.4 FDMM for TM polarization

3.4.1 Rectangular-Groove Gratings

In this subsection accuracy and convergence are investigated again with the same parameters as those in preceding section except for TM polarization. Note that here the method of discretization in each layer is distributing grid points according to the ratio of width of each region inside that layer. This process could avoid too large difference of distances from sample points to discontinuities between points on each side of discontinuities and will be discussed in the last part of this subsection.

A. Dielectric

Consider a dielectric grating with $\varepsilon_{g1} = \varepsilon_{tra} = (3)^2$, and the results are shown in Fig. 3.27 and Fig. 3.28. It could be found that although the propagation constants β of five-point FDMM without GD and methods with even higher order converge faster than RCWA, the convergence of diffraction efficiencies of FDMM are slower than RCWA, and the results of every FDMM are on the same degree of accuracy except for three-point FDMM.

B. Lossless metal

A lossless grating with $\varepsilon_{g1} = \varepsilon_{tra} = (-10i)^2$ is tested, and the results is shown in Fig. 3.29 and Fig. 3.30. In this case, RCWA's results are quite unstable and do not converge to a satisfying degree of accuracy. However, such kind of situation will not happen in FDMM. Therefore, although not

all convergence lines of β of FDMM converge faster than that of RCWA, the convergence of diffraction efficiencies of FDMM is superior to RCWA even for three-point FDMM without GD.

C. Lossy metal I

A lossy metallic grating with $\varepsilon_{g1} = \varepsilon_{tra} = (3.18 - 4.41i)^2$ is considered. Like dielectric gratings with TM polarization, the diffraction efficiencies of FDMM converge slower than RCWA. The results are shown in Fig. 3.31 and Fig. 3.32.

D. Lossy metal II

If the parameter ε_{g1} of lossy gratings is replaced by highly conductive one, FDMM will become superior to RCWA. To verify this statement, consider a lossy metallic grating with $\varepsilon_{g1} = \varepsilon_{tra} = (0.22 - 6.71i)^2$ which is the permittivity of gold at $\lambda = 1000nm$, and the results are shown in Fig. 3.33 and Fig. 3.34.

E. Lossy metal with high conductivity

Finally, we test FDMM in an even higher conductive grating with $\varepsilon_{g1} = \varepsilon_{tra} = (1 - 40i)^2$. The results are shown in Fig. 3.35 and Fig. 3.36. Although the results of FDMM will be more correct than RCWA until exceeding 200 grid's number, FDMM can still be seen as a better choice than RCWA because the result of RCWA converges quite slowly in this case. Note that the FDMM inside each layer can not be taken non-uniform discretization under

TM polarization.

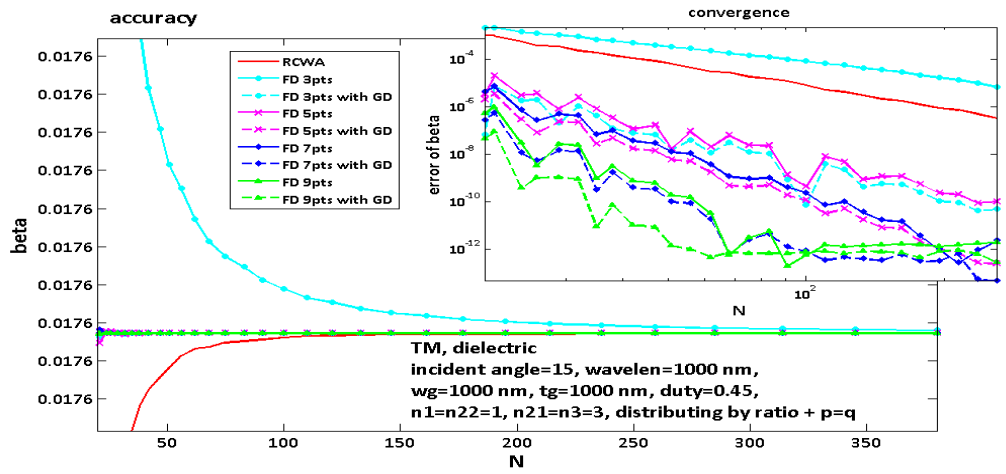

Figure 3.27: Accuracy and convergence of β of fundamental mode. A dielectric grating with $\varepsilon_{r,g1} = 3^2$ under TM incidence. Grids are distributed by ratio of width.

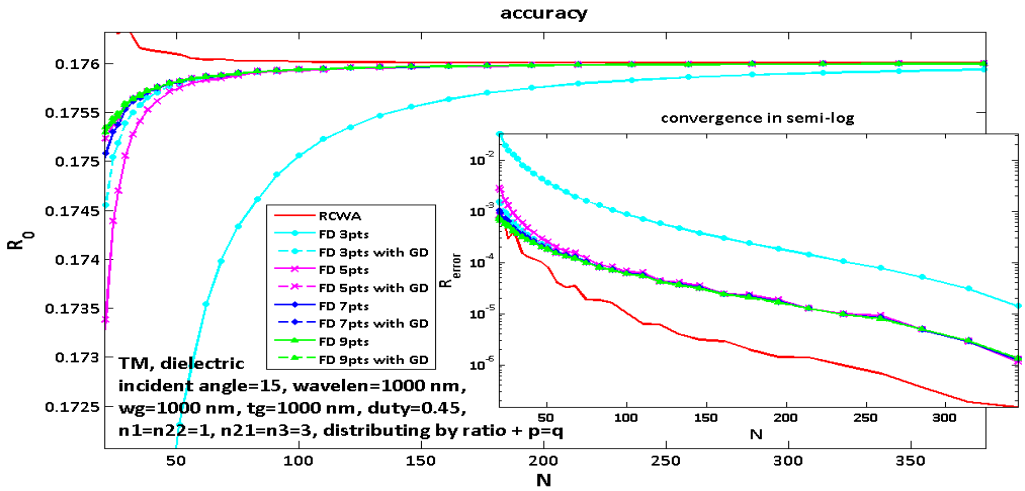

Figure 3.28: Convergence of the zeroth-order reflection. A dielectric grating with $\varepsilon_{r,g1} = 3^2$ under TM incidence. Grids are distributed by ratio of width.

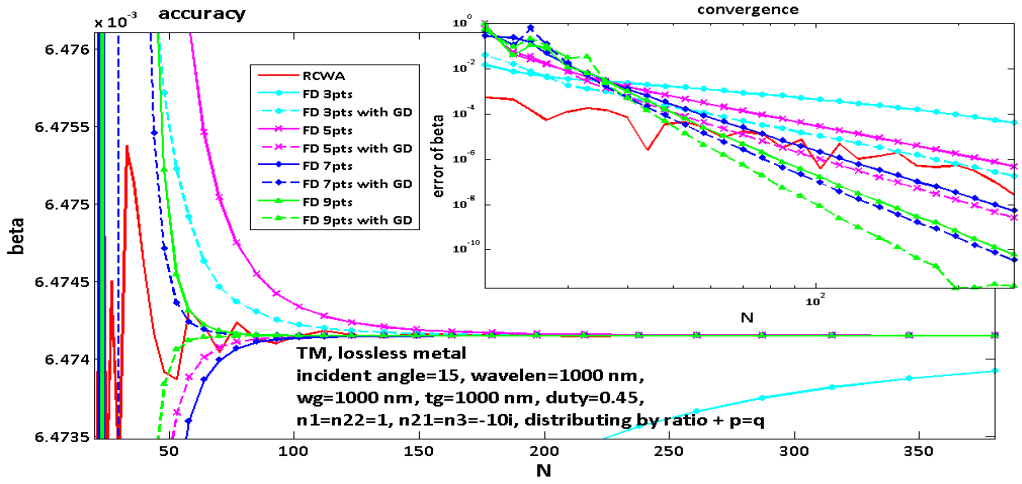

Figure 3.29: Accuracy and convergence of β of fundamental mode. A lossless metallic grating with $\varepsilon_{r,g1} = (-10i)^2$ under TM incidence. Grids are distributed by ratio of width.

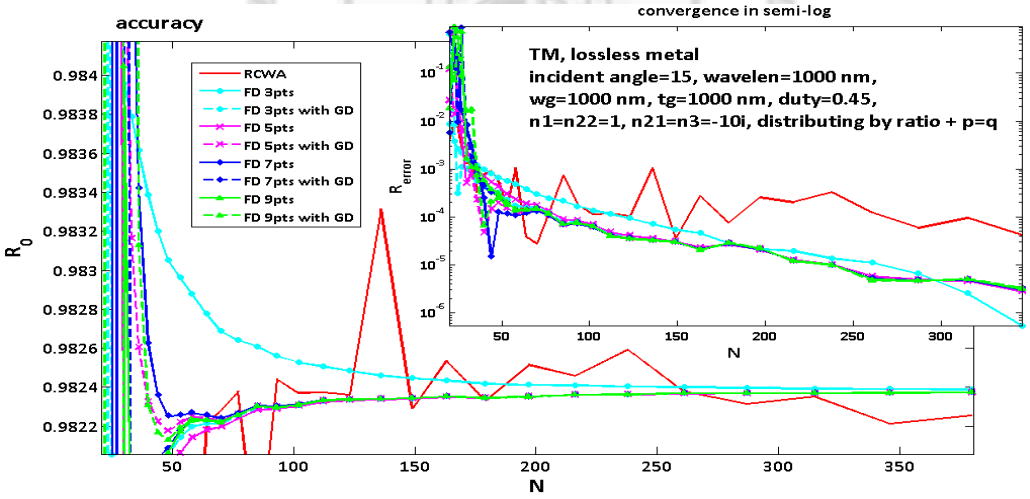

Figure 3.30: Convergence of the zeroth-order reflection. A lossless metallic grating with $\varepsilon_{r,g1} = (-10i)^2$ under TM incidence. Grids are distributed by ratio of width.

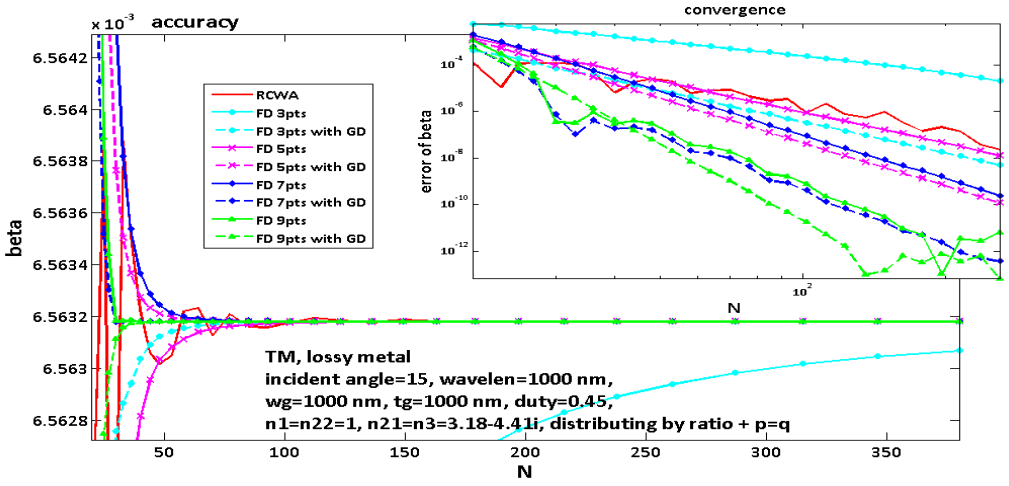

Figure 3.31: Accuracy and convergence of β of fundamental mode. A lossy grating with $\varepsilon_{r,g1} = (3.18-4.41i)^2$ under TM incidence. Grids are distributed by ratio of width.

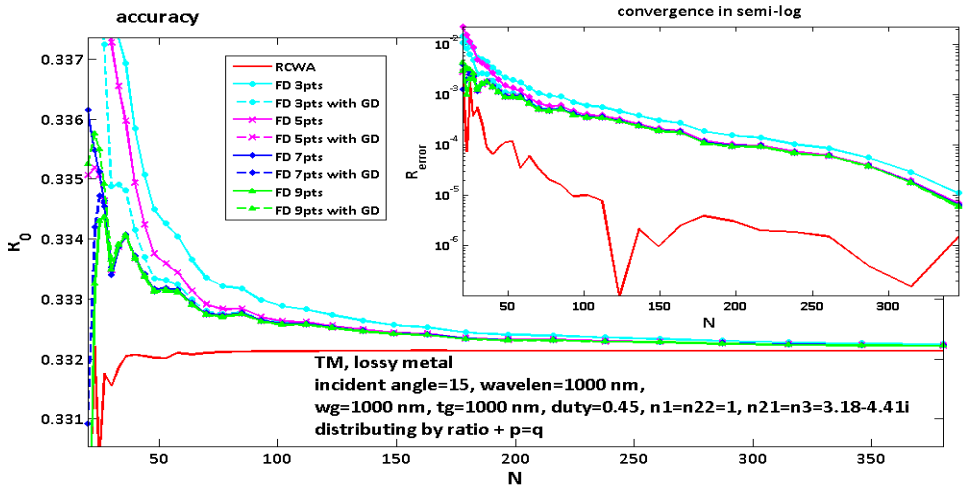

Figure 3.32: Convergence of the zeroth-order reflection. A lossy grating with $\varepsilon_{r,g1} = (3.18 - 4.41i)^2$ under TM incidence. Grids are distributed by ratio of width.

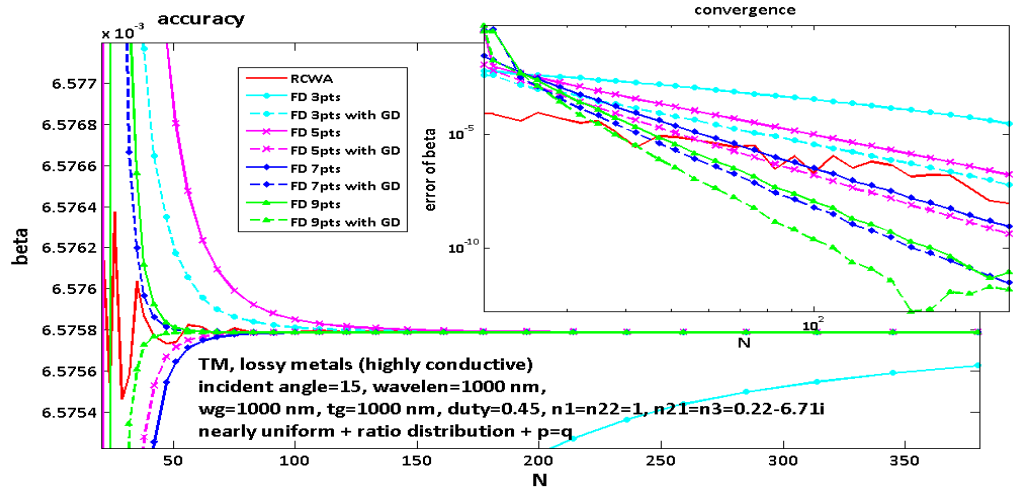

Figure 3.33: Accuracy and convergence of β of fundamental mode. A lossy grating with $\varepsilon_{g1} = (0.22 - 6.71i)^2$ under TM incidence. Grids are distributed by ratio of width.

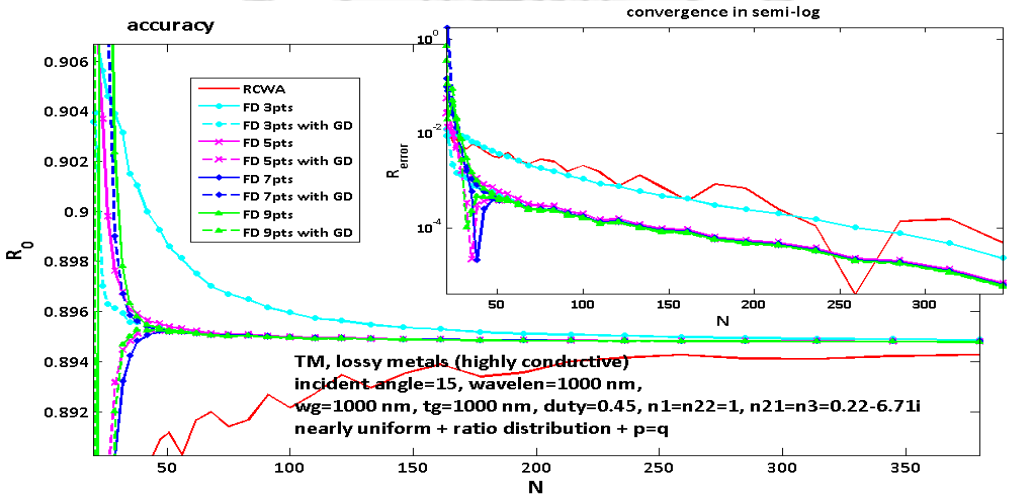

Figure 3.34: Convergence of the zeroth-order reflection. A lossy grating with $\varepsilon_{g1} = (0.22 - 6.71i)^2$ under TM incidence. Grids are distributed by ratio of width.

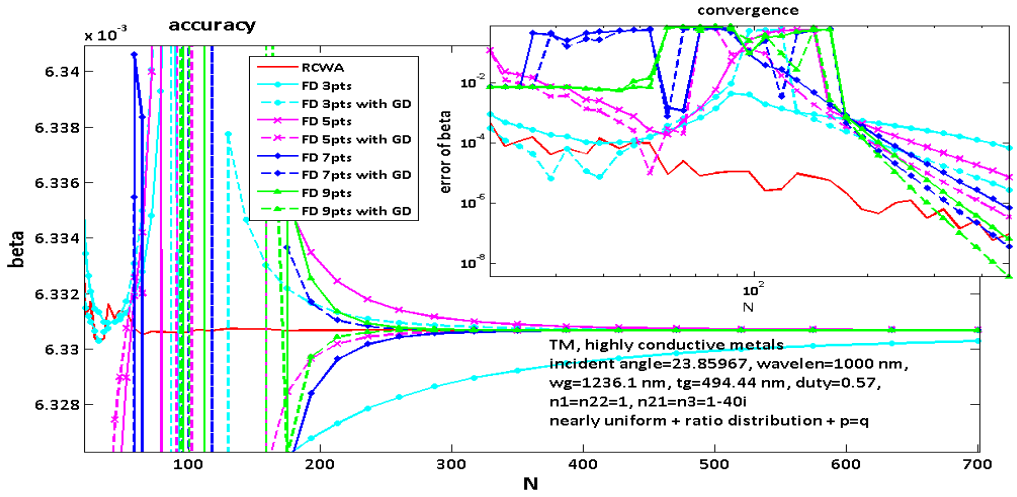

Figure 3.35: Accuracy and convergence of β of fundamental mode. A highly conductive grating with $\varepsilon_{g1} = (1 - 40i)^2$ under TM incidence. Grids are distributed by ratio of width.

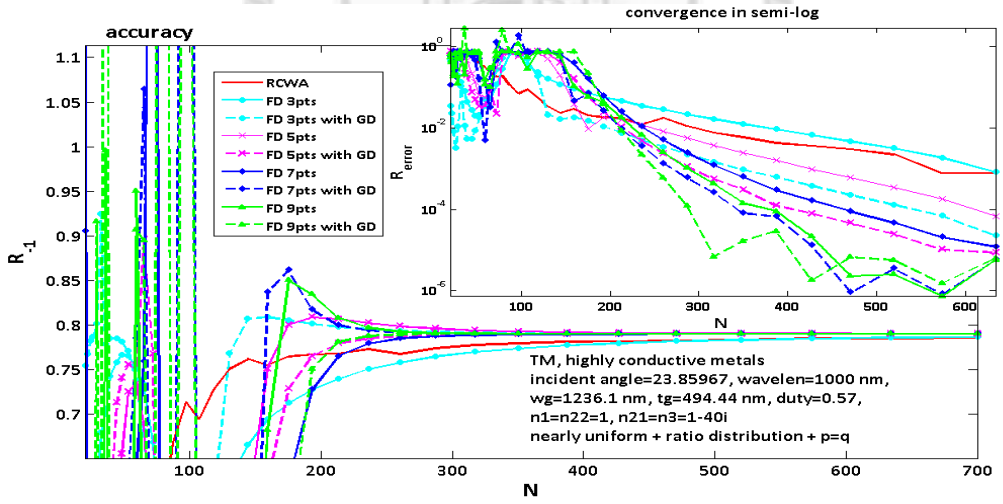

Figure 3.36: Convergence of the zeroth-order reflection. A highly conductive grating with $\varepsilon_{g1} = (1 - 40i)^2$ under TM incidence. Grids are distributed by ratio of width.

At the beginning of this subsection, we noted a proper way for TM polarization to dicretize. It is found that the ratio of distance between discontinuities and their adjacent grid points affect the convergence properties, especially for the convergence of diffraction efficiencies. This problem may be due to ignoring some boundary conditions while constructing the sparse matrix and solving eigen-problem in each layer. And this omission will cause the contradiction of continuity of fields as matching boundary condition between every layers.

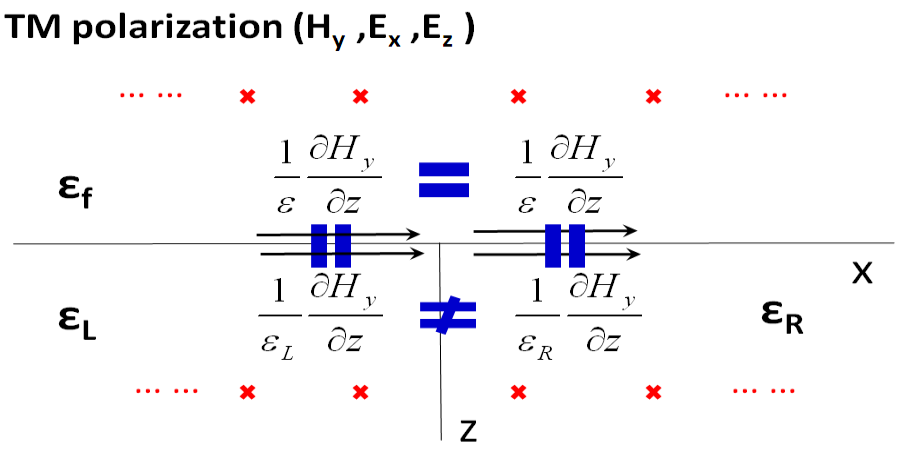

Figure 3.37: Continuity of E_x fields for TM polarization.

As in Fig. 3.37, while matching boundary of tangential field E_x for TM polarization, the fields $\frac{1}{\epsilon}\frac{\partial H_y}{\partial z}$ are continuous at the interface between the upper and the lower layer. But, inside the lower layer of Fig. 3.37, the field $\frac{1}{\epsilon_L}\frac{\partial H_y}{\partial z}$ on the left side and $\frac{1}{\epsilon_R}\frac{\partial H_y}{\partial z}$ on the right side are not continuous at the vertical

interface. Therefore, it causes the contradiction of continuity of fields $\frac{1}{\epsilon}\frac{\partial H_y}{\partial z}$ at the vertical interface in the lower layer of Fig. 3.37. In addition, while constructing the sparse matrix for TM polarization in FDMM, the boundary condition of the fields $\frac{1}{\epsilon}\frac{\partial H_y}{\partial z}$ or the boundary condition of fields E_x is not considered, and what we considered are only tangential fields H_y and E_z. This effect of contradiction does not happen in TE polarization because the fields $\frac{\partial E_y}{\partial z}$ (which means B_x) used in matching boundary condition between every layers are always continuous at the vertical interface of Fig. 3.37.

As using nonuniform discretization to increasing the spatial resolution near the interfaces for TM polarization, or distributing grid points without considering the ratio of width of each different region inside one layer, such kind of contradiction may impact the stability and the convergence more drastically. Hence, this is my speculation on the failure of FDMM under TM polarization for nonuniform discretization and the dependance on the ratio of distances between the interface and its adjacent grid points. In addition, the similar problem of continuity at corners has been discussed by Chiou *et al.* [31].

However, this problem does not happen in FMM (or RCWA) as well, even for TM polarization. It could be explained by using $\frac{1}{\epsilon_r}\frac{\partial H_y}{\partial z}$ combined with (2.7) and (2.20) to get

$$\frac{1}{\epsilon_r}\frac{\partial H_{yi}^G}{\partial z} = \sum_p \sum_m a_{ip} w_{pm} (-j\beta_m)\{g_m^+ - e^{-j\beta_m t} g_m^-\} e^{-jk_{xi}x} \tag{3.4}$$

for a specific order. The boundary conditions of fields at the interfaces are matched by use of the same Fourier order terms in FMM (or RCWA). And it could be found in (3.4) that this field of the specific order is continuous at the vertical interface of Fig. 3.37 naturally because the x-dependance of the fields is a continuous function $e^{-jk_{xi}x}$. Therefore, this is my speculation on why RCWA does not have such contradictory problem. Although RCWA does not suffer from the problem of contradiction of field's continuity as matching boundary condition between every adjacent layers, it has difficulty in effectively describing structures with abrupt and large change in permittivity by Fourier bases because such bases are continuous functions.

In a word, the difficulty of FMM (or RCWA) is inside one layer to describe the abrupt change material by continuous functions, and the problem of FDMM is contradiction of continuity of fields as matching boundary condition around corners.

3.4.2 Arbitrary Profiles Gratings

A. Dielectric

From preceding subsection, it has been known that one needs to use proper discretization to avoid the instabilities for TM polarization. However, as the gratings cut into many layer for approximating arbitrary shape of gratings, such proper discretization for every interfaces would be achieved more difficultly. But if the proper discretization is not considered, the serious problem of instability will occur, as in Fig. 3.38, which shows transmittance for TM case with respect to the grid's number for uniform grids. The parameters of the grating's structure are: $t_g = 1000nm$, $\Lambda = 1000nm$, $\theta_{tilt} = \arctan(2t_g/\Lambda)$, number of layers=15 $\varepsilon_{r,tra} = \varepsilon_{r,g1} = 3^2$ and $\varepsilon_{r,inc} = \varepsilon_{r,g2} = 1$. The results of FDMM in Fig. 3.38 are inferior to that of RCWA and suffer from obvious instabilities. And these instabilities could be avoided by placing grid points as in Fig. 3.22. After using such proper discretization, the results will become quite stable, as in Fig. 3.39.

Although convergence of FDMM is a little worse than that of RCWA in Fig. 3.39, the results of FDMM is correct and stable. Therefore, it could be expected that results of FDMM become better than RCWA as simulating structures that RCWA will suffer from instabilities or slower convergence.

B. Lossless metal

A lossless metal grating with $\varepsilon_{r,g1} = \varepsilon_{r,tra} = (-10i)^2$ is considered, and its

results are shown in Fig. 3.40. In this case, results of RCWA are very unstable and incorrect. However, the results of FDMM with proper discretization could avoid such instability and failure. Notice that three-point FDMM without GD is superior to other higher order FDMM unexpectedly.

C. Lossy metal

Finally, a lossy metal grating with $\varepsilon_{r,g1} = \varepsilon_{r,tra} = (3.18 - 4.41i)^2$ is tested. Fig. 3.41 shows that the results of FDMM converge faster than that of RCWA even for three-point formulation without GD. Note that this is different from the result of FDMM for rectangular-groove grating with the same $\varepsilon_{r,g1}$ and $\varepsilon_{r,tra}$, which shows that all of the formulations of FDMM are inferior to RCWA.

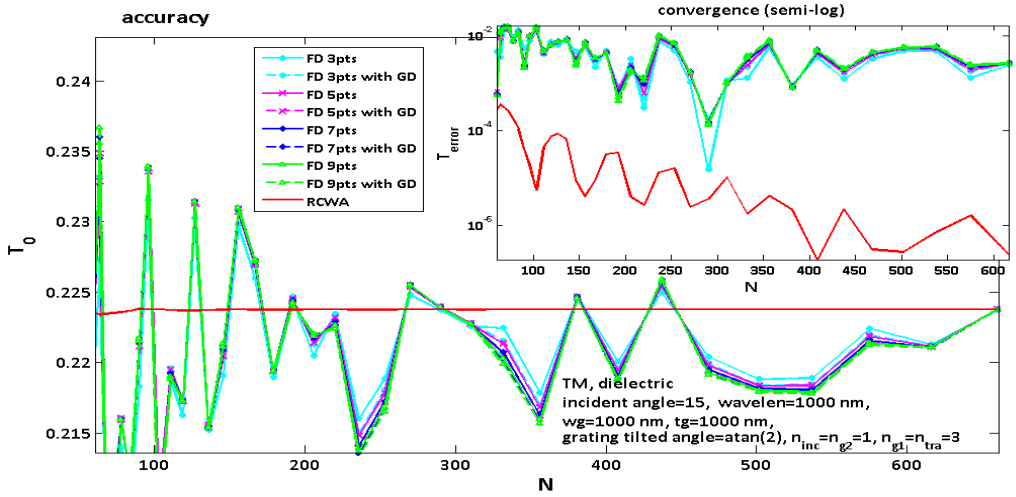

Figure 3.38: Convergence of the zeroth-order transmittance. A dielectric triangular grating with $\varepsilon_{g1} = 3^2$ under TM incidence.

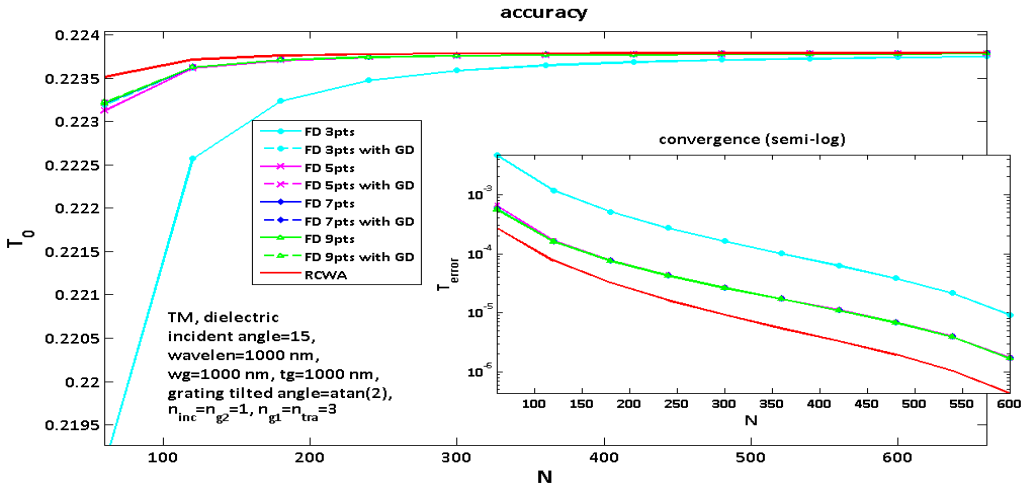

Figure 3.39: Convergence of the zeroth-order transmittance with proper discretization. A dielectric triangular grating with $\varepsilon_{g1} = 3^2$ under TM incidence.

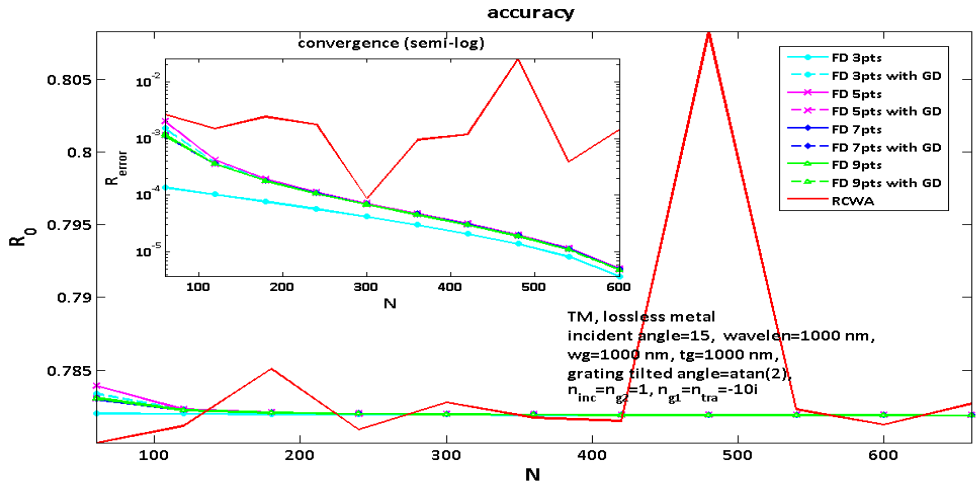

Figure 3.40: Convergence of the zeroth-order reflection with proper discretization. A lossless metal triangular grating with $\varepsilon_{g1} = (-10i)^2$ under TM incidence.

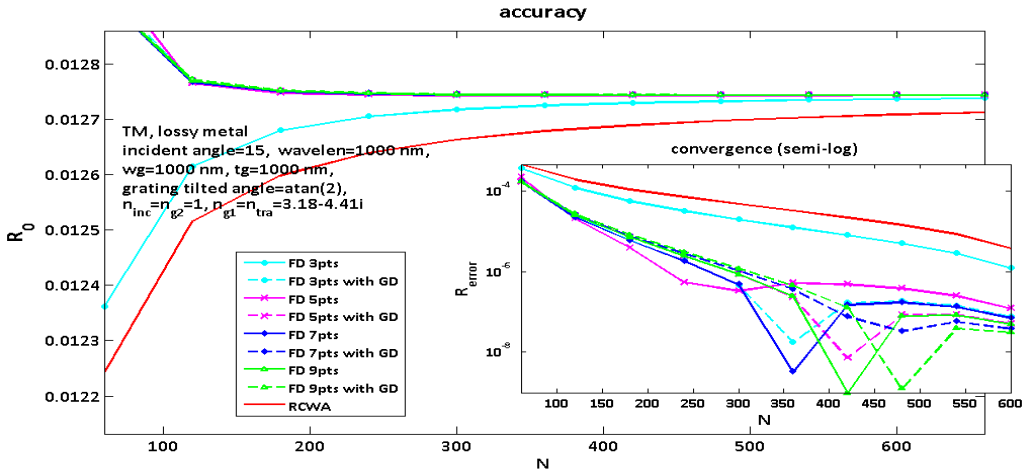

Figure 3.41: Convergence of the zeroth-order reflection with proper discretization. A lossy triangular grating with $\varepsilon_{g1} = (3.18 - 4.41i)^2$ under TM incidence.

3.5 Numerical Verification of 2DFD

Another method to solve the problem of RCWA for highly conductive and lossless metallic gratings under TM polarization is using two-dimensional finite difference (2DFD) to solve scattering problems directly. By comparing the duty cycle variation of graded-index 2DFD with RCWA and FDMM, it could be found that the graded-index approximation is appropriate for small index difference. Fig. 3.42 shows the duty cycle dependence of the minus-first order reflection, and the its parameters are: $\varepsilon_{r,inc} = \varepsilon_{r,g2} = 1$, $\varepsilon_{r,g1} = \varepsilon_{r,tra} = 3^2$, f from 0.98 to 0.08, $\Lambda = 500nm$, $\lambda = 632.8nm$, $t_g = 500nm$ and $\theta_{inc} = 30°$. There is a little deviation from the results of RCWA and FDMM because the index difference between 3 and 1 is not really small.

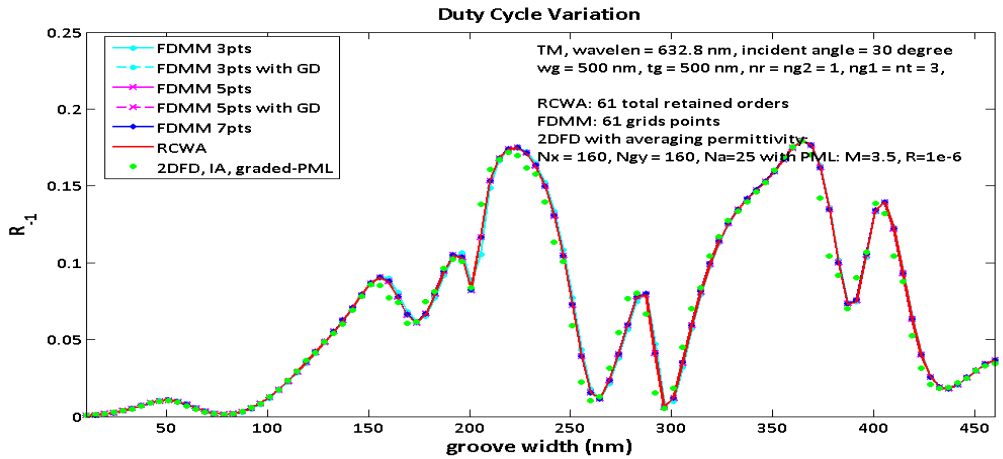

Figure 3.42: Duty cycle variation of the minus-first-order reflection. A dielectric grating with $\varepsilon_{g1} = 3^2$ under TM incidence. 2DFD with averaging permittivity is used.

However, for large index difference and nearly abrupt interfaces, the graded-index approximation has difficulty in accurately modeling the field behaviors. As in Fig. 3.43, which has the same parameters as in Fig. 3.12, it is found that the line of graded-index 2DFD deviates from the appropriated results but does not suffer large instability like RCWA.

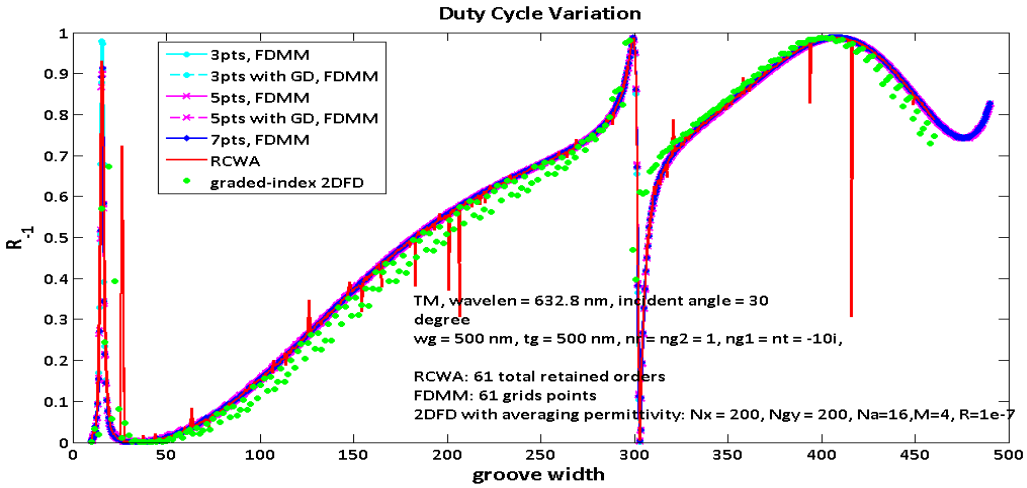

Figure 3.43: Duty cycle variation of the minus-first-order reflection. A lossless metallic grating with $\varepsilon_{g1} = (-10i)^2$ under TM incidence. 2DFD with averaging permittivity is used.

For the structure with abrupt interfaces or large index difference, it is better to consider the interface conditions in 2DFD, and this method is demonstrated in section 2.3. Using step-index 2DFD method to approach the same problem as Fig. 3.43, the results are shown in Fig. 3.44. It is found that the result of step-index 2DFD matches the results of FDMM well and does not suffer any instabilities.

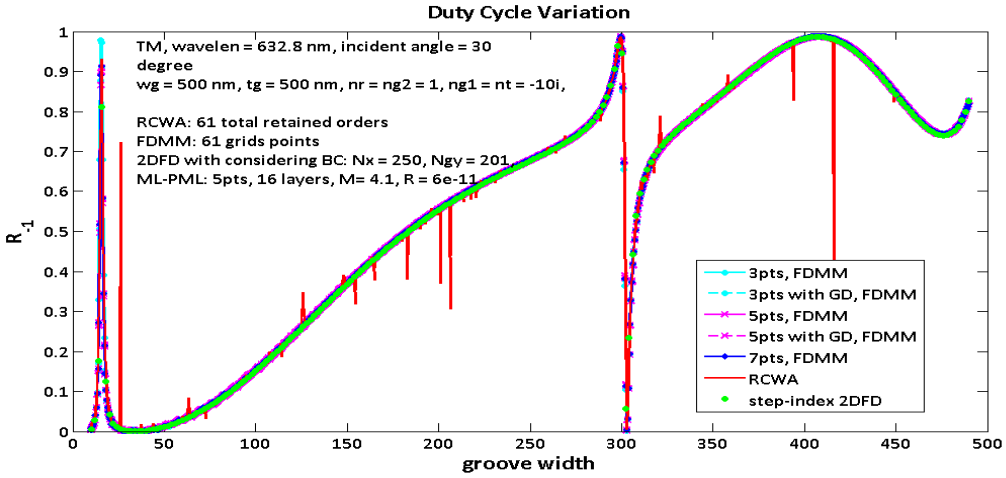

Figure 3.44: Duty cycle variation of the minus-first-order reflection. A lossless metallic grating with $\varepsilon_{g1} = (-10i)^2$ under TM incidence. 2DFD with considering boundary condition is used.

The fields diagrams obtained from four methods which have been presented in the thesis are shown in Fig. 3.45-Fig. 3.48. Fig. 3.45 and Fig. 3.46 have the same parameters as Fig. 3.44 with $302nm$ groove width. And Fig. 3.47 and Fig. 3.48 are the results for $250nm$ groove width. In Fig. 3.45 and Fig. 3.47, it is found that the fields calculated by RCWA do not vanish totally inside the lossless metallic gratings. This phenomenon may be explained by the spurious modes mentioned by Lyndin *et al.* [19] that the spurious mode resonance causes the field enhancement in the grating region.

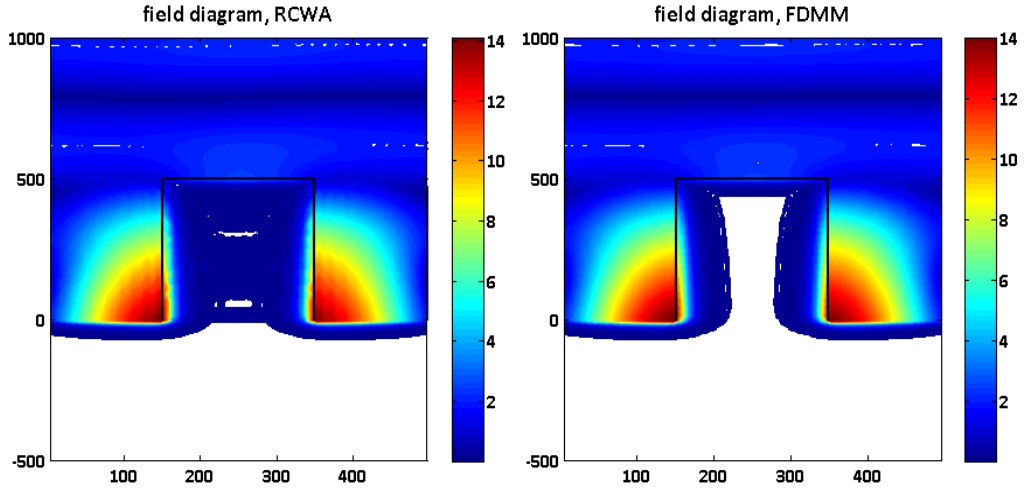

Figure 3.45: Field diagram of Fig. 3.12 at groove width= $302nm$ (Left: RCWA, Right: FDMM)

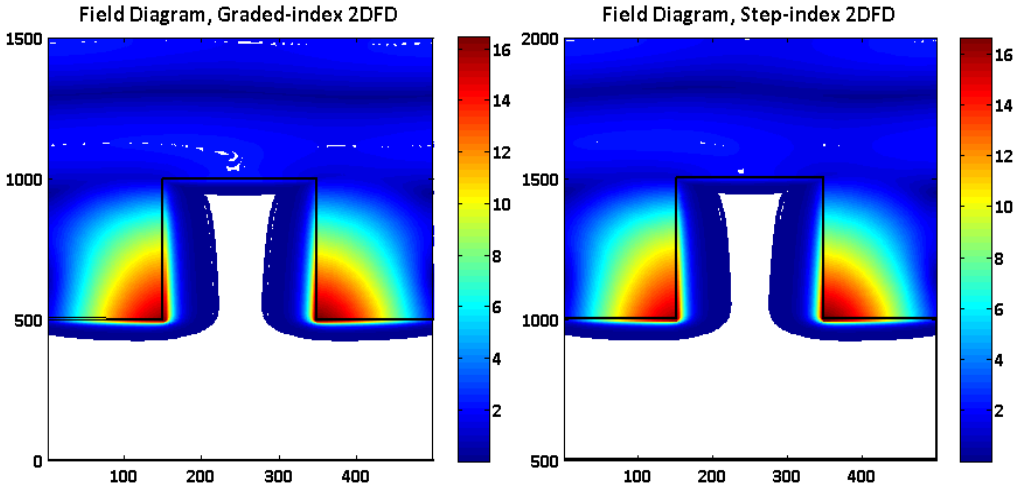

Figure 3.46: Field diagram of Fig. 3.12 at groove width= $302nm$ (Left: Graded-index 2DFD, Right: Step-index 2DFD)

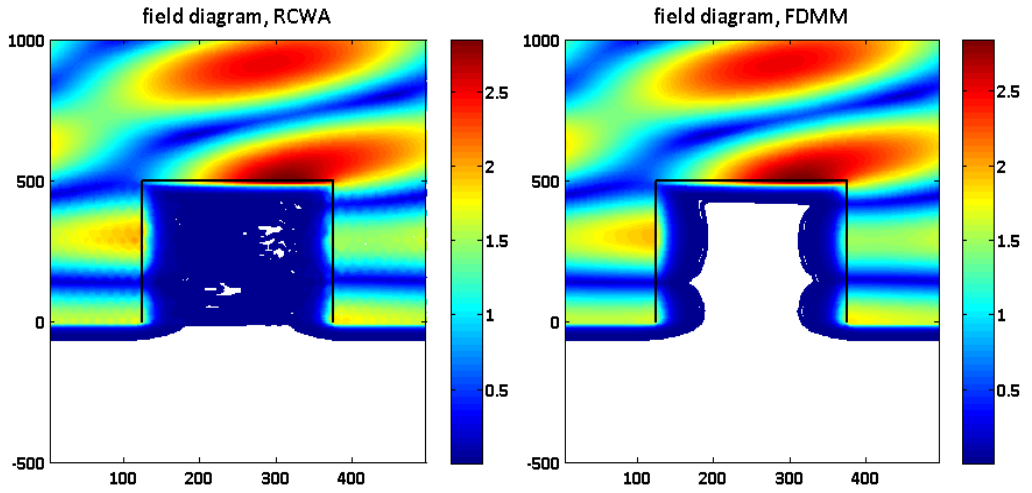

Figure 3.47: Field diagram of Fig. 3.12 at groove width= 250nm (Left: RCWA, Right: FDMM)

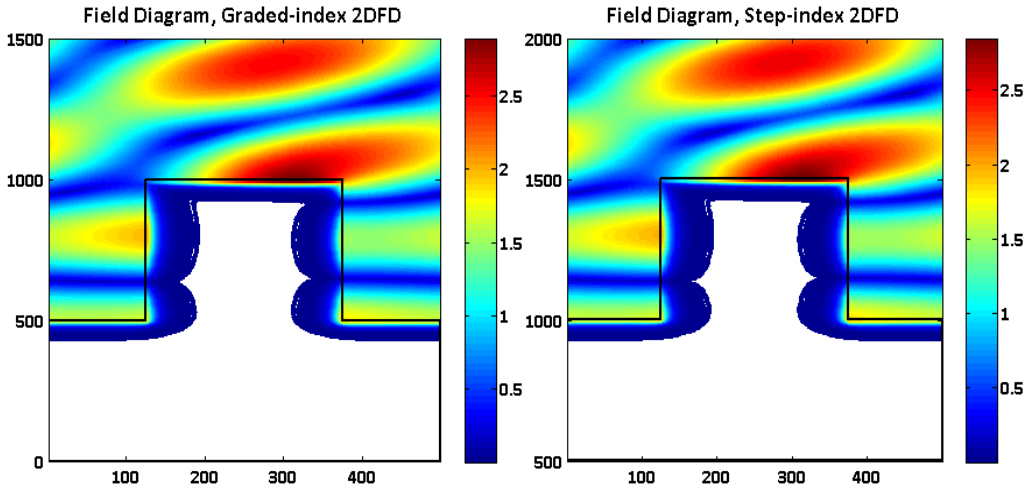

Figure 3.48: Field diagram of Fig. 3.12 at groove width= 250nm (Left: Graded-index 2DFD, Right: Step-index 2DFD)

Chapter 4

Conclusion

The arbitrary-order finite-difference modal method (FDMM) with step-index formulation for the analysis of gratings with one-dimensional periodicity has been presented. The correctness of FDMM is testified by comparing with some papers, and the accuracy and convergence of this method were compared with the Fourier modal method (FMM), also named rigorous coupled-wave analysis (RCWA). It is found that the accuracy of three-point FDMM with generalized Douglas scheme and even higher order methods are better than FMM for TE polarization in almost all cases. In addition, using nonuniform discretization with increased resolution near the discontinuities could accelerate the convergence. For TM polarization, the accuracy of FDMM could be superior to FMM for high conductive and lossless metallic gratings, and even for usual lossy metallic gratings as simulating gratings with arbitrary profiles by multi-layer approximation.

However, numerical results of rectangular-groove gratings indicates that

a proper discretization for FDMM is important under TM incidence. This problem may be attributed to the corners existing in calculated configuration and could be explained by disregard of some boundary conditions of the fields normal to the vertical interfaces as constructing the sparse matrix of each layer which causes contradiction of continuity of the fields tangential to horizontal interfaces as matching boundary conditions between every layers. Therefore, for arbitrary profile gratings under TM incidence, a proper discretization might be achieved by making the distances between discontinuities and their adjacent grid points on both sides of them equal, and the results will avoid instabilities and converge to the correct answer smoothly. Moreover, this technique could also be used for TE polarization to make results more stable.

Besides using FDMM to solve the serious problem of FMM as simulating lossless metallic gratings for TM polarization, the two-dimensional finite-difference methods of both graded-index and step-index formulation are presented and shown that the results are correct and stable, especially for step-index formulation.

Bibliography

[1] P. Vincent, "Differential method," in *Electromagnetic Theory of Gratings*, R. Petit ed., vol. 22 of Topics in Current Physics (Springer-Verlag, Berlin, 1980).

[2] M. G. Moharam and T. K. Gaylord, "Rigorous coupled-wave analysis of planar-grating diffraction," *J. Opt. Soc. Am.*, vol. 71, no. 7, pp. 811-818, July 1981.

[3] M. G. Moharam and T. K. Gaylord, "Rigorous coupled-wave analysis of grating diffraction−E-mode polarization and losses," *J. Opt. Soc. Am.*, vol. 73, no. 4, pp. 451-455, Apr. 1983.

[4] M. G. Moharam and T. K. Gaylord, "Three-dimensional vector coupled-wave analysis of planar-grating diffraction," *J. Opt. Soc. Am.*, vol. 73, no. 9, pp. 1105-1112, July 1983.

[5] M. G. Moharam, Eric B. Grann, and Drew A. Pommet, "Formulation for stable and efficientimplementation of the rigorous coupled-wave analysis

of binary gratings," *J. Opt. Soc. Am. A*, vol. 12, no. 5, pp. 1068-1076, May 1995

[6] M. G. Moharam and T. K. Gaylord, "Diffraction analysis of dielectric surface-relief gratings," *J. Opt. Soc. Am.*, vol. 72, no. 10, pp. 1385-1392, Oct. 1982.

[7] M. G. Moharam and T. K. Gaylord, "Rigorous coupled-wave analysis of metallic surface-relief gratings," *J. Opt. Soc. Am. A*, vol. 3, no. 11, pp. 1780-1787, Nov. 1986.

[8] R. Magnusson and T. K. Gaylord, "Analysis of multiwave diffraction of thick gratings," *J. Opt. Soc. Am.*, vol. 67, no. 9, pp. 1165-1170, Apr. 1977.

[9] R.S. Chu and J.A. Kong, "Modal theory of spatial periodic media," *IEEE Trans. Microwave Theory Tech.*, vol. MTT-25, no. 1, pp. 18-24, Jan. 1977.

[10] R. Magnusson and T. K. Gaylord, "Equivalence of multiwave coupled-wave theory and modal theory for periodic-media diffraction," *J. Opt. Soc. Am.*, vol. 68, no. 12, pp. 1777-1779, Apr. 1978.

[11] Lifeng Li, "Formulation and comparison of two recursive matrix algorithms for modeling layered diffraction gratings," *J. Opt. Soc. Am. A*, vol. 13, no. 5, pp. 1024-1035, May 1996.

[12] M. G. Moharam, Drew A. Pommet, Eric B. Grann and T. K. Gaylord, "Stable implementation of the rigorous coupled-wave analysis for surface-relief gratings: enhanced transmittance matrix approach," *J. Opt. Soc. Am. A*, vol. 12, no. 5, pp. 1077-1086, May 1995.

[13] Lifeng Li and Charles W Haggans, "Convergence of the coupled-wave method for metallic lamellar diffraction gratings," *J. Opt. Soc. Am. A*, vol. 10, no. 6, pp. 1184-1189, Jun. 1993.

[14] Philippe Lalanne and G. Michael Morris, "Highly improved convergence of the coupled-wave method for TM polarization," *J. Opt. Soc. Am. A*, vol. 13, no. 4, pp. 779-784, Apr. 1996.

[15] G. Granet and B. Guizal, "Efficient implementation of the coupled-wave method for metallic lamellar gratings in TM polarization," *J. Opt. Soc. Am. A*, vol. 13, no. 5, pp. 1019-1023, May 1996.

[16] Lifeng Li, "Use of Fourier series in the analysis of discontinuous periodic structures," *J. Opt. Soc. Am. A*, vol. 13, no. 9, pp. 1870-1876, Sep. 1996.

[17] Evgeny Popov, Boris Chernov, Michel Nevie're and Nicolas Bonod, "Differential theory: application to highly conducting gratings," *J. Opt. Soc. Am. A*, vol. 21, no. 2, pp. 199-206, Feb. 2004.

[18] Koki Watanabe, "Study of the differential theory of lamellar gratings made of highly conducting materials," *J. Opt. Soc. Am. A*, vol. 23, no. 1, pp. 69-72, Jan. 2006.

[19] Nikolay M. Lyndin, Olivier Parriaux, and Alexander V. Tishchenko, "Modal analysis and suppression of the Fourier modal method instabilities in highly conductive gratings," *J. Opt. Soc. Am. A*, vol. 24, no. 12, pp. 3781-3788, Dec. 2007.

[20] B. Guizal, H. Yala, and D. Felbacq, "Reformulation of the eigenvalue problem in the Fourier modal method with spatial adaptive resolution," *Opt. Lett.*, vol. 34, no. 18, pp. 2790-2792, Sep. 2009.

[21] Gérard Granet, "Reformulation of the lamellar grating problem through the concept of adaptive spatial resolution," *J. Opt. Soc. Am. A*, vol. 24, no. 12, pp. 2510-2516, Oct. 1999.

[22] Philippe Lalanne and Jean-Paul Hugonin, "Numerical performance of finite-difference modal methods for the electromagnetic analysis of one-dimensional lamellar gratings," *J. Opt. Soc. Am. A*, vol. 17, no. 6, pp. 1033-1042, June 2000.

[23] Yih-Peng Chiou, Yen-Chung Chiang, and Hung-Chun Chang, "Improved three-point formulas considering the interface conditions in the

finite-difference analysis of step-index optical devices," *J. Lightwave Texhnol.*, vol. 18, no. 2, pp. 243-251, Feb. 2000.

[24] Yih-Peng Chiou and Cheng-Han Du, "Arbitrary-order interface conditions for slab structures and their applications in waveguide analysis," *Opt. Express*, Mar. 2010.

[25] D. M. Pai and K. A. Awada, "Analysis of dielectric gratings of arbitrary profiles and thicknesses," *J. Opt. Soc. Am. A*, vol. 8, no. 5, pp. 755-762, Dec. 1990.

[26] Lifeng Li, "Multilayer modal method for diffraction gratings of arbitrary profile, depth, and permittivity," *J. Opt. Soc. Am. A*, vol. 10, no. 12, pp. 2581-2591, Dec. 1993.

[27] Yean-Woei Kiang and Chung-Han Hsieh, "Modified finite-difference frequency-domain method and its applications," *Master Thesis*, Jul. 2006.

[28] Jean-Pierre Bérenger, "A perfectly matched layer for the absorption of electromagnetic waves," *J. Comp. Phys.*, vol. 114, pp. 185-200, July 1994.

[29] Allen Taflove and Susan C. Hagness, *Computational Electrodunamics : the Finite-Difference Time-Domain Method*, 3^{rd} ed. Artech House, Boston, 2005.

[30] P. Sheng, R. S. Stepleman, and P. N. Sanda, "Exact eigenfunctions for square-wave gratings: application to diffraction and surface-plasmon calculations," *Phys. Rev. B*, vol. 26, no. 6, pp. 2907-2917, Sep. 1982.

[31] Yih-Peng Chiou, Yen-Chung Chiang, Chih-Hsien Lai, Cheng-Han Du, and Hung-Chun Chang, "Finite-difference modeling of dielectric waveguides with corners and slanted facets," *J. Lightwave Texhnol.*, vol. 27, no. 12, pp. 2077-2086, Feb. 2009.

[32] A. Wirgin, "A new theoretical approach to scattering from a periodic interface," *Opt. Commun.*, vol. 27, no. 2, pp. 189-194, Nov. 3, 1978.

[33] D. Maystre, "A new general integral theory for dielectric coated gratings," *J. Opt. Soc. Am.*, vol. 68, no. 4, pp. 490-495, Apr. 3, 1978.

[34] K. C. Chang, V. Shah and T. Tamir, "Scattering and guiding of waves by dielectric gratings with arbitrary profiles," *J. Opt. Soc. Am.*, vol. 77, no. 7, pp. 1385-1392, Jul. 1980.

[35] Maud Foresti, Ludivine Menez and Alexander V. Tishchenko, "Modal method in deep metal-dielectric gratings: the decisive role of hidden modes," *J. Opt. Soc. Am. A*, vol. 23, no. 10, pp. 2501-2509, Oct. 2006.